IOWA STATE UNIVERSITY
Digital Repository

2016

Improving performance and sustainability of unpaved roads: Stabilization and testing

Cheng Li
Iowa State University

Improving performance and sustainability of unpaved roads: Stabilization and testing

by

Cheng Li

A dissertation submitted to the graduate faculty

in partial fulfillment of the requirements for the degree of

DOCTOR OF PHILOSOPHY

Major: Civil Engineering (Geotechnical Engineering)

Program of Study Committee:
Jeramy C. Ashlock, Co-major Professor
David J. White, Co-major Professor
Pavana K.R. Vennapusa
Charles T. Jahren
Robert P. Ewing
Bora Cetin

Iowa State University
Ames, Iowa
2016

This work is dedicated to my newborn daughter,

Alina G. Li

TABLE OF CONTENTS

LIST OF TABLES

LIST OF FIGURES

ACKNOWLEDGEMENTS

I would like to express my deepest gratitude to my co-major professors, Drs. Jeramy Ashlock and David White, for their inspirations, guidance, and patience. Without their constant supports, this work would not have been possible.

I would like to thank my committee members Drs. Pavana Vennapusa, Robert Ewing, Charles Jahren, and Bora Cetin for providing constructive suggestions to my research and help in my personal life. I would also like to thank Dr. Christianna White for helping me to improve my technical writing and presentation skills.

The research projects were sponsored by the Iowa Department of Transportation (DOT). The Hamilton County secondary roads department is greatly appreciated for constructing test sections for this study. I would also like to acknowledge several graduate and undergraduate research assistants for performing lab and field tests.

Last but not the least; I want to express my deepest love to my parents, wife, and in-laws for their supports and encouragements throughout my study.

ABSTRACT

Unpaved roads in seasonal frost regions frequently experience severe damage during spring thaws, which adversely affects traffic safety and significantly increases maintenance costs. Current maintenance practices such as spreading new aggregate to cover the damaged roadway surface aim at repairing damage after it occurs, rather than minimizing or preventing its occurrence in the first place. Dust emission and aggregate loss are also severe issues for unpaved roads that are attributed primarily to the mechanical degradation of the surface aggregates. Due to the considerable variation in aggregate quality, most transportation agencies use the Los Angles (LA) abrasion test to set specifications for unpaved road surface materials. However, this testing method does not simulate the actual compaction or traffic loading conditions responsible for degradation of the materials in service. Furthermore, the LA abrasion test does not test the full material gradations and therefore cannot quantify the influence of the missing material on the actual field performance.

The goal of this study is to cost-effectively improve the performance and sustainability of unpaved roadway systems. To identify the most cost-effective stabilization methods for improving freeze-thaw performance of unpaved roads, several promising technologies were selected based on a comprehensive literature review, and used to construct a total of 17 test sections over a 3.22 km stretch of unpaved road in Hamilton County, Iowa. Design methods and construction procedures and costs were documented for each test section. Mechanistic-based field tests and visual inspections were conducted over two seasonal freeze-thaw periods (from 2013 to 2015) to compare the relative performance and durability of the various test sections. Based on the field testing and statistical analysis results, it was found that test sections stabilized

with macadam stone base layers yielded the best overall performance for both pre-freezing and post-thawing conditions.

In this research, a newly improved surface wave method (SWM) was also evaluated for determining the very shallow near-surface stiffness profiles of unpaved-road systems. By combining the SWM and falling weight deflectometer test, a new method of testing and analysis was developed to determine the in-situ nonlinear modulus reduction curves of each material layer in an unpaved road profile. The new method may provide significant improvements to current mechanistic-based design methods for both paved and unpaved roads.

To address the shortcomings of the commonly used LA abrasion test for evaluating degradation and abrasion of granular materials, a new laboratory testing method termed the Gyratory Abrasion and Image Analysis (GCIA) method was also developed in this study. The new testing method employs a gyratory compaction device and two-dimensional (2D) image analyses to determine changes in gradation, morphology, and mechanical properties of granular materials under simulated compaction or traffic loads. Based on the new GAIA test results, the density-strength-compaction energy relationships of granular materials can be rapidly established, and used to develop performance-based specifications that can improve the material's field performance, minimize its degradation, and save compaction time and energy.

CHAPTER 1. INTRODUCTION

Unpaved roads account for 63% of public roads in the state of Iowa, and 34% of the

6,702,195 total km of public roads in the United States (FHWA 2014). Compared to paved

roads, unpaved roads more frequently experience severe damage, which incurs significant

maintenance costs and adversely affects traffic safety (De Vries 2012; Jahren et al. 2005; White

and Vennapusa 2013). This chapter discusses the current industry and technical problems related

to unpaved roads, presents the research goal and objectives of this study, and details the

organization of the dissertation.

1.1. Problem Statement

Unpaved roads in seasonally frozen climate regions are frequently subjected to freeze-thaw

cycles, which could lead to severe damage including rutting, potholes, corrugations, and frost

boils. Most of the freeze-thaw related damage is caused by a combination of several factors,

including frost-susceptible subgrades, degraded surface materials, sources of water, poor

subsurface drainage, and heavy traffic loading (Henry and Holtz 2001; Hoover et al. 1981;

Kestler 2003; Saarenketo and Aho 2005; White and Vennapusa 2013). During spring thaws,

unpaved roads are usually heavily used by agricultural equipment, and the infiltrated water and

melted ice lenses in the surface and subgrade materials becomes trapped above the zone of

frozen subgrade, causing the saturated materials to lose strength and stiffness under heavy traffic

loads (Andersland and Ladanyi 2004).

Many counties in the northern U.S. impose traffic restrictions during the spring thawing

period to reduce such damage. Some approaches currently used by County Engineers to repair

the damaged areas include temporarily spreading rock on the affected areas, lowering or

improving drainage ditches, bridging the areas with stone and geosynthetics covered by a top

course of aggregate or gravel, coring boreholes and filling with calcium chloride to melt lenses and provide drainage, and re-grading the crown to a slope of 4 to 6% to maximize spring drainage (White and Vennapusa 2013). However, all these maintenance solutions aim to repair damage after it occurs, but not prevent or minimize the damage in the first place.

To prevent and mitigate freeze-thaw damage for unpaved road systems, various mechanical and chemical stabilization methods as well as recycled or by-product materials have been evaluated (Cetin et al. 2010; Henry et al. 2005; Hoover et al. 1981; Jiménez et al. 2012; Shoop et al. 2003). Generally speaking, it can be concluded that technologies which provide stable support conditions year-round with improved subsurface drainage can significantly improve the freeze-thaw performance of unpaved road systems. However, due to the different climate, traffic, and subgrade conditions of the separate studies, it is difficult to directly compare the relative effectiveness of the various technologies.

Dust emission and aggregate loss are also severe and costly issues suffered by unpaved roads, and are mainly attributed to mechanical degradation of the surface aggregates. Due to considerable variations in the quality of local aggregates, the additional new aggregates spread for maintenance can quickly break down to sand-size particles or airborne dust under traffic loads. The rapid deterioration of new aggregate adversely influences its mechanical, drainage, and freeze-thaw performance. Numerous previous studies have concluded that mechanical degradation of a granular material is a function of its mineral components, gradation, morphology, and loading conditions (Hardin 1985; Lade et al. 1996; Lees and Kennedy 1975; Marsal 1967; Nurmikolu 2005; White et al. 2004; Zeghal 2009). To quantify degradation characteristics and set specifications for granular materials, most researchers and transportation agencies rely on the Los Angeles (LA) abrasion and Micro-Deval tests, both of which require

that specimens be prepared to standard gradings and tested in a rotating steel drum containing steel spheres (ASTM 2014; ASTM 2014). However, these testing methods do not simulate the actual compaction or traffic loading conditions responsible for the degradation of the materials in situ, and do not test the full material gradations.

Unpaved roads under heavy traffic volume and loading are sometimes paved to improve ride quality and reduce maintenance costs. However, many agencies upgrade unpaved roads with little or no preparation of the foundation layers, and thus the new asphalt surface courses can rapidly deteriorate and also require significant recurring maintenance (Fay et al. 2016). Recent studies have emphasized the importance of using performance-based geotechnical field assessments for evaluating structural capacity, predicting damage susceptibility, or ensuring design and construction performance for pavement systems (Puppala 2008; Scott III et al. 2014; Vennapusa and White 2015; White et al. 2013). Geophysical testing methods, including the widely used multichannel analysis of surface waves (MASW) method, are potentially useful and powerful tools for such assessments. MASW is an efficient nondestructive testing (NDT) method commonly employed for profiling of elastic moduli of soil and pavement systems (Lin and Ashlock 2015; Park et al. 2001; Ryden 2004). However, MASW has not been applied to testing of unpaved roads with a focus on characterizing the elastic properties of both the unbound aggregate layer and top subgrade layer. Therefore, in this research, the MASW method was examined and compared to conventional in situ test methods to assess its ability to provide valuable inputs for condition assessment, mechanistic-based design, and QC/QA for construction of unpaved roads.

1.2. Research Goal and Objectives

The main goal of this research project is to cost-effectively improve the performance and sustainability of unpaved roadway systems in seasonal frost regions. To address this goal, the objectives of the research are to:

- Design and construct various field test sections using a range of technologies determined to be the most promising for improving freeze-thaw performance of unpaved roads, and compare their construction costs and as-constructed performances,

- Perform mechanistic-based field tests on the test sections over seasonal freeze-thaw cycles and statistically assess the field measurements to identify the most cost-effective methods,

- Develop a new laboratory testing method to evaluate mechanical degradation and changes in morphology and mechanical properties of granular materials under simulated field compaction and loading conditions, and

- Evaluate a newly-improved geophysical surface wave method for nondestructively determining the in situ multi-layered stiffness profiles of unpaved road systems.

1.3. Organization of the Dissertation

This dissertation consists of seven chapters: a general introduction, background, four research articles, and conclusions and recommendations for further research.

Following this general introduction, Chapter 2 provides background information for designs, specifications, stabilization methods, and two nondestructive testing methods for unpaved road systems. Chapter 3 details a demonstration project in which 17 test sections were constructed using several promising mechanical and chemical stabilization methods on a 3.2 km stretch of unpaved road in Hamilton County, Iowa. Extensive documentation, field and laboratory tests,

and field surveys were then analyzed to compare the construction costs, relative as-constructed performance, and stiffness changes of some mechanical stabilization sections one year after construction. Chapter 4 presents a statistical assessment of the post-thawing performance of the various test sections using mechanistic-based field testing data collected over two seasonal freeze-thaw cycles. Chapter 5 develops a new laboratory testing method to improve upon the shortcomings of current test methods, by employing the gyratory compaction device and 2D image analyses to determine changes in gradation, morphology, and shear strength of granular materials under simulated compaction or traffic loading. Chapter 6 evaluates the feasibility of using a newly improved multichannel analysis of surface wave (MASW) testing method to determine the near-surface multi-layered elastic modulus profiles of unpaved-road systems. This chapter also proposes a new method that combines data from MASW and falling weight deflectometer (FWD) tests to generate in-situ nonlinear modulus reduction curves for different material layers of unpaved road systems. Chapter 7 summarizes the conclusions and outcomes derived from this study, and offers several suggestions and directions for future research.

CHAPTER 2. BACKGROUND

This chapter consists of four sections: typical design methods for unpaved roads, state Department of Transportation (DOT) specifications for unpaved road surface materials, promising technologies for improving performance and durability of unpaved roads, and the nondestructive testing methods used in this study to determine multi-layered stiffness profiles of unpaved road systems.

2.1. Design Methods for Unpaved Roads

Various empirical and mechanistic-based methods have been proposed for thickness design of the surface aggregate layer of unpaved roads. The design basis, required inputs, and failure criteria of four typical design methods are summarized in Table 2.1 (AASHTO 1993; Bolander et al. 1995; Giroud and Han 2004a; Giroud and Han 2004b; Tannant and Regensburg 2001).

Table 2.1. Summary of design methods of unpaved roads.

Method	Basis	Inputs	Criteria
AASHTO Design Chart	Empirical	- ESAL[a] - Location of road M_R of subgrade [b] E of base material [c] - Aggregate loss	Rutting depth and serviceability
U. S. Forest Service Surface Thickness Program (STP)	Empirical	- ESAL CBR[d] of subgrade and aggregate	Rutting depth
Giroud and Han's Method	Mechanistic-Empirical	- Traffic load and volume CBR of subgrade and surface aggregate,	Rutting depth
Critical Strain Limit (CSL) method in Guidelines for Mine Haul Road Design	Mechanistic-Empirical	- Traffic volume M_R or E of each layer	Critical Strain

[a] Equivalent single axle load
[b] Resilient modulus
[c] Elastic modulus
[d] California Bearing Ratio

In the AASHTO design chart method, the U.S. map is divided into six climate regions. The
traffic load and volume are quantified using the equivalent single axial load (ESAL). The
seasonal variation of the subgrade resilient modulus (M_R) and aggregate loss are taken into
account. To provide drainage, a portion of the base layer can also be converted to an equivalent
thickness of subbase layer using an empirical chart.

For cases in which insufficient design inputs are available, AASHTO (1993) also provides a
design catalog (Table 2.2) for three traffic levels ranging from 10,000 to 100,000 ESALs. In the
catalog, the subgrade conditions are categorized into five levels, but the effective elastic modulus
of base material is consistently assumed to be 200 MPa.

**Table 2.2. Aggregate surfaced road design catalog: recommended aggregate base thickness
(in inches) for the six U.S. climatic regions, five relative qualities of roadbed soil and three
levels of traffic (AASHTO 1993).**

Relative Quality of Roadbed Soil	Traffic Level*	U.S. Climate Region					
		I	II	III	IV	V	VI
Very good	High	8	10	15	7	9	15
	Medium	6	8	11	5	7	11
	Low	4	4	6	4	4	6
Good	High	11	12	17	10	11	17
	Medium	8	9	12	7	9	12
	Low	4	5	7	4	5	7
Fair	High	13	14	17	12	13	17
	Medium	11	11	12	10	10	12
	Low	6	6	7	5	5	7
Poor	High	**	**	**	**	**	**
	Medium	**	**	**	15	15	**
	Low	9	10	9	8	8	9
Very poor	High	**	**	**	**	**	**
	Medium	**	**	**	**	**	**
	Low	11	11	10	8	8	9

* High (60,000 to 100,000 ESAL), Medium (30,000 to 60,000 ESAL), and Low (10,000 to 30,000 ESAL)
**Higher type pavement design recommended

The U. S. Forest Service Surface Thickness Program (STP) uses the empirical Equation (2.1)
to determine the thickness of surface aggregate layer, which was originally developed by the

U.S. Army Corps of Engineers based on the *CBR* values of the subgrade and surface aggregate materials (Barber et al. 1978):

$$RD = 5.8230 \frac{R^{0.2476}}{(\log t)^{2.002} C_1^{0.9335} C_2^{0.2848}} \qquad (2.1)$$

where *RD* is the rutting depth (in.), *R* is the ESAL adjusted by reliability (e.g., 50%), *t* is the thickness of top layer (in.), C_1 is the *CBR* of surface aggregate, and C_2 is *CBR* of subgrade.

The design method developed by Giroud and Han (2004a; 2004b) uses rutting depth as the failure criterion. Compared to other design methods that consider only the subgrade strength and traffic load and volume, this method also considers the distribution of vertical stress applied at the aggregate-subgrade interface, strength of the surface aggregate material, interlocking between geogrid and the aggregate material, and geosynthetic stiffness through Equation (2.2). The required thickness *h* must be determined iteratively, as it appears on both sides of the equation.

$$h = \frac{0.868 + (0.661)\left(\frac{r}{h}\right)^{1.5} \log N}{f_E} \times \left[\sqrt{\frac{P/(\pi r^2)}{m N_c f_C CBR_{SG}}} - 1 \right] r \qquad (2.2)$$

where *h* is the thickness of surface aggregate layer (m); *J* is the aperture stability modulus of geogrid (m-N/°); *r* is the radius of equivalent tire contact area (m^2); *N* is the number of axle passes; CBR_{SG} is the *CBR* of the subgrade (%); f_E is the modulus ratio factor, calculated based on *CBR* of the surface aggregate and subgrade; *P* is the axle load (kN); *m* is the bearing capacity mobilization coefficient; *Nc* is the bearing capacity factor; and f_C is the ratio of undrained cohesion and CBR_{SG}.

The CSL method uses the critical strain level as the failure criteria, for which the allowable strain limit (ASL) is determined using the empirical Equation (2.3), developed for heavy loading conditions on docks at container ports (Knapton 1989).

$$ASL = 80,000 / N^{0.27} \tag{2.3}$$

where *N* is the number of load repetitions.

The stress distribution and strain levels in each layer are calculated using a 2D finite element model.

2.2. Specifications for Unpaved Road Surface Materials

Gradation and plasticity have long been recognized as critical parameters for performance of unpaved road surface materials (e.g., Hudson et al. 1986; Jones and Paige-Green 2015; Paige-Green 1989; Skorseth and Selim 2000; Van Zyl et al. 2007). Skorseth and Selim (2000) explained that unpaved road surface materials are different from granular base materials, because the base materials usually have a larger top size and contain a very small percentage of fines. These two characteristics can provide better drainage but result in a surface that is unstable and difficult to maintain when used on unpaved roads. Légère and Mercier (2003) developed a chart for comparison of typical base material specifications with unpaved road wearing course specifications, and the gradation-related surface distress (Figure 2.1).
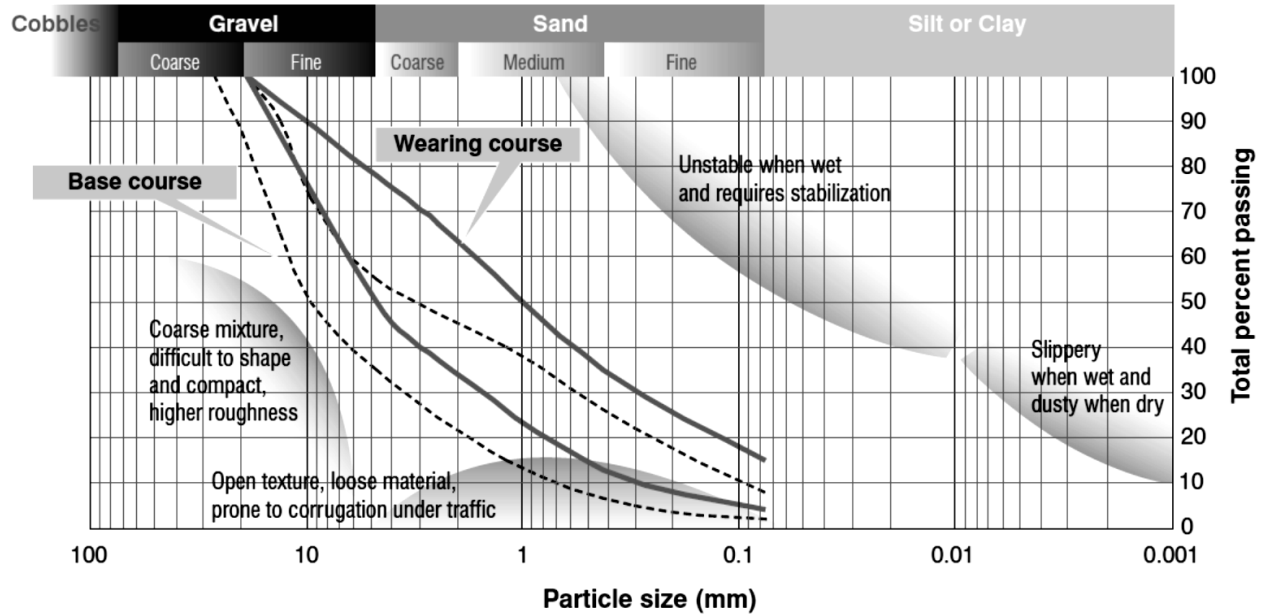
Figure 2.1. Typical specifications for the range of particle-size gradations for a base course and a wearing course, and size distributions that typically pose surface-distress problems (Légère and Mercier 2003).

Specifications for gradation and plasticity index of unpaved road surface materials vary between different state DOTs. Table 2.3 summarizes some typical specifications used by Iowa and several neighboring states. All of the specifications were established based on arbitrary gradation bands with at most six control points. In addition, most of the specifications do not include plasticity index, except for those from South Dakota and Illinois. The importance of gradation and plasticity have long been emphasized in several design and maintenance manuals of unpaved roads (e.g., Jones et al. 2013; Jones and Paige-Green 2015; Paige-Green 1998; Skorseth and Selim 2000). However, most of the current specifications are not performance-related, and quantitative evaluations are lacking.

Table 2.3. Some typical specifications for gradation and plasticity of unpaved road surface material used by Iowa DOT and some adjacent state DOTs.

Sieve No.	Iowa Class A or B	South Dakota	Illinois CA-6	Minnesota Class 1	Nebraska Rock	Missouri Grade B
1.5			100			
1	100		100-90		100	100
3/4 in.	100-95	100		100		
1/2 in.	90-70		90-60			
3/8 in.				95-65		< 65
No. 4	55-30	78-50	56-30	85-40	60-20	
No. 8	40-15	67-37				
No. 10				70-25	30-0	25-5
No. 16			40-10			
No. 40		35-13		45-10		
No. 200	16-6	15-4	12-4	15-8	10-0	
Plasticity Index	NA	12-4	9-2	NA	NA	NA

Paige-Green (1989) developed a performance-related material selection chart for unpaved road surfaces based on testing and monitoring of 110 unpaved road sections for more than three years in Southern Africa (Figure 2.2). The grading coefficient and shrinkage product in the figure are calculated using below equations.

$$\text{Grading Coefficient} = \frac{(\% \text{ passing } 26.5\,\text{mm} - \% \text{ passing } 2.0\,\text{mm}) \times \% \text{ passing } 4.75\,\text{mm}}{100} \quad (2.4)$$

$$\text{Shrinkage Product} = \text{Bar Linear Shrinkage} \times \% \text{ passing } 0.425\,\text{mm} \quad (2.5)$$

The bar linear shrinkage of a material is determined using the bar linear shrinkage test described in the South African Technical Methods for Highways (TMH1-A4). However, to use this chart, calibrations for local subgrade conditions and mechanical properties of surface aggregate materials are required.
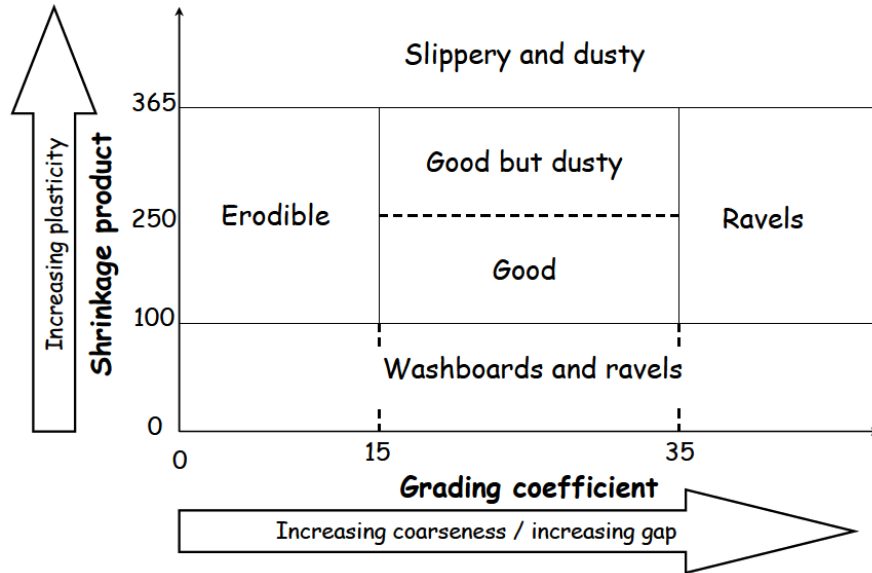
Figure 2.2. Relationship between shrinkage product, grading coefficient, and performance of surface course of gravel roads (from South Africa DOT, 1990).

In addition to the gradation and plasticity, most state DOTs use the Los Angeles (LA) abrasion test to set specifications for quality of unpaved road surface materials. According to the LA Abrasion ASTM Standard (2014), depending on the original gradation of the material, the specimen must be washed and prepared to a standard grading before being tested in a rotating steel drum containing steel spheres. After the test, the specimen is washed and sieved through a 1.7 mm sieve, and the percent passing is reported as the LA abrasion loss or percent loss of the material. Because the specimen is first prepared to a standard grading, the influence of the material's original gradation on the actual abrasion performance in the field is eliminated.

2.3. Technologies for Improving Performance and Durability of Unpaved Roads

Many previous studies have evaluated various methods such as mechanical and chemical stabilization and the use of geosynthetics to improve the freeze-thaw performance of unpaved roads (e.g., Azadegan et al. 2013; Berthelot and Carpentier 2003; Henry et al. 2005; Hoover et al. 1981). Based on the results of the previous studies, it can be concluded that methods that

permanently increase strength and stiffness, or improve subsurface drainage can effectively

minimize freeze-thaw damage of unpaved road systems. To assess the various stabilization

methods for improving freeze-thaw performance of low-volume roads, White and Vennapusa

(2013) reviewed more than 150 domestic and international literature and identified a range of

most promising methods that are summarized below:

2.3.1. Macadam stone base layers

Macadam stone base layers containing large aggregate size (i.e., maximum size of 75 or

100 mm) without tar or bitumen binder were believed to facilitate drainage and stability for both

unpaved and paved roads due to the large voids and significant particle interlocking between

aggregates. Several field projects conducted in Iowa concluded that construction of roads with

macadam base layers was easy and fast (e.g., Hoover et al. 1981; Jobgen et al. 1994; Less and

Paulson 1977; Lynam and Jones 1979). Macadam stone materials were placed on top of prepared

subgrades or existing road surfaces using a Jersey Spreader and compacted using a vibratory

drum roller. A choke stone layer with double seal asphalt coat (Jobgen et al. 1994; Less and

Paulson 1977) or Portland cement concrete (PCC) and asphalt concrete (AC) (Lynam and Jones

1979) was built upon as surface course in these projects. The procedures and equipment used for

constructing the macadam base layer were as specified in Section 2210.03 of the Iowa DOT

specification (Iowa DOT 2012). Performance of the test sections was evaluated by annual field

tests and visual inspections, and compared with that of sections stabilized by other chemical

methods. The test results showed that freeze-thaw damage of the road sections can be effectively

minimized by the macadam base layers (Less and Paulson 1977; Lynam and Jones 1979).

Compared to other stabilization methods, the macadam base sections also showed the best

overall performance and durability (Jobgen et al. 1994). Less and Paulson (1977) also evaluated

the effects of the thickness of the macadam base layer on the performance of the unpaved roads, and recommended 200 mm as the most cost-effective design thickness in Iowa.

2.3.2. Chemical stabilization methods

They summarized that chemical stabilizers used are typically either active or passive. Active chemical admixtures that are commonly used include Portland cement, fly ash, lime, and bentonite, and passive chemical admixtures include bitumen, plant processed bio-fuel co-products with varying lignin contents and lignosulfates, and polymer emulsions. In this study, Portland cement, ASTM Class C self-cementing fly ash (ASTM, 2012), and bentonite were used and information pertaining to these admixtures is provided herein.

Use of cement and ASTM class C (self-cementing) fly ash can improve the shear strength, stiffness, and wet-dry and freeze-thaw durability of soils (e.g., Cetin et al. 2010; Johnson 2012; Parsons and Milburn 2003; Shoop et al. 2003; Solanki et al. 2013; White et al. 2005; Zhang et al. 2016). Chu et al. (1955) and Terrel et al. (1979) have provided guidance on the type of chemical stabilizer to use depending on the soil classification and plasticity properties.

Using self-cementing fly ash for soil stabilization provide environmental incentives in terms of using a waste product and cost savings relative to other chemical stabilizers, but the characteristics of fly ash change significantly between plants and therefore warrants a detailed laboratory mix design and evaluation (White et al. 2005; White et al. 2005).

Freeze-thaw durability of chemically stabilized materials has been studied by many researchers in laboratory setting by determination of loss of material during freeze thaw cycles and/or unconfined compressive strength/California bearing ratio (CBR) after a certain number of freeze thaw cycles. Portland cement stabilized materials generally show superior performance than any other chemical stabilizer (Henry et al. 2005; Parsons and Milburn 2003), while mixed

information was documented with fly ash stabilized soils. For e.g., Berg (1998) studied freeze-thaw performances of reclaimed hydrated fly ash activated aggregate materials, and found that the materials did not survive over ten laboratory freeze-thaw cycles. However, some field studies documented therein showed that these materials did perform well, even though they break down during the freeze-thaw action. Results presented by Bin-Shafique et al. (2010) were similar to Berg (1998), in terms of performance of fly ash stabilized soils. Bin-Shafique et al. (2010) indicated that fly ash stabilized soils lost up to 40% of the strength due to freeze-thaw cycles, although they did not experience significant strength loss during wet-dry cycles. Khoury and Zaman (2007) investigated the effect of freeze-thaw cycles on cement kiln dust (CKD), class C fly ash, and fluidized bed ash (FBA) stabilized aggregates. Results indicated that the resilient modulus values of these mixtures decreased with increasing freeze thaw cycles. Comparisons with no stabilizer were not provided in this study. It is mentioned therein that CKD stabilized base materials deteriorated faster than fly ash and FBA stabilized base materials.

Bergeson and Wahbeh (1990) and Bergeson et al. (1995) documented the use of bentonite to surface treat the gravel roads as a means for dust reduction in comparison with calcium and magnesium chloride. They noted that the negatively charged surfaces of bentonite particles (sodium montmorillonite clay) can interact with the positively charged limestone fines particles, and the "electrochemical glue" can effectively reduce dust and improve slaking characteristics and stability of limestone-surfaced roads. Bergeson et al. (1995) concluded that calcium chloride treatments are 2 to 3 times more effective in the short term, but bentonite is more cost-effective, because the bonding capability of bentonite can last much longer (2–3 winter seasons) than chloride treatments (3–4 months).

2.3.3. Geosynthetics

Geosynthetics are typically placed between subgrade and surface courses to serve as subsurface drainage layers, provide reinforcement, create capillary barriers, and provide separation. Stabilization using geotextiles and geogrids has been extensively studied for mitigating freeze-thaw damage of unpaved roads (Henry 1990; Henry 1996; Hoover et al. 1981; Lai et al. 2012). The mechanisms, design, and benefits of using geogrids and geotextiles to stabilize unpaved roads were examined in Giroud and Han (2004a; 2004b). Henry (1990) conducted a laboratory study using geotextiles to mitigate frost heave, and the results showed that geotextiles used as capillary breaks reduced frost heave of soil specimens by about 60%. In a later study, Henry (1996) also found that geotextiles can reduce rates of frost heave, but the performance can be influenced by the pore size distribution, wettability, and thickness of the geotextiles, and those having higher capillary rise when inserted in water may exacerbate frost heave. Hoover et al. (1981) evaluated effects of a nonwoven geotextile on frost heave and thaw weakening of unpaved roads built on frost-susceptible silty soils in Iowa. Laboratory Iowa K tests combined with freeze-thaw tests showed that specimens with embedded geotextile discs resulted in lower frost-heave rates and higher cohesion and friction angles than control specimens after freezing-thawing cycles, but the stiffnesses of specimens with geotextile discs were decreased. However, field tests showed that the geotextile had no influence for roads with a stiffer base (i.e., granular backfill or macadam stone base), but could improve freeze-thaw durability for roads having lower composite stiffnesses. Henry et al. (2005) also conducted a demonstration project to compare several geosynthetic types including geogrid, geotextile, geowrap, geocell, and a patented geosynthetic capillary barrier for improving freeze-thaw performance of unpaved roads in Vermont. Field tests and monitoring results over two years

showed that the geogrid and geotextile placed between subgrade and surface course layers did not provide an observable benefit.

Geocomposite materials usually consist of three layers: two layers of geotextile acting as filters sandwiching a drainage net or geogrid acting as conduit for water (Holtz et al. 2008). Geocomposite materials are therefore typically designed as drainage layers and capillary barriers to improve hydraulic conductivity and freeze-thaw performance of road systems. Several previous studies have assessed the use of geocomposite drainage layers for both paved and unpaved roads using laboratory, field, and numerical evaluations (e.g., Bahador et al. 2013; Christopher et al. 2000; Henry and Holtz 2001; Henry et al. 2005; Stormont et al. 2001).Christopher et al.(2000) installed a geocomposite drainage layer at three different vertical locations within a pavement system: 1) under the asphaltic concrete pavement, 2) under the base coarse aggregate, and 3) on or within the subgrade to allow for a capillary break to reduce frost action. The authors found that a geocomposite drainage layer placed on or within the subgrade can remove water from the road system during spring thaw quicker than other locations. Henry and Holtz (2001) conducted a laboratory investigation using both geotextile and geocomposite drainage layers to mitigate frost heave of soil specimens. The laboratory frost heave test results showed that geotextiles that were moistened and which contained soil fines to simulate field conditions did not reduce frost heave. The specimens with geocomposite barriers prepared in the same manner showed significant reductions in frost heave when the degree of saturation of the overlying soil was below 75%. When the degree of saturation of the overlying soil exceeded 80%, however, the geocomposites permitted significant heave due to water migrating from one geotextile to the other through thin films adhered to the middle geonet layer. Henry et al. (2005) also conducted a field investigation to compare different technologies for mitigation freeze-thaw

damage to unpaved roads. Field dynamic cone penetrometer (DCP) tests and rutting measurements showed that a patented Geosynthetic Capillary Barrier Drain provided benefits by keeping the upper layers of the soil relatively dry. However, geogrid and geotextile separators placed 300 mm deep provided no observable benefit. Bahador et al. (2013) numerically evaluated effects of geocomposite drainage layers on the moisture distribution and plastic deformations of both paved and unpaved roads. The authors found that the geocomposite layer can decrease plastic deformation of the road systems through combined mechanistic and hydraulic actions, but increasing the thickness of surface course layer will reduce the reinforcement effect of the geotextile on both sides of the geocomposite material.

2.4.   The FWD and MASW Test

Performance-based nondestructive testing methods including the falling weight deflectometer (FWD) and multichannel analysis of surface wave (MASW) tests are used to determine multi-layered elastic stiffness profiles of pavement systems. The FWD and MASW methods employ two different theories (i.e., the theory of elastic layer systems and wave propagation theory, respectively) and optimization methods to back-calculate the elastic moduli of the multi-layered pavement systems. The FWD test usually involves applying large dynamic impact loads on road surface to simulate traffic loading, and measuring system response (deflection) through one or multiple sensors, then calculating composite or multi-layered elastic moduli of pavement systems (Lytton 1989; Wightman et al. 2004). Compared to the FWD test, the MASW tests applies a much smaller impact on the ground surface to generate seismic surface waves, and the resulting surface motion is measured using an array of geophones or accelerometers (Lin 2014; Lin and Ashlock 2015; Park et al. 1998; Park et al. 1999; Xia et al. 1999). Employing the phenomenon of dispersion of surface waves in layered elastic media, the layer properties (e.g., thickness and

modulus) can be inferred by matching experimental dispersion curves to their theoretical counterparts.

Unpaved road systems typically consist of two layers: subgrade and surface aggregate. An equivalent layer method is commonly used for back-calculating elastic moduli of two layered systems using FWD data (AASHTO 1993). This approach combines Boussinesq theory and Odemark's equivalent layer thickness assumption (Boussinesq 1885; Odemark 1949). The subgrade modulus (E_{SG}) is calculated as

$$E_{SG} = \frac{(1 - \nu^2) F_{\max}}{\pi \, r \, d_{(r,0)}} \tag{2.6}$$

where ν is Poisson's ratio, F_{max} is applied peak load (kN), r is distance from the center of the loading plate to the measurement location (mm), and $d_{(r,0)}$ is road surface deflection measured at distance r (mm).

To eliminate the influence of surface aggregate on the subgrade modulus, the road surface deflection should be measured at a distance greater than 0.7 times a_e, which is the effective radius of the stress bulb at the interface of the two layers;

$$a_e = \sqrt{A^2 + \left(h \sqrt[3]{\frac{E_{AGG}}{E_{SG}}} \right)^2} \tag{2.7}$$

where A is the radius of the loading plate in mm, and h is the thickness of the surface aggregate layer in mm. The measured deflection can then be considered to be caused only by subgrade deformation and independent of the size of the loading plate.

To back-calculate the elastic modulus of the surface aggregate layer (E_{AGG}), Odemark's assumption is used to determine the deflection of a two layer system under an applied load by

converting the thickness of the surface aggregate layer (h) into an equivalent thickness (h_e) of additional subgrade given by

$$h_e = h\left(\frac{E_{AGG}}{E_{SG}}\right)^{1/3}$$

(2.8)

The total surface deflection directly beneath the FWD loading plate caused by the deformation of both the surface aggregate layer and subgrade can then be calculated as

$$d_{0,0} = \frac{\left(1-v^2\right)F_{max}f}{\pi A}\left\{\frac{1}{E_{SG}\sqrt{1+\left(\frac{h}{A}\sqrt[3]{\frac{E_{AGG}}{E_{SG}}}\right)^2}} + \frac{\left[1-\frac{1}{\sqrt{1+\left(\frac{h}{A}\right)^2}}\right]}{E_{AGG}}\right\}$$

(2.9)

By matching the calculated deflection ($d_{(0,0)}$) to the measured deflection underneath the loading plate, the elastic modulus of the surface aggregate layer (E_{AGG}) is then iteratively determined.

In contrast to conventional seismic reflection and refraction methods, the MASW test is capable of measuring modulus profiles of stiff over soft layers (Lin and Ashlock 2011). When applying traditional surface wave analysis methods to pavement systems, several challenges are encountered such as numerical instability when using the transfer matrix method to calculate theoretical dispersion curves at high frequencies, and convergence to a local minimum when using the Levenberg-Marquardt method for inversion (Lin and Ashlock 2011).

To address these issues, several improvements were made to the dispersion analysis and inversion procedures for MASW data analysis by Lin (2014). The improvements include a new phase-velocity and intercept-time scanning (PIS) method to improve the resolution and sharpness

of experimental dispersion images by minimizing side lobes and aliasing that can be generated by conventional wavefield transformation methods. The side lobes and aliasing can lead to misidentification of apparent higher and lower modes, resulting in errors in the inverted profiles. In addition, the new PIS dispersion analysis method does not require a complex high-accuracy trigger system, because it eliminates the assumption of the conventional methods that the impact point coincides with the generation point of the Rayleigh waves. The PIS method first converts the field data from the space-time domain to the space-frequency domain by applying a Fourier transform, then uses the slant-stack scheme to provide a new series of harmonic curves in the phase slowness-time intercept plane, and lastly applies another Fourier transform followed by auto-power spectrum analysis to the new harmonic curves to generate the experimental dispersion image. A new hybrid genetic-simulated annealing (GSA) optimization algorithm developed by Lin (2014) can improve the inversion procedure by enhancing global searching efficiency, thus reducing the risk of becoming trapped in a local minimum. The GSA method uses a new combination of the genetic algorithm (GA) and simulated annealing (SA) algorithm, which excel at global and local searches, respectively.

CHAPTER 3. MECHANISTIC-BASED COMPARISONS OF STABILIZED BASE AND GRANULAR SURFACE LAYERS OF LOW-VOLUME ROADS

A paper submitted to *International Journal of Pavement Engineering*

Cheng Li, Jeramy C. Ashlock, David J. White, and Pavana K.R. Vennapusa

3.1.   Abstract

Granular surface and base layers of low-volume roads (LVRs) are frequently subjected to severe damage caused by heavy agricultural traffic loads and weather changes, which adversely affects safety and requires regular repair and maintenance. Various stabilization methods have been evaluated for mitigating damage and improving serviceability of LVR systems. However, few well-documented comparisons exist of the field mechanical performance, durability, and construction costs of different stabilization methods under the same set of geological, climate, and traffic conditions. Therefore, the present study was conducted to identify the most effective and economical among several stabilization methods for repairing or reconstructing granular surface and base layers of LVRs. In this study, a range of promising technologies from a comprehensive literature review were selected and examined using field demonstration sections. A total of nine geomaterials, three chemical stabilizers, and three types of geosynthetics were used to construct various test sections over a 3.22 km stretch of granular-surfaced road. Extensive falling weight deflectometer (FWD) and dynamic cone penetrometer (DCP) tests were performed to evaluate the multi-layered elastic moduli and strengths of the various sections. This paper details the design and construction of each test section, compares the as-constructed mechanistic performance of all test sections, and assesses stiffness changes of several sections one year after construction. To provide a statistical basis for the comparisons, a pairwise multiple-comparison procedure applied for unequal sample sizes and variances and the paired *t*-

test were used to analyse the FWD test results, demonstrating that the performance measures of the various sections were significantly different.

3.2. Introduction

Granular surface and base layers of low-volume roads (LVRs) frequently experience severe damage that adversely affects traffic safety and requires regular repair and maintenance. Additionally, many agencies upgrade damaged granular-surfaced roads with little or no preparation of the foundation layers, and thus the new asphalt surface courses can rapidly deteriorate and also require recurring maintenance (Fay et al. 2016). Various mechanical and chemical stabilization methods as well as recycled and by-product materials have been evaluated for mitigating damage and improving serviceability of LVR systems (e.g., Henry et al. 2005; Hoover et al. 1981; Jiménez et al. 2012; Shoop et al. 2003). However, few detailed and well-documented comparisons of the relative field performance, durability, and construction costs of various stabilization methods under the same set of geological, climate, and traffic conditions are available.

In this study, a comprehensive literature review was conducted to assess cost-effective technologies for mitigating damage and improving serviceability of LVRs. Based on the literature review, a total of 17 field test sections were designed and constructed over a 3.22 km stretch of heavily used granular-surfaced road using nine different geomaterials, three chemical stabilizers, and four types of geosynthetics. Construction procedures and costs including materials, labour, and equipment were documented for each test section. Extensive series of falling weight deflectometer (FWD) and dynamic cone penetrometer (DCP) tests were conducted to compare the as-constructed mechanistic performance of all sections, as well as the stiffness change of several sections one year after construction. A pairwise multiple-comparison

procedure applied for unequal sample sizes and variances and the paired *t*-test were used to analyse the FWD test results to provide a statistical basis for the comparisons.

3.3. Background

White and Vennapusa (2013) reviewed more than 150 research publications to assess technologies and geomaterials for mitigating damage and improving serviceability of LVRs in seasonally cold regions. All of the reviewed publications were summarized in White and Vennapusa (2013) using a matrix of the form shown in Table 3.1, and organized into a searchable electronic database to provide researchers and practitioners information on experiences regarding the various stabilization methods and measurement technologies. Based on the extensive literature review, it was concluded that technologies which permanently increase strength and stiffness or improve subsurface drainage can significantly improve the performance and durability of LVR systems. The following subsections provide background information for some of the stabilization methods used for test sections in this study.

Table 3.1. Literature assessment matrix used in White and Vennapusa (2013), showing example assessment for one publication.

KEY: ✓ = item addressed C – Chemical stabilization (cement, fly ash, bitumen/asphalt emulsion, hydrated fly ash, lime, chlorides, bentonite, combinations, biofuel byproducts) M – Mechanical stabilization (blending, geosynthetics, macadam base, fibers, use of recycled products) B – Bio-stabilization G – Granular Soil NG – Non-Granular Soil O – Other (e.g., hydrated fly ash) D – Domestic I – International AP – Agency Publication B – Book CP – Conference Proceedings IP – Industry Publication NJ – Non Peer-Reviewed Journal P – Patent PJ – Peer-Reviewed Journal T – Thesis (Masters) D – Dissertation (Doctorate) TR – Technical Report	Stabilization Type	Soil Type	Freeze/Thaw or Frost Boil Issues	Rehabilitation/Repair Options	Stabilization Design Procedure/Typical Values	Durability (Freeze/Thaw Cycles)	Construction Methods/Considerations and Time	Equipment and Contractors	Specifications	QA/QC Testing Procedures	Performance Monitoring Results	Limitations	Lab Testing Results	Field Study – Granular-surfaced road	Field Study – Paved Road	Environmental Impacts	Initial Cost	Life Cycle Costs	Maintenance Issues	Numerical Analysis / Thickness Design Aspects	Origin of Reference	Publication Type	Number of Instances Cited[a]
Khoury and Zaman (2007)	C	G				✓							✓									PJ	10

3.3.1. Macadam stone base layers

Macadam stone base (MSB) layers containing large particle sizes (i.e., a maximum of 100 mm) without tar or bitumen binder have been used successfully for both paved and unpaved roads in Iowa, USA (Hoover et al. 1981; Jobgen et al. 1994; Less and Paulson 1977; Lynam and Jones 1979). Annual visual inspections and field tests revealed that the MSB layers not only improved stability, but also minimized water-related damage due to large void ratios and significant particle interlocking between the large aggregates (Less and Paulson 1977; Lynam and Jones 1979). Compared to biochemical- and asphalt-treated base materials, test sections with MSB layers also provided the best overall performance and durability (Jobgen et al. 1994). Less and Paulson (1977) evaluated the effects of MSB layer thickness and concluded that a 200 mm thick MSB was the most cost-effective design for Iowa. In addition, the authors reported that

marginal macadam stone materials having a high abrasion loss of approximately 50% performed satisfactorily.

3.3.2. Stabilization by cement, self-cementing fly ash, and bentonite

Portland cement and self-cementing fly ash have long been recognized as cost-effective active chemical stabilizers for improving the strength, stiffness, and freeze-thaw and wet-dry durability of a wide range of soils (e.g., Cetin et al. 2010; Ghafoori et al. 2013; Johnson 2012; Parsons and Milburn 2003; White et al. 2005). Several guidelines for cement and fly ash stabilization were also developed to control chemical reactions, provide empirical charts to determine the optimum type and percentage of stabilizers, and recommend construction procedures as well as quality control and quality assurance methods (Bergeson and Barnes 1998; PCA 1995; White et al. 2005; Winterkorn and Pamukcu 1991). However, several factors affecting the performance of the final products, such as the percentage of stabilizers, compaction moisture content, and compaction delay time must be evaluated by laboratory mix design tests (Chen et al. 2011; Winterkorn and Pamukcu 1991). Additionally, certain issues specific to the chemical stabilizers need to be carefully considered. For example, physical and chemical properties of self-cementing fly ash can vary significantly between plants due to different chemical components of the source coal material used (White et al. 2005).

Bentonite (sodium montmorillonite clay) has also been successfully used for dust reduction on limestone-surfaced roads. Bergeson and Wahbeh (1990) and Bergeson et al. (1995) conducted comprehensive laboratory and field evaluations, and showed that the negatively charged surfaces of the clay particles interacting with positively charged limestone surfaces effectively bond the fine particles to the large limestone particles. Their laboratory tests also demonstrated that the bentonite could significantly increase the compressive strength and improve the slaking

characteristics of crushed limestone materials. Compared to calcium and magnesium chloride surface treatments for dust control of granular-surfaced roads, bentonite treatments were 2 to 3 times less effective, but the bonding capability of bentonite lasted four to six times longer than chloride treatments (Bergeson et al. 1995).

3.3.3. Geosynthetics

Nonwoven (NW) geotextiles, biaxial (BX) geogrids, and geocomposites are typically placed between subgrades and base layers to provide separation, reinforcement, and subsurface drainage for road systems. Many previous studies have shown that geotextiles and geogrids are effective for improving bearing capacity and preventing material migration, enabling base layer thicknesses to be reduced (e.g., Abu-Farsakh et al. 2016; Douglas and Valsangkar 1992; Fannin and Sigurdsson 1996; Freeman 2006; Hufenus et al. 2006; Latha et al. 2010). The mechanisms, benefits, and construction methods for use of geogrids and geotextiles to stabilize granular surface and base layers have been discussed in many publications (Giroud 2009; Giroud and Han 2004a; Holtz et al. 2008; Tingle and Webster 2003). Giroud and Han (2004a; 2004b) also developed a theoretically based design method for determining the thickness of the base course of geogrid-stabilised granular-surfaced roads.

Geocomposite materials are commonly used as drainage layers and capillary barriers to improve subsurface drainage and frost susceptibility of road systems. Geocomposite drainage layer performance has been assessed for both paved and unpaved roads using laboratory, field, and numerical evaluations (e.g., Bahador et al. 2013; Christopher et al. 2000; Henry and Holtz 2001; Henry et al. 2005; Stormont et al. 2001). From these studies, it can be generally concluded that geocomposite drainage layers help to keep the upper layers of soil relatively dry, and reduce plastic deformation through combined mechanical and hydraulic action. Christopher et al. (2000)

evaluated different placements of geocomposite drainage layers and found that geocomposites placed within the subgrade were quickest at removing water from the road system during spring thaws.

3.4. Test Section Design, Materials, Construction Methods, and Costs

The following subsections describe the pre-construction conditions of the test site and detail the design approaches, materials, construction procedures, and costs of the test sections.

3.4.1. Preconstruction conditions of the test site

The selected 3.2 km stretch of granular-surfaced road was a heavily used farm-to-market road with an 8.5 m nominal width, and a very flat vertical profile and similar drainage conditions along its length. According to the Iowa DOT (2011), the annual average daily traffic (AADT) was 130 vehicles. County officials reported that maintenance of the selected road required at least two motor grader bladings per week during harvest and planting seasons, and approximately 200 metric tons of virgin aggregate per kilometer annually, resulting in an annual maintenance cost of $1.00 per square meter of roadway surface area. Based on personal communications with the county officials, the roadway embankment was constructed using the existing natural soil. Additionally, according to the Natural Resources Conservation Service (NRCS) web soil survey database, the two main soil types present at the test site have nearly identical soil index and physical properties, and were therefore considered to be practically the same material for this study. To determine the actual soil index properties and support conditions of the subgrade materials, laboratory soil classification and California bearing ratio (CBR) tests were performed prior to construction using relatively dry conditions in accordance with ASTM D422 and ASTM D1883. The test results are summarized in Table 3.2.

Table 3.2. Pre-construction lab test results of the subgrade and existing surface aggregate.

Parameter	Subgrade	Existing Surface Aggregate
Gravel content (%)	0.9	25.7
Sand content (%)	39.8	57.1
Silt content (%)	30.6	
Clay content (%)	28.7	17.2 a
D10 (mm)	–	–
D30 (mm)	0.003	0.282
D60 (mm)	0.081	2.489
Liquid limit (%)	43	
Plastic limit (%)	22	NP
USCS classification	CL	SM
CBR (%)	5	26

[a] Percentage shown includes both silt and clay content.

3.4.2. Macadam stone base (MSB) sections

In this study, nine sections with MSB layers overlain by choke stone and road stone were constructed over the first 1.6 km of roadway, and one unmodified section was used as a control, as shown in Figure 3.1(a). Design and construction of the MSB sections essentially followed the empirical recommendations of the previous studies discussed in Section 3.3.1. However, three macadam types; dirty, clean, and recycled Portland cement concrete (RPCC) were used to construct the base layers of the test sections, as shown in Figure 3.2. The clean macadam material met the Iowa DOT specifications for gradation of macadam stone materials, which requires 76.2 mm nominal maximum size screened over a 25.4 or 19.1 mm screen (Iowa DOT (2012)). However, the dirty macadam and RPCC macadam had a maximum size of 125 mm and contained 44% and 19% particles passing 4.75 mm sieve, respectively. These two materials can therefore be considered as marginal.

Calcium chloride sprayed on the surface

50 mm Road Stone (GP-GM)

50 mm Choke Stone (GP-GM)

150mm Road Stone + Choke Stone + 5% Bentonite

50 mm Road Stone

50 mm Choke Stone

150 mm Road Stone + Choke Stone + 5% Bentonite

50 mm Road Stone

50 mm Choke Stone

150 mm Dirty Macadam (GM)

NW-geotextile

150 mm Clean Macadam (GP)

150 mm RPCC Macadam (GP)

75 mm Existing Aggregate (SM)

Subgrade (CL)

| 518 m | 76 m | 168 m | 76 m | 72 m | 157 m | 152 m | 152 m | 145 m | 100 m |

(a) The First 1.6-km Test Sections

30

75~ 130 mm Existing Agg. (SM)

GC-1 liner

150 mm road stone +5% Bentonite

25 mm Road Stone

200 mm SG+AGG+ 15% FA

200 mm SG+AGG+ 6% Cement

200 mm Road Stone

100 mm Existing Agg.

Subgrade (CL)

GC-2

BX-geogrid+ NW-geotextile

BX-geogrid

| 281 m | 105 m | 105 m | 122 m | 183 m | 183 m | 183 m | 183 m | 91 m | 91 m | 80 m |

(b) The Second 1.6-km Test Sections

Figure 3.1. Nominal cross-section profiles of the (a) first and (b) second 1.6-km of test sections (not to scale).
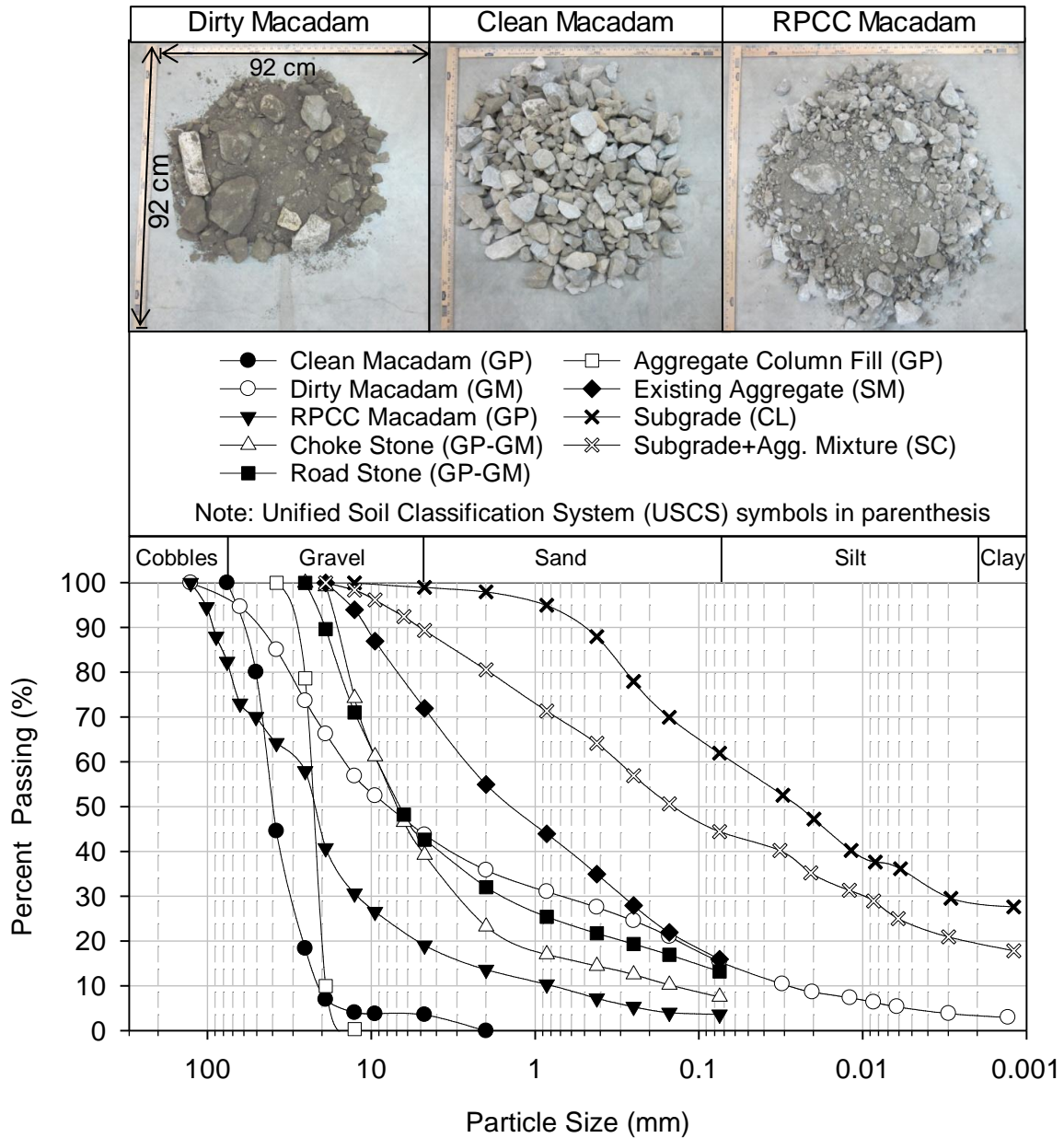
Figure 3.2. Photos of the dirty, clean, and RPCC macadam materials, and gradation curves of all geomaterials used in this study.

During construction, the macadam stone materials were placed on top of the existing surface aggregate using a Jersey spreader, then compacted to a final nominal thickness of 150 mm using approximately six passes of a vibratory roller with a gross weight of 13,000 kg. A choke stone drainage layer was placed and compacted over the MSB layers using the same equipment and methods, followed by a road stone layer as a wearing surface, with nominal thicknesses of

50 mm for each. The gradations of the choke and road stones are also shown in Figure 3.2. A layer of NW-geotextile was placed at the interface of the MSB and choke stone layers for four sections to facilitate drainage and prevent contamination of the macadam materials by fines migrating between the surface and base layers (Figure 3.1(a)). For one of the dirty macadam sections, an owner of an adjacent property sprayed a calcium chloride surface treatment for dust control with unknown concentration eight months after construction. Two of the dirty macadam sections had bentonite (sodium montmorillonite) mixed with the existing and additional virgin road stone at a rate of 5% by dry mass, which increased the thickness of the road stone layer by approximately 50 mm as shown in Figure 3.1 (a).

3.4.3. Aggregate column sections

On the second 1.6 km of the test site, two aggregate column sections were constructed between two drainage tiles crossing beneath the roadway, where frequent frost boils were reported to occur during spring thaws. To facilitate subsurface drainage, 0.2 m-diameter holes were augured to a depth of 1.8 m to extend below the local seasonal frost line, then backfilled with clean aggregate (Figure 3.2) without compaction. The spacing of the columns was selected to give one column per 20 square meters of roadway surface area. For one of the two aggregate column sections, the perimeters of the bottom 1.2 m of the holes were lined with GC-1 geocomposite to prevent contamination by fines from the surrounding subgrade.

3.4.4. Geosynthetic sections

Three sections with embedded geosynthetics were also designed and constructed to either increase bearing capacity or improve subsurface drainage. A GC-2 geocomposite layer, a BX-geogrid on top of the NW-geotextile, and the BX-geogrid alone were placed at the subgrade and surface-aggregate interface for three sections of the second 1.6 km of roadway (Figure 3.1(b)).

To determine the required thickness of the surface aggregate layer for the BX geogrid-stabilised sections, a design method developed by Giroud and Han (2004a; 2004b) was followed in this study. The design method uses rutting depth as the failure criterion. Compared to other design methods that consider only the subgrade strength and traffic load and volume, this method also considers the distribution of vertical stress applied at the aggregate-subgrade interface, strength of the surface aggregate material, interlocking between geogrid and the aggregate material, and geosynthetic stiffness through Equation (3.1). The required thickness h must be determined iteratively, as it appears on both sides of the equation. Additional details on the development, derivation, and calibration of the design method are provided in Giroud and Han (2004a; 2004b).

$$h = \frac{0.868 + (0.661 - 1.006J^2)\left(\dfrac{r}{h}\right)^{1.5} \log N}{f_E} \times \left[\sqrt{\frac{P/(\pi r^2)}{m N_c f_C CBR_{SG}}} - 1\right] r \quad (3.1)$$

where h is the thickness of surface aggregate layer (m); J is the aperture stability modulus of geogrid (m-N/°); r is the radius of equivalent tire contact area (m^2); N is the number of axle passes; CBR_{SG} is the CBR of the subgrade (%); f_E is the modulus ratio factor, calculated based on CBR of the surface aggregate and subgrade; P is the axle load (kN); m is the bearing capacity mobilization coefficient; N_c is the bearing capacity factor; and f_C is the ratio of undrained cohesion and CBR_{SG}.

The design inputs used in Equation (3.1) for this study are summarized in Table 3.3. The rest of the parameters in the equation, including f_E, m, N_c, and f_C are either calculated using the design inputs or constants calibrated by Giroud and Han (2004b). Using these values, the required thickness of the surface aggregate was determined to be 217 mm.

Table 3.3. Design inputs for determining thickness of surface aggregate layer of geogrid-stabilized sections.

Design Input	Value
Failure Criterion	
Allowable rut depth (mm)	75 [a]
Traffic Load and Volume	
Axle load, *P* (kN)	80 [b]
Hot inflation pressure, *p* (kPa)	830 [c]
Estimated daily number of *ESALs*	45 [d]
Number of axles per vehicle	2
Design service life (years)	10
Number of passes of axle (*N*)	284,700
Properties of Materials	
Lab-soaked *CBR* of base course (%)	26
Lab-soaked *CBR* of subgrade (%)	4 [e]
Aperture stability moduli of geogrid, *J* (m-N/°)	0.32 [f]

[a] Used by the AASHTO (1993) and the U.S Army of Corps of Engineers (Hammitt and Aspinall 1970).

[b] Equivalent single axle load (*ESAL*) specified in the AASHTO (1993).

[c] A default hot inflation pressure used in the Mechanistic-Empirical Pavement Design Guide (AASHTO 2004).

[d] Assuming the number of *ESALs* is 30% of the reported AADT (i.e., 130).

[e] The design method is valid for subgrade with a *CBR* less than 5%, so used 4% for design (the lab-measured CBR_{SG} was 5% as shown in Table 3.2).

[f] From manufacture's product datasheet for the geogrid used in this study.

3.4.5. Chemical stabilization sections

Three chemical stabilization sections were constructed on the second 1.6 km of road (Figure 3.1(b)). A full depth reclaimer (FDR) was used to incorporate the stabilizers into the existing surface and subgrade materials. For one section, five percent bentonite (sodium montmorillonite) by dry mass was mixed with the existing surface aggregate to reduce dust and improve stability of the section. To compare relative performance between the geosynthetics sections and those stabilised with commonly used active chemical stabilizers, 6% type I/II Portland cement and 15% self-cementing fly ash by dry mass were incorporated into a 200 mm SG+AGG surface layer, by blending the nominally 75-mm thick existing surface aggregate layer with 125 mm of subgrade. The gradation of the SG+AGG mixture is shown in Figure 3.1(b). Before construction of the test sections, laboratory mix designs were also performed to determine the moisture-

density-strength relationships for the fly ash- and cement-stabilised mixtures. The mix design results were used to control the compaction moisture contents and compaction delay times during construction. After mixing and compaction of the bentonite-, fly ash-, and cement-stabilized sections, a 25 mm thick layer of road stone was spread on the roadway surface to minimize wearing and retain moisture during curing.

3.4.6. Construction costs

A breakdown of construction costs for all test sections is presented in Figure 3.3. The short distances of the test sections somewhat inflate the costs, which should therefore only be used to compare relative initial costs of the different stabilization methods rather than to serve as cost estimates for real projects. Additionally, the construction costs of the bentonite-treated macadam sections would be greatly reduced if the bentonite were incorporated during construction instead of several months later.
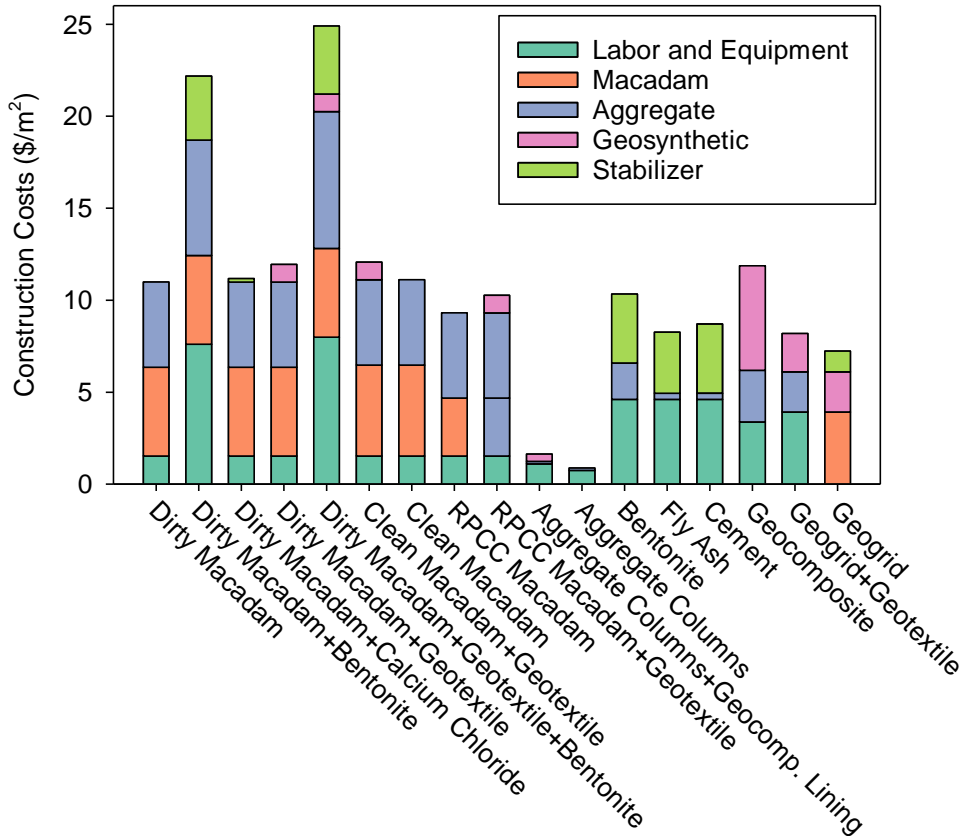
Figure 3.3. Construction costs per square meter of the test sections.

3.5. Field Tests and Statistical Analysis Methods

The strength and stiffness of the different material layers of a road significantly influence the performance and durability of the overall system. Additionally, the elastic moduli and CBR values of a given material layer are important inputs for both empirical and mechanistic-based design methods. Therefore, dynamic cone penetrometer (DCP) and falling weight deflectometer (FWD) tests were performed in this study to compare the strength and elastic modulus of the multiple material layers of the test sections. Statistical analyses were also conducted on the FWD test data to provide a basis for comparisons between the various stabilization methods.

Construction of the test sections was completed in two separate stages (fall 2013 for the first 1.6 km and fall 2014 for the second), and two corresponding series of field tests were conducted in 2013 and 2014 to evaluate the as-constructed performance. The chloride and bentonite surface

treatments had not yet been applied on the dirty macadam sections during the first group of tests in 2013. The second group of tests in 2014 were conducted on all test sections to compare the newly constructed sections with the MSB sections, and to determine the stiffness changes of the MSB sections after the first year of service.

3.5.1. Dynamic cone penetrometer tests

DCP tests were performed to determine the thickness and shear strength of the surface aggregate layer and subgrade in accordance with ASTM 6951-09 (2013). The test involves driving a conical point with a base diameter of 20 mm, using an 8 kg hammer dropped a distance of 575 mm, and measuring the penetration distance in mm per blow, referred to as the DCP Index (DCPI). The empirical correlations for estimating the in situ CBR values recommended in the ASTM standard are given by Equations (3.2) and (3.3) below;

$$CBR = \frac{292}{DCPI^{1.12}} \qquad \text{(for } CBR>10)$$

(3.2)

$$CBR = \frac{1}{\left(0.017019 \times DCPI\right)^2} \qquad \text{(for CL soils with } CBR<10)$$

(3.3)

The thickness of each material layer and its weighted-average CBR can be calculated from the DCP test data, with boundaries between the layers typically identifiable by sudden changes in the slope of the cumulative blows versus depth profile.

In the following results, CBR_{AGG} and CBR_{SG} denote the weighted-average CBR of the surface aggregate and subgrade layers, respectively. According to ASTM D1883, the DCP test should not be used for granular materials containing a large percentage of aggregates larger than 50 mm. Hence, the CBR_{AGG} values of the MSB sections may be exaggerated due to the DCP cone encountering large macadam stones. The DCP test results also do not clearly delineate the boundaries between the MSB layers and the aggregate layers above and below, due to similar

shear resistances of these materials. Therefore, the MSB sections were analyzed as two-layered systems consisting of a single combined surface aggregate layer (i.e.,

aggregate + MSB+ aggregate) on top of a subgrade layer. The average thickness of the surface aggregate layer for each section was used as input for analysis of the FWD test data, to calculate multi-layered elastic moduli as described below.

3.5.2. Falling weight deflectometer tests

FWD tests were conducted using a Kuab Model 150 2m FWD, with a 300 mm diameter segmented loading plate to provide a uniform stress distribution on the roadway surface. For each test location, a 53 kN dynamic impact load was applied on the plate, resulting in an applied pressure of 755 kPa. A single equivalent composite elastic modulus ($E_{Composite}$) for the surface aggregate layer and subgrade was then calculated based on Boussinesq's solution as given in Equation (3.4).

$$E_{Composite} = \frac{\left(1-v^2\right)\sigma_0 A}{d_0} \times f$$

(3.4)

where $E_{Composite}$ is the composite elastic modulus (MPa); d_0 is the measured deflection at the center of the loading plate (mm); v is the Poisson's ratio (assumed to be 0.4); σ_0 is the normalized applied peak stress (MPa); A is the radius of the plate (mm); and f is the shape factor assumed to be 2 for a uniform stress distribution (Vennapusa and White 2009).

The FWD test data were also used to calculate separately the elastic modulus E_{AGG} of the surface aggregate layer and E_{SG} of the subgrade layer, using an approach detailed in AASHTO (1993) which combines Boussinesq's solution and Odemark's equivalent layer thickness assumption.

3.5.3. Statistical Analysis Methods

Dunnett's T3 test is a pairwise multiple-comparison procedure valid for unequal sample sizes and variances, which is based on a Studentized maximum modulus distribution (Dunnett 1980). Compared to other multiple-comparison procedures for unequal variances, the T3 procedure is recommended for small sample sizes (Hochberg and Tamhane 1987). The average elastic modulus (μ) values between two sections were declared statistically significantly different if their absolute mean difference was greater than the test statistic as shown in Equation (3.5). The Satterthwaite approximate degree of freedom ($\hat{v}$) can be calculated using Equation (3.6). The test statistics and probability values were calculated using the Statistical Package for the Social Sciences (SPSS) software package.

$$\left| \mu_i - \mu_j \right| \geq SMM_{\alpha,k^*,\hat{v}} \sqrt{s_i^2 / n_i + s_j^2 / n_j} \tag{3.5}$$

$$\hat{v} = \frac{\left(\dfrac{s_i^2}{n_i} + \dfrac{s_j^2}{n_j} \right)^2}{\dfrac{s_i^4}{n_i^2 v_i} + \dfrac{s_j^4}{n_j^2 v_j}} \tag{3.6}$$

where $SMM_{\alpha,k^*,v}$ is the critical value of the Studentized maximum modulus distribution; α is the significance level (0.05 in this study for a 95% confidence level), $k^*=k\times(k-1)/2$ is the total number of pairwise comparisons; n_i and n_j are the number of measurements for two test sections; s_i and s_j are the standard deviations of the elastic moduli for two test sections; v_i and v_j are the numbers of degrees of freedom for two test sections (e.g., n_i - 1).

The two groups of FWD tests in 2013 and 2014 were conducted at approximately the same locations in the MSB sections, therefore the paired t-test was used to statistically assess the

durability of the MSB sections. In this sense, a decrease in the elastic modulus was considered indicative of a reduction in durability. The null hypothesis (H_0) was that the difference ($\bar{d}$) between the mean elastic modulus of the as-constructed and one year post-construction tests was zero for a given test section. The corresponding standard deviations (S_d) for the n pairs of measurements for each test section were used to calculate the test statistic (t) using Equation (3.7);

$$t = \frac{\bar{d} \times \sqrt{n}}{S_d}$$

(3.7)

If the $|t|$ value is greater than or equal to the critical $t_{(\alpha/2)}$ for a two-tailed test with a 95% confidence level (i.e., $\alpha = 0.05$), it can be concluded that the average elastic modulus of the test section either significantly increased or decreased between the two groups of tests.

3.6. As-Constructed Stiffness and Strength of the MSB Sections

The first group of DCP and FWD tests were performed in November, 2013 to measure the as-constructed mechanistic properties of the MSB and control sections in the first 1.6 km. The DCP test results indicated that the thicknesses of the combined surface layers of the MSB sections were relatively uniform, ranging from 340 to 400 mm, whereas the average thickness of the control section was only 125 mm. The elastic moduli of the test sections calculated from FWD test results are shown in Figure 3.4. The $E_{Composite}$ values of each section show small variations, but obvious differences are evident between average values of the sections. The clean macadam shows the highest average value (260 MPa), and the average $E_{Composite}$ values of all the MSB sections are more than 2.5 times higher than the control section. However, depending on the macadam types, the average $E_{Composite}$ of the sections with an embedded NW-geotextile layer were 14% to 25% lowered than the corresponding sections without the geotextile.

Compared to the $E_{Composite}$ values, the E_{AGG} values of the surface aggregate layers exhibit more variation (Figure 3.4(b)). Additionally, the average E_{AGG} values of the MSB sections containing the NW-geotextile layer are consistently lower than the corresponding MSB sections without the NW-geotextile, but are still higher than those of the control section. For the subgrade, the average E_{SG} values reported in Figure 3.4(c) are relatively consistent across the different MSB sections. However, the average E_{SG} values underneath the MSB sections are approximately 1.5 times those of the control section. This indicates that the subgrade of the MSB sections was improved relative to the control section, possibly due to the increased confining stresses from the surcharge of the macadam layers. This hypothesis is also consistent with the lower E_{SG} in the RPCC macadam sections compared to the dirty and clean macadam sections, because the RPCC macadam layer applied a lower surcharge due to its lower unit weight.

The CBR_{AGG} and CBR_{SG} correlations calculated from the DCP test data are plotted along with the FWD test results in Figure 3.4, showing that the trends of CBR- and FWD-derived values generally agree. As previously discussed, the few high CBR_{AGG} values in Figure 3.4(b) may be due to the DCP cone encountering large macadam stones. For the subgrade, most of the CBR_{SG} values of the MSB sections are also higher than the control section. Some discrepancies between moduli derived from FWD and CBR tests are to be expected, due to the significantly different volumes of material involved in the two tests.

42
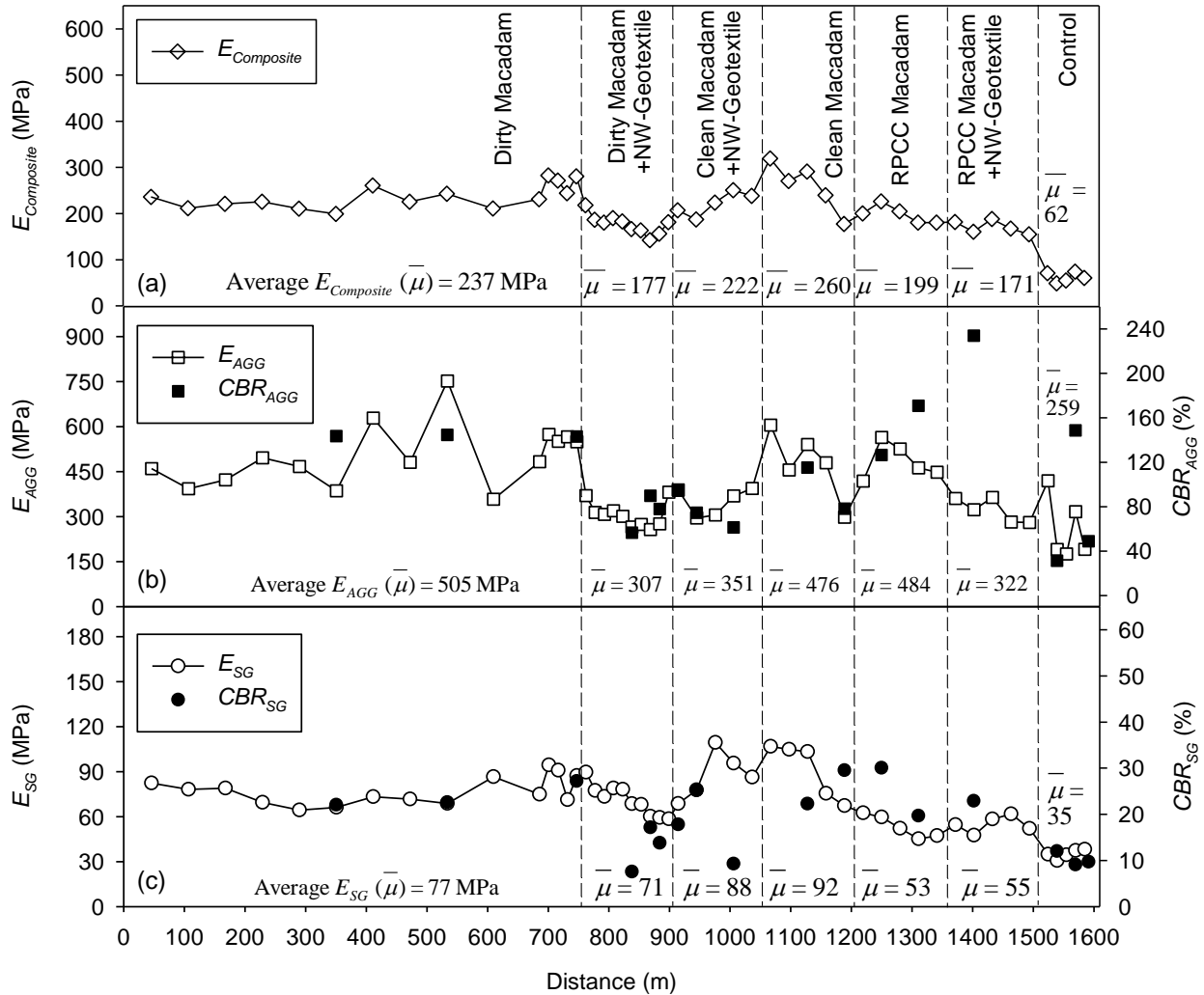
Figure 3.4. As-constructed FWD and DCP test results for the MSB and control sections in the first 1.6 km: (a) $E_{Composite}$, (b) E_{AGG} and CBR_{AGG}, (c) E_{SG} and CBR_{SG}.

Results of Dunnett's T3 test for the FWD data verified that the average $E_{Composite}$ values of all the MSB sections are statistically higher than the control section (Table 3.4). However, the clean macadam section with the highest average $E_{Composite}$ of 260 MPa is not statistically significantly different from other MSB sections due to its relatively large variation and small sample size (Figure 3.4(a)). The T3 test results also indicate that the NW-geotextile embedded in the dirty MSB sections resulted in significantly lower average $E_{Composite}$ values.

For the average E_{AGG} of the surface layers, the statistical analysis results show no statistical differences between the three macadam types, but the dirty and RPCC macadam section moduli are significantly higher than the corresponding sections with the NW-geotextile. For the subgrade, the results also support the previous explanations that the subgrade stiffness (E_{SG}) of the MSB sections are significantly improved compared to the control section, and that the RPCC material with its lower unit weight showed significantly less increase in the subgrade stiffness than the dirty and clean macadam materials.

Table 3.4. Dunnett's T3 test results for as-constructed elastic moduli of MSB and control sections in the first 1.6 km.

Pairwise Multiple Comparisons		Probability Values [a]		
		$E_{Composite}$	E_{AGG}	E_{SG}
Clean macadam	Dirty macadam	0.996	1.000	0.813
	RPCC macadam	0.475	1.000	0.078
	Dirty macadam + geotextile	0.215	0.238	0.515
	Clean macadam + geotextile	0.910	0.525	1.000
	RPCC macadam + geotextile	0.173	0.316	0.094
	Control	0.010	0.181	0.022
Dirty macadam	RPCC macadam	0.086	1.000	0.006
	Dirty macadam + geotextile	<0.001	<0.001	0.923
	Clean macadam + geotextile	0.977	0.007	0.920
	RPCC macadam + geotextile	<0.001	0.001	0.001
	Control	<0.001	0.041	<0.001
RPCC macadam	Dirty macadam + geotextile	0.645	0.012	0.047
	Clean macadam + geotextile	0.838	0.065	0.061
	RPCC macadam + geotextile	0.340	0.021	1.000
	Control	<0.001	0.068	0.040
Dirty macadam + geotextile	Clean macadam + geotextile	0.135	0.766	0.594
	RPCC macadam + geotextile	1.000	1.000	0.026
	Control	<0.001	0.992	<0.001
Clean macadam + geotextile	RPCC macadam + geotextile	0.082	0.993	0.077
	Control	<0.001	0.762	0.015
RPCC macadam + geotextile	Control	<0.001	0.958	0.005

[a] Shaded values indicate that difference between two average elastic moduli is statistically different at the 95% confidence level.

3.7. Stiffness Comparisons for All Test Sections

The second group of FWD tests were performed on all sections following completion of construction in October, 2014, at which time the chemical stabilization sections had cured 20 days. A weather station installed on the project site showed that the cumulative rainfall was 62 mm during the curing time. The FWD test results are presented in Figure 3.5. The five control sections were combined due to their relatively small variations. Relative to other stabilized sections, all the MSB sections constructed one year prior still exhibited higher average $E_{Composite}$ values (Figure 3.5(a)). Among the rest of the sections, the fly ash- and cement-stabilized sections exhibited the highest average $E_{Composite}$ values. However, significant variations were observed within the cement-stabilized section. Based on observations during construction, the large variation was caused by non-uniform mixing, as much more aggregate was incorporated into the SG+AGG+cement mixture than the designed proportion (38% surface aggregate + 62% subgrade by volume). The aggregate column and geocomposite sections were designed to improve the subsurface drainage rather than increase stiffness, and therefore yielded $E_{Composite}$ values similar to the control sections. Because the FWD tests were conducted under dry conditions, the benefits of the improved subsurface drainage are not apparent. The elastic modulus values for the bentonite section were also not significantly higher than the control sections. Based on visual observations, bentonite can effectively reduce dust and loss of fines and provide a much tighter road surface than all the other sections, which can bring some long-term benefits to the system.

For the surface layer, Figure 3.5(b) shows that the active stabilizers (i.e., fly ash and cement) yielded much higher E_{AGG} values than the other stabilization methods, followed by the BX-geogrid and RPCC macadam sections. The surface layer thickness of the RPCC macadam section was nominally 50 mm thicker than the fly ash-, cement-, and geogrid-stabilized sections,

but the construction costs of the four sections were approximately the same. Additionally, the E_{AGG} values of the RPCC macadam section show less variations than the fly ash, cement, and geogrid sections. The average E_{AGG} values of the rest of the clean and dirty MSB sections were at about the same level, but sections with a layer of NW-geotextile consistently resulted in lower average E_{AGG} but less variation than the corresponding sections without the NW-geotextile. To compare the subgrade stiffness, Figure 3.5(c) also shows that the E_{SG} values of the dirty and clean macadam sections remained higher than other sections, as was observed from the first group of tests in 2013. Also, the subgrade of the aggregate column sections showed lower average values than the control section as expected. As mentioned previously, the two sections were constructed between two drainage tiles crossing beneath the roadway where frequent frost boils were reported to occur during spring thaws, so the subgrade likely has higher moisture contents than the other sections. The geocomposite section yielded the lowest elastic moduli among all the sections. This is because the specific geocomposite (GC-2) used in this study contains a flexible middle geonet layer, which may yield a much higher elastic deformation under the heavy FWD impact load, resulting in much lower elastic moduli. One month after construction of the geocomposite section, a field investigation was conducted to visually examine the quality of the geocomposite material. Geocomposite samples dug out from three different locations showed no damage on either the geonet core or the outer NW-geotextile layers, which may indicate that most deformations of the material are recoverable.
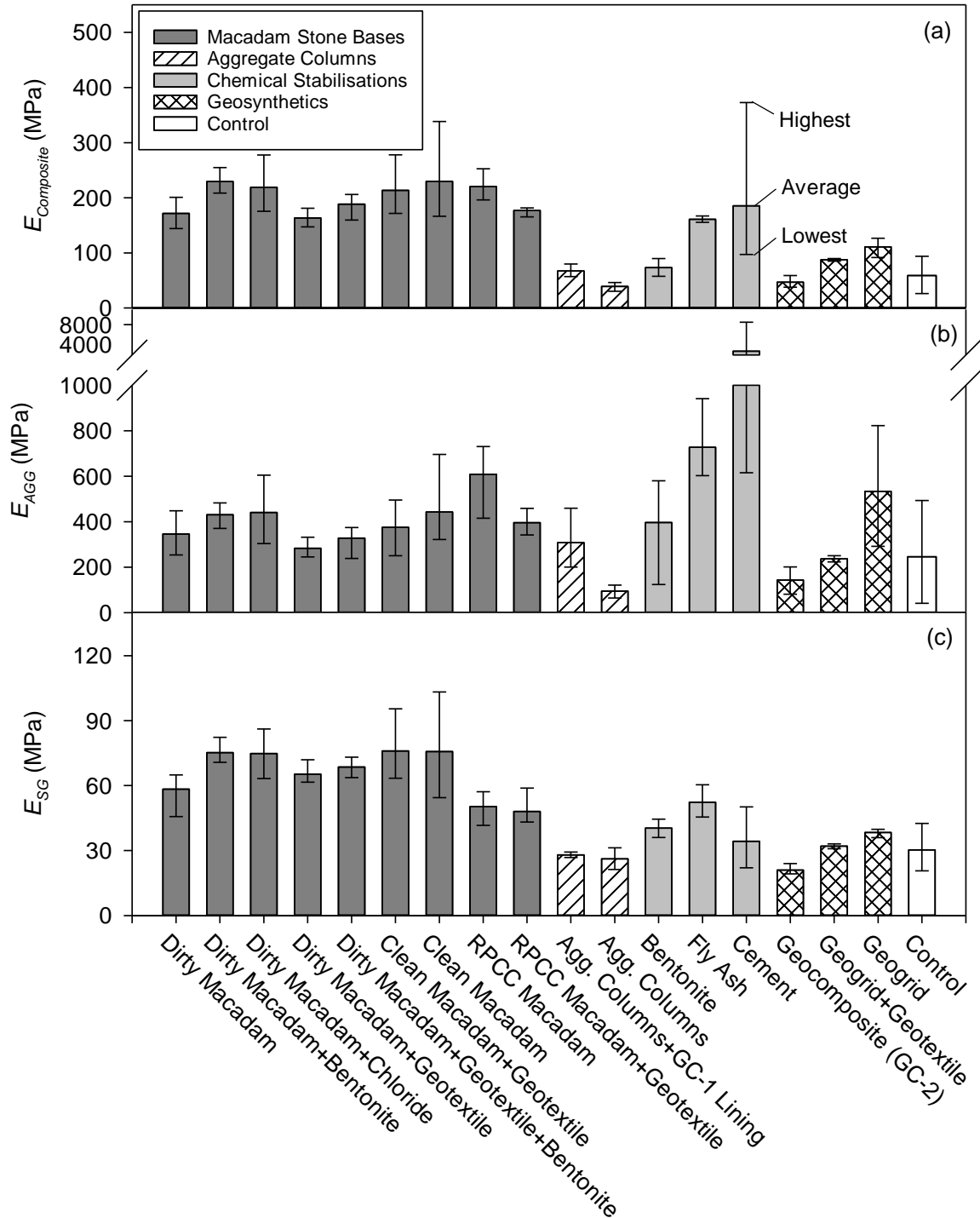
Figure 3.5. Results from second group of FWD tests conducted on all test sections in 2014: (a) $E_{Composite}$, (b) E_{AGG}, and (c) E_{SG}.

Dunnett's T3 test was also used to statistically assess which of eight selected stabilization methods performed best in terms of increasing the stiffness (Table 3.5). Because larger groups of

pairwise comparisons can reduce the power of the analysis, the MSB sections with NW-geotextile and surface treatments as well as the sections aimed at improving subsurface drainage were not included. The results in Table 3.5 reveal that most of the stabilised sections yield significantly higher $E_{Composite}$ values than the control sections, except for the bentonite and cement sections. The average $E_{Composite}$ of the dirty macadam, RPCC macadam, and fly ash sections are significantly higher than the geogrid-stabilised section. For the surface aggregate layers, only the RPCC macadam and fly ash sections yield significantly higher average modulus than the control sections. Due to the large variations within the cement and clean macadam sections, larger sample sizes are needed to ensure the validity of the statistical conclusions.

Table 3.5. Dunnett's T3 test results for comparing elastic moduli of eight selected sections.

Pairwise Multiple Comparisons		$E_{Composite}$ (MPa)		E_{AGG} (MPa)		E_{SG} (MPa)	
		$\mu_i - \mu_j$ [a]	Prob. [b]	$\mu_i - \mu_j$ [a]	Prob. [b]	$\mu_i - \mu_j$ [a]	Prob. [b]
Clean macadam	RPCC macadam	230−220	1.000	443−609	0.775	76−50	0.296
	Dirty macadam	230−172	0.746	443−346	0.950	76−58	0.649
	Fly ash	230−161	0.561	443−728	0.203	76−52	0.364
	Cement	230−139	1.000	443−1334	0.875	76−30	0.052
	BX-Geogrid	230−111	0.149	443−534	1.000	76−38	0.092
	Bentonite	230−73	0.058	443−397	1.000	76−40	0.107
	Control	230−46	0.044	443−133	0.412	76−30	0.044
RPCC macadam	Dirty macadam	220−172	0.129	609−346	0.096	50−58	0.538
	Fly ash	220−161	0.064	609−728	0.956	50−52	1.000
	Cement	220−139	1.000	609−1334	0.913	50−30	0.261
	BX-Geogrid	220−111	0.002	609−534	1.000	50−38	0.104
	Bentonite	220−73	<0.001	609−397	0.765	50−40	0.218
	Control	220−46	0.000	609−133	0.018	50−30	0.007
Dirty macadam	Fly ash	172−161	0.964	346−728	0.025	58−52	0.820
	Cement	172−139	1.000	346−1334	0.850	58−30	0.049
	BX-Geogrid	172−111	0.006	346−534	0.841	58−38	<0.001
	Bentonite	172−73	<0.001	346−397	1.000	58−40	0.001
	Control	172−46	<0.001	346−133	0.399	58−30	<0.001
Fly Ash	Cement	161−139	1.000	728−1334	0.936	52−30	0.167
	BX-Geogrid	161−111	0.041	728−534	0.900	52−38	0.044
	Bentonite	161−73	0.001	728−397	0.295	52−40	0.082
	Control	161−46	<0.001	728−133	0.005	52−30	0.002
Cement	BX-Geogrid	139−111	0.912	1334−534	0.898	30−38	0.999
	Bentonite	139−73	0.597	1334−397	0.865	30−40	0.971
	Control	139−46	0.481	1334−133	0.823	30−30	0.999
BX-Geogrid	Bentonite	111−73	0.099	534−397	0.999	38−40	0.988
	Control	111−46	0.015	534−133	0.514	38−30	0.005
Bentonite	Control	73−46	0.843	397−133	0.925	40−30	0.013

[a] Difference in average elastic modulus between two sections.
[b] Shaded values indicate that difference between two average elastic moduli is statistically different at the 95% confidence level.

3.8.   Stiffness Changes of the MSB Sections One Year Post-Construction

Because the second group of FWD tests, performed in 2014, were also conducted on the

MSB sections at the same test locations as the first group of tests in 2013, the stiffness changes

of the MSB sections during one year of service can be determined. Based on visual observations,

the weather and road conditions were similar during the two test periods. The road surface

temperatures were also measured at each testing point by the FWD during the two groups of tests, showing that the average value in each year differed by 4°C. The FWD test results are summarized by the boxplots in Figure 3.6. The $|t|$ and probability (Prob.) values of the paired t-test are also shown for the sections that yield a statistically significant stiffness change.

The dirty macadam section yielded the largest reduction in average $E_{Composite}$ (~23%) and E_{AGG} (~26%), whereas the clean macadam section's stiffness did not significantly change as shown in Figure 3.6(a) and Figure 3.6(b). The results also show that the dirty and clean macadam sections with NW-geotextile experienced smaller relative reductions in average E_{AGG} than the corresponding sections without NW-geotextile. This phenomenon may suggest that the NW-geotextile can enhance long-term durability due to improved subsurface drainage and reduced contamination of the MSB by migrating fines. Most notably, due to the beneficial effects of further hydration of the RPCC material, the average E_{AGG} of the RPCC macadam section increased by 25% one year post-construction, resulting in an 11% increase in the composite stiffness $E_{Composite}$ of the system. Similar increases were also observed for the RPCC macadam with NW-geotextile section. Additionally, Figure 3.6(c) shows that the clean and RPCC macadam sections experienced smaller decreases in the average E_{SG} values than the dirty macadam sections. This may be because the large voids between the clean macadam stones can efficiently drain water out of the system and the low permeability of the RPCC material can impede water from infiltrating to the subgrade during wet seasons. These hypotheses are supported by a recent study on performance of RPCC materials under pavements, which found that RPCC materials stiffen over time and generally have lower permeability than virgin aggregate materials (White et al. 2008).
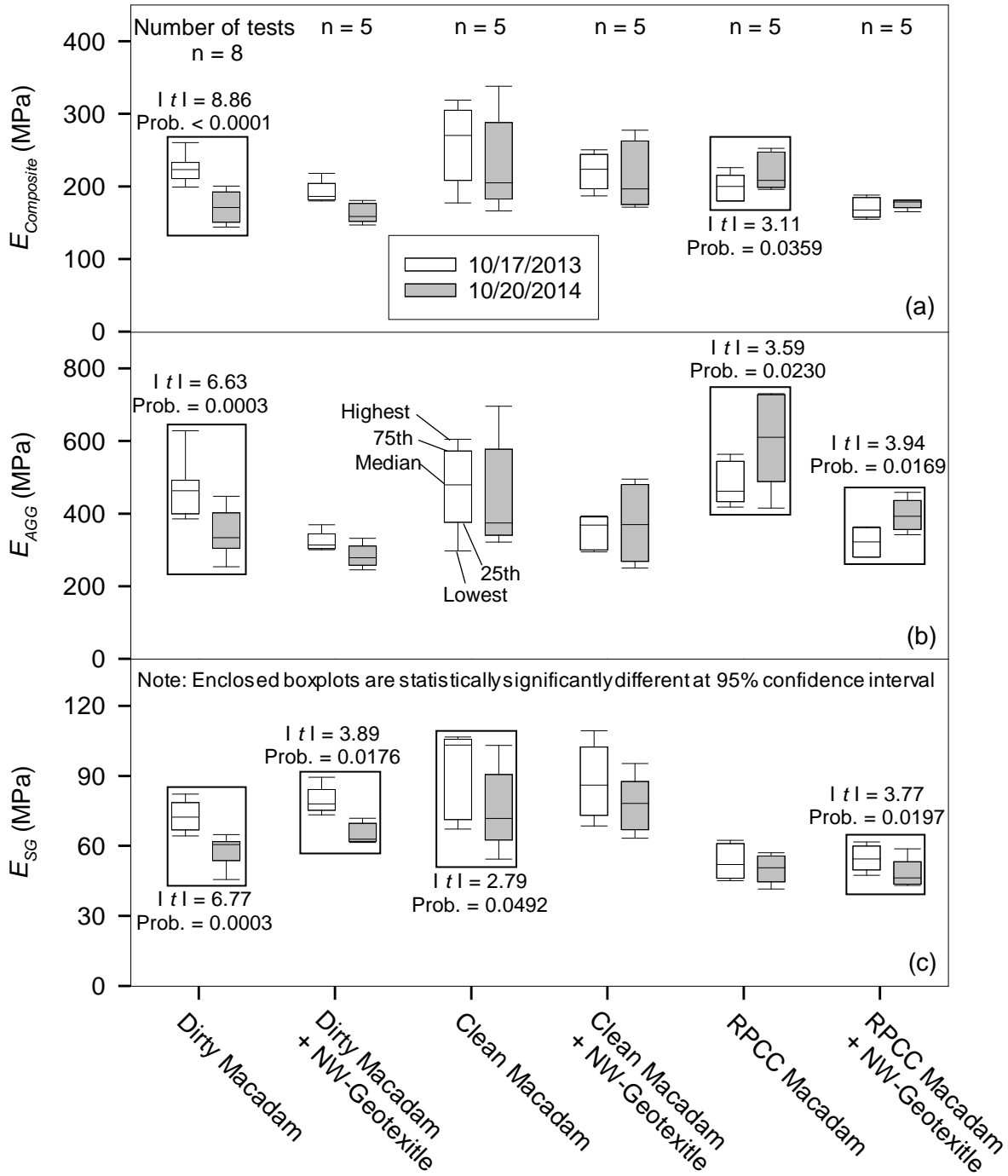
Figure 3.6. Summary boxplots of as-constructed and one year post-construction FWD test results for MSB sections: (a) $E_{Composite}$**, (b)** E_{AGG}**, and (c)** E_{SG}**.**

3.9. Summary and Conclusions

The objective of this study was to identify the most cost-effective technologies to improve performance and durability of granular surface and base layers of low-volume roads. Based on the comprehensive literature review results, a total of nine geomaterials, three chemical stabilizers, and three types of geosynthetics were selected to construct various test sections over a 3.22 km stretch of granular-surfaced road. The design methods, construction procedures and costs, and mechanical properties of the test sections were presented and statistically analyzed.

The construction costs of the test sections varied within a small range, except for the MSB sections with bentonite surface treatment, which had the highest costs, and the aggregate column sections, which had the lowest costs. Among the various stabilization methods, the MSB, fly ash, and cement-stabilized sections yielded significantly higher stiffnesses immediately after construction. However, considering that laboratory mix design tests and specialized construction equipment are usually required to ensure the final performance of the chemical stabilizations, use of MSB layers may be more cost-effective for practioners to implement.

The average as-constructed stiffness of the MSB layers without the NW-geotextile ranged between 476 and 505 MPa (Figure 3.4(b)), and the Iowa DOT-specified clean macadam material was not statistically different from the dirty and RPCC macadam, which were considered marginal materials. For the MSB sections with an embedded NW-geotextile layer, the average as-constructed stiffnesses were 14% to 25% lower than the sections without the geotextile. However, some long-term benefits of the geotextile layer such as reducing surface rutting, preventing material migration, and facilitating drainage may not be reflected by the as-constructed FWD test results. For the durability of the MSB sections, the dirty macadam sections showed the greatest stiffness reduction (approximately 26%) one year post-construction, while

the average elastic modulus of the RPCC macadam layer increased about 25% due to the beneficial effects of further hydration of the RPCC material.

Compared to the control sections, the test sections designed for improving subsurface drainage conditions (the aggregate column and geocomposite sections) did not have significantly increased as-constructed stiffnesses. However, their performance in mitigating drainage related or freeze-thaw related damage, and their influence on the stiffness of the roadway systems during thawing periods have not been evaluated. These topics are beyond the scope of the present study and will be presented in a future publication due to length restrictions.

3.10. Acknowledgements

CHAPTER 4. MECHANISTIC-BASED COMPARISONS FOR FREEZE-THAW PERFORMANCE OF STABILIZED UNPAVED ROADS

A paper to be submitted to *Cold Regions Science and Technology*

Cheng Li, Pavana K.R. Vennapusa, Jeramy C. Ashlock, and David J. White

4.1. Abstract

Unpaved roads in seasonally frozen regions are frequently subjected to frost boils and other freeze-thaw related damage. In this study, a range of several promising stabilization technologies selected based on a comprehensive literature review were evaluated for their ability to improve the freeze-thaw performance of unpaved roads under the same set of geological, climate, and traffic conditions. A total of 17 test sections were constructed using nine geomaterials, three chemical stabilizers, and three types of geosynthetics over a 3.2 km stretch of unpaved road. Visual inspections and extensive dynamic cone penetrometer (DCP) and falling weight deflectometer (FWD) tests were conducted over two seasonal freeze-thaw periods to compare the surface performance and mechanical properties of the various test sections. A weather station and subgrade temperature sensors were installed to monitor the depth and duration of soil freezing, and to determine the critical thaw-weakening periods during which to conduct field tests. The test results revealed that sections with macadam stone base (MSB) layers yielded the best freeze-thaw performance in terms of elastic modulus among all the stabilization methods examined. Multiple regression analyses of measurements taken after thawing showed that the aggregate layer modulus had a statistically greater influence on the overall composite modulus of the MSB sections, but the modulus of the underlying weaker subgrade layer had a greater influence in the sections without MSB layers. The field test results also demonstrated that the

stiffness and strength of underlying subgrade layer in the MSB sections were improved due to the benefits offered by the MSB layers.

4.2. Introduction

Unpaved roads in seasonally frozen regions experience several types of freeze-thaw related damage including frost boils, rutting, and potholes. This damage is dependent upon a combination of factors including the presence of frost-susceptible soils, duration of subfreezing temperatures, number of freeze-thaw cycles, source of water, poor subsurface drainage, and heavy traffic loading (Henry and Holtz, 2001; Hoover et al., 1981; Kestler, 2003; Saarenketo and Aho, 2005; White and Vennapusa, 2013). The most unfavorable scenario usually occurs during the spring-thaw periods when the melted ice lenses and infiltrated water trapped above the zone of frozen subgrade can cause the saturated surface and subgrade materials to lose strength and stiffness under heavy traffic loads (Andersland and Ladanyi, 2004). Many counties in the northern U.S. provide traffic restrictions during spring thawing periods to reduce such damage. Some approaches currently used by County Engineers to repair the damaged areas include temporarily spreading rock on the affected areas, lowering or improving drainage ditches, bridging the areas with stone and geosynthetics covered by a top course of aggregate or gravel, coring boreholes and filling them with calcium chloride to melt lenses and provide drainage, and re-grading the crown to a slope of 4 to 6% to maximize spring drainage (White and Vennapusa, 2013). However, all these maintenance solutions aim to repair damage after it occurs, rather than to prevent or minimize its occurrence in the first place.

White and Vennapusa (2013) reviewed more than 150 publications to assess technologies for preventing or mitigating the freeze-thaw damage of low-volume roads. One of the conclusions from their review was that technologies that provide stable support conditions year-round with

improved subsurface drainage can significantly improve the freeze-thaw performance of low-volume road systems. However, due to the different climate, traffic, and subgrade conditions of the separate studies, it was difficult to compare the relative effectiveness of the various technologies.

In the present study, a total of 17 demonstration test sections were designed and constructed using nine geomaterials, three chemical stabilizers, and three types of geosynthetics over a 3.2 km stretch of unpaved road in Hamilton County, Iowa, USA. A weather station and a vertical array of subsurface thermocouples were installed to monitor the weather and subsurface temperatures to determine the critical thaw weakening periods in which to conduct field tests. This paper presents the results of visual inspections, falling weight deflectometer (FWD) tests, and dynamic cone penetrometer (DCP) tests conducted over two seasonal freeze-thaw cycles (both pre-freezing and post-thawing). Statistical analyses of the test data are also conducted to compare the relative performance of the test sections and assess the influence of the surface aggregate layers and subgrade on the composite stiffness for both pre-freezing and post-thawing conditions.

4.3. Background of the Selected Technologies

Pertinent background information and findings from previous studies related to the selected technologies are summarized in the following sections.

4.3.1. Macadam stone base layers

Macadam stone base (MSB) layers with large maximum aggregate particle sizes of 75 or 100 mm have been evaluated in several research projects (e.g., Hoover et al., 1981; Jobgen et al., 1994; Less and Paulson, 1977; Lynam and Jones, 1979). The presence of large voids and improved particle interlocking between the large aggregates were believed to help minimize

56

freeze-thaw related damage. Visual inspections from 1988 to 1992 showed that MSB layers exhibited the best overall performance and durability compared to asphalt- or biochemical-treated base layers (Jobgen et al., 1994). Less and Paulson (1977) reported that a 200 mm thick MSB layer was the most cost-effective design in Iowa. It was noted in those studies that construction of the MSB layers was relatively simple and fast, but the MSB layers needed to be constructed on either a prepared subgrade or an existing unpaved road surface to prevent subgrade intrusions. However, most of the reported findings in the previous studies were qualitative, and very little quantitative information is available to date in terms of improvement in the mechanistic properties when using MSB layers.

4.3.2. Chemical stabilizations

White and Vennapusa (2013) provided a review of over 70 technical articles that summarized various chemical stabilizers in the contexts of freeze-thaw durability and guidelines for design and construction. They studied differences in the mechanisms and performance of active and passive chemical stabilizers. Commonly used active chemical admixtures include Portland cement, fly ash, lime, and bentonite, whereas passive chemical admixtures include bitumen, plant processed bio-fuel co-products with varying lignin contents and lignosulfates, and polymer emulsions. In the present study, Portland cement, ASTM Class C self-cementing fly ash (ASTM, 2012), and bentonite were used in the demonstration sections, and their relative performance will be presented herein.

Stabilization by Portland cement and ASTM class C self-cementing fly ash can improve the shear strength, stiffness, and wet-dry and freeze-thaw durability of soils (e.g., Cetin et al., 2010; Johnson, 2012; Parsons and Milburn, 2003; Shoop et al., 2003; Solanki et al., 2013; White et al., 2005a; White et al., 2005b; Zhang et al., 2016). Guidance on selection of chemical stabilizers

based on soil classification and plasticity properties is provided by Chu et al. (1955) and Terrel et al. (1979). The use of self-cementing fly ash for soil stabilization provides environmental benefits in terms of recycling a waste product, and cost savings relative to other chemical stabilizers. However, the physical properties of fly ash vary significantly between plants, which therefore warrants a detailed laboratory mix design and evaluation to ensure that soil stabilization is effective (White et al., 2005a; White et al., 2005b).

The freeze-thaw durability of chemically stabilized materials has been extensively studied in laboratory settings, typically by measuring material loss during freeze thaw cycles and/or unconfined compressive strength/California bearing ratio (CBR) tests following a certain number of freeze thaw cycles. In such studies, Portland cement stabilized materials generally exhibit superior performance relative to other chemical stabilizers (e.g., Henry et al., 2005; Parsons and Milburn, 2003); while observations related to performance of fly ash-stabilized soils are mixed. For instance, Bin-Shafique et al. (2010) reported that fly ash stabilized soils lost up to 40% of their strength due to freeze-thaw cycles, but did not experience significant strength loss during wet-dry cycles. Berg (1998) studied the laboratory freeze-thaw performance of reclaimed hydrated fly ash-activated aggregate materials, and found that they did not survive beyond ten freeze-thaw cycles. However, other studies documented that these materials did perform well, even though they break down under freeze-thaw action (e.g., Li et al., 2008; Parsons and Milburn, 2003; White et al., 2005b). Khoury and Zaman (2007) investigated the effect of freeze-thaw cycles on aggregates stabilized with cement kiln dust (CKD), class C fly ash, and fluidized bed ash (FBA). Their results indicated that the resilient moduli of the various mixtures decreased with increasing freeze-thaw cycles. Comparisons with control specimens were not provided in

their study, but it was reported that CKD-stabilized base materials deteriorated faster than fly ash- and FBA-stabilized base materials.

Bergeson and Wahbeh (1990) and Bergeson et al. (1995) documented the use of bentonite (sodium montmorillonite clay) surface treatments as a means for dust reduction of gravel roads in comparison with calcium and magnesium chloride. They noted that the negatively charged surfaces of montmorillonite particles interact with positively charged limestone fines, forming an "electrochemical glue" that can effectively reduce dust and improve the slaking characteristics and stability of limestone-surfaced roads. Bergeson et al. (1995) concluded that calcium chloride treatments are 2 to 3 times more effective than bentonite in the short term, but bentonite is more cost-effective because its bonding capability can last much longer (2–3 winter seasons) than chloride treatments (3–4 months).

4.3.3. Geosynthetics

Geotextiles and geogrids have previously been evaluated for mechanically improving the freeze-thaw performance of unpaved roads (e.g., Henry, 1990; Henry, 1996; Hoover et al., 1981; Lai et al., 2012). The geosynthetics are usually placed between the subgrade and base layers to provide separation, reinforcement, and subsurface drainage. Hoover et al. (1981) conducted laboratory freeze-thaw tests and concluded that specimens with an embedded geotextile disc showed lower frost-heave rates and greater cohesion and friction angle values, but decreased stiffnesses relative to control specimens. Based on field experiments, Henry (1990) reported that geotextiles used as capillary barriers can reduce the occurrence of frost heaves by approximately 60%. Henry (1996) also indicated that the performance of geotextiles in reducing frost heave rates depends on the geotextile's pore size distribution, wettability, and thickness.

Geocomposite materials consist of two geotextile layers and a drainage net, and are typically used as capillary barriers to prevent surface materials from becoming saturated (Christopher et al., 2000; Holtz et al., 2008). Henry et al. (2005) conducted a field investigation and showed that a geocomposite drainage layer can keep upper layers of unpaved roads relatively dry, and accelerate strength recovery of the systems. Christopher et al.(2000) studied locations for installing geocomposite drainage layers and concluded that layers placed on or within the subgrade were quickest at removing water during spring thawing. Henry and Holtz (2001) also found significant reductions in frost heave when the overlying soil had a degree of saturation below 75%, but the geocomposite could not prevent heave when the degree of saturation exceeded 80%, due to water migrating through a film adhered to the middle geonet layer.

4.4.   Site Descriptions and Materials

In this study, a 3.2 km stretch of heavily used farm-to-market unpaved roadway in Hamilton County, Iowa was selected for constructing the test sections. The nominal width of the road was 8.5 m. According to the Iowa DOT (2011), the annual average daily traffic (AADT) of the roadway was 130 vehicles. The county officials reported that the selected road routinely experienced significant freeze-thaw related damage in the past. Laboratory particle-size analysis test results showed that the subgrade contained 24% silt and 35% clay (particle size < 0.02 mm) and had a plasticity index (PI) of 21. Per the USACE (1984) chart, the frost susceptibility of the subgrade materials ranged from medium to very high. The Natural Resources Conservation Service (NRCS) web soil survey database rated the natural subgrade material as very frost-susceptible (NRCS, 2016).

Three chemical stabilizers (i.e., fly ash, cement, and bentonite), three types of geosynthetics (i.e., geocomposite, NW-geotextile, and BX-geogrid), and geomaterials were used to construct

various test sections (Figure 4.1) over the selected roadway. Five existing sections located at different locations within the 3.2 km road were used as control sections without any modification. The particle size distribution curves of all geomaterials used in this study and their Unified Soil Classification System (USCS) symbols determined in accordance with ASTM (2003) and ASTM (2011) are shown in Figure 4.2. According to the liquid limit (LL) and plastic limit (PL) test results (ASTM 2010), all materials are non-plastic except for the subgrade and subgrade-aggregate (SG+AGG) mixture.
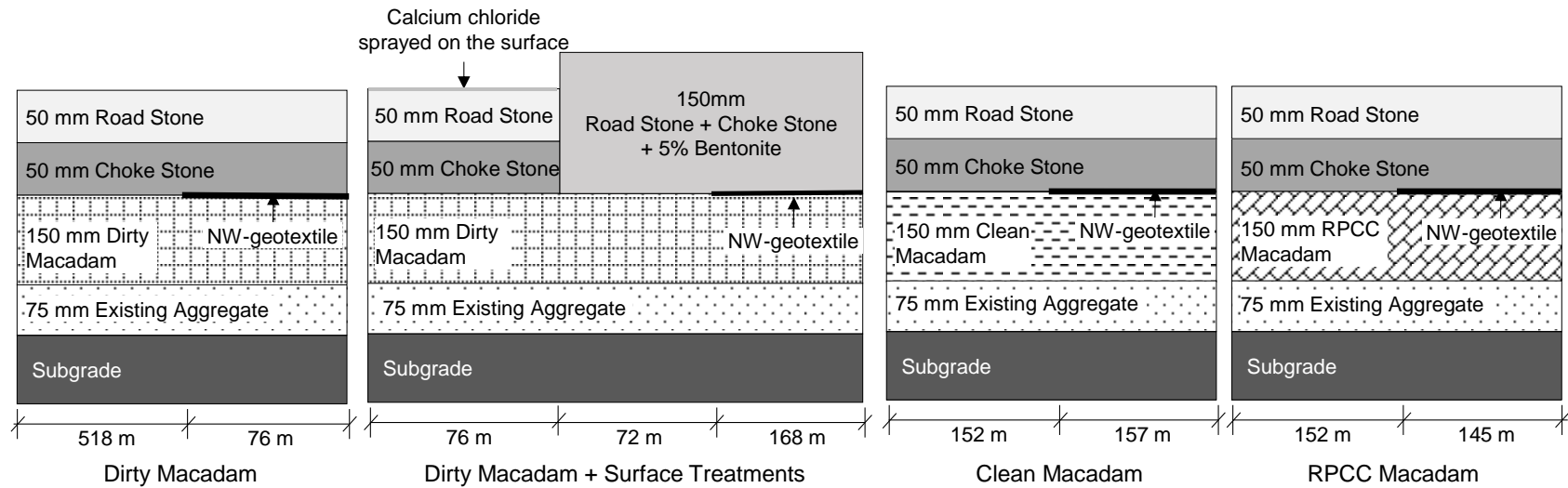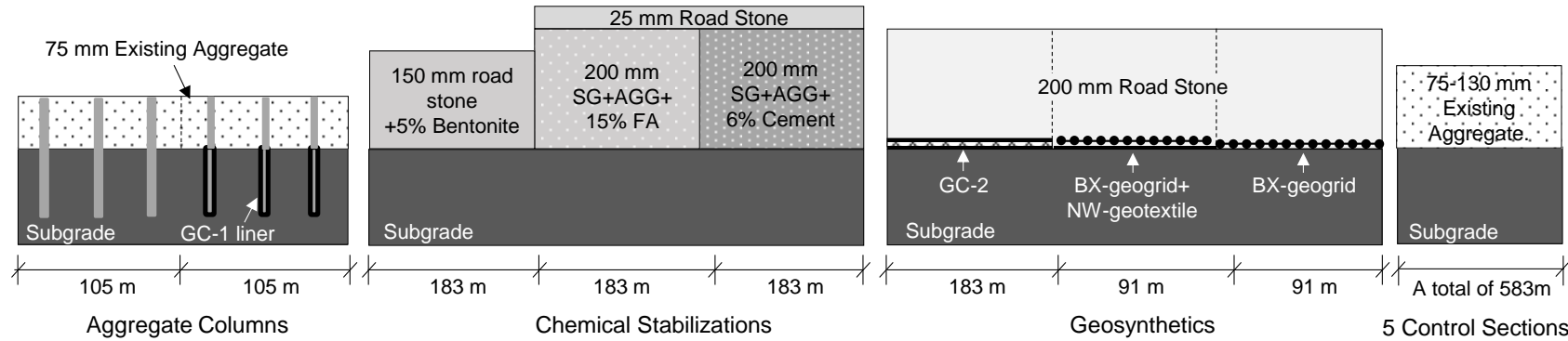
Figure 4.1. Nominal cross-section profiles, names, and lengths of the test sections (not to scale)
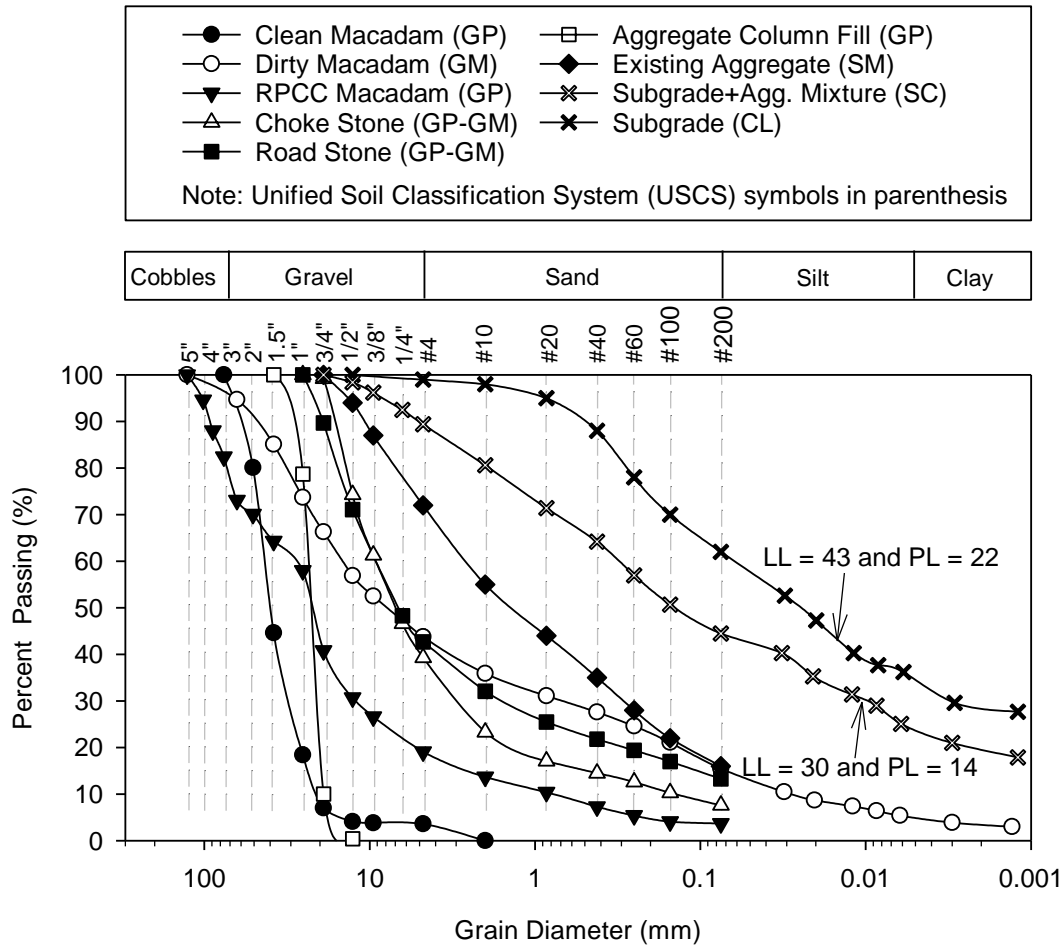
Figure 4.2. Particle size distribution curves and USCS soil classifications of the nine geomaterials used in this study.

Nine sections with macadam stone base (MSB) layers were constructed over the first 1.6 km of roadway using three different macadam types (i.e., dirty, clean, and recycled Portland cement concrete (RPCC)). The clean and dirty macadam consisted of virgin aggregates. The clean macadam was uniformly graded with 100% retained on the No. 10 sieve, while the dirty macadam was well graded with 15% passing the No. 200 sieve (Figure 4.2). The RPCC macadam consisted of recycled concrete material, and was well graded with 3.7% passing the No. 200 sieve. The cross-section designs and construction procedures for the various MSB sections essentially followed the recommendations of the previous studies discussed in Section 4.3.1. Nonwoven (NW) geotextile was used in some sections to prevent contamination of the

MSB layers by fines, and to compare the performance to sections without geotextile. Calcium chloride or bentonite was used to treat surfaces of three of the dirty macadam sections for dust reduction. The calcium chloride was sprayed on the roadway surface with an unknown concentration by a property owner, whereas the bentonite was mixed with the surface aggregates at a specific concentration as part of the research project.

Two aggregate column sections were constructed over a portion of the second 1.6 km of roadway, near a tile crossing location where frost boils were often observed. The purpose of the aggregate columns was to facilitate drainage of the subgrade and minimize the damage due to effects of frost boils. The diameter of the columns was approximately 200 mm and the depth was 1.8 m, which is below the estimated local maximum frost depth of approximately 1.2 m (Bowles 1996). The diameter of the columns was selected based on the local County engineer's experience. To prevent contamination of the clean aggregate fill, the bottom 1.2 m of the aggregate columns were lined around the perimeter with a geocomposite layer (denoted GC-1 in Figure 4.1) in one of the two sections.

For the three geosynthetic-stabilized sections shown in Figure 4.1, a geocomposite layer (GC-2), NW-geotextile with a BX-geogrid having a 25 by 33 mm rectangular aperture opening, or the BX-geogrid alone were installed at the subgrade to aggregate interface to provide drainage, separation, and reinforcement. To design the thickness of the surface aggregate layer of the geogrid-stabilized sections, a method developed by Giroud and Han (2004a; 2004b) was used. The method considers the strength of both subgrade and surface aggregate materials, traffic load and volume, distribution of vertical stress, geosynthetic stiffness, and interlock between the geogrid and aggregate material. The calculated thickness of the surface layer according to this

method was 217 mm. However, to compare the relative performance of the three geosynthetic sections, a consistent surface layer thickness of 200 mm was used.

The three chemically stabilized sections were constructed using 5% bentonite (sodium montmorillonite), 15% self-cementing fly ash, and 6% type I/II Portland cement by dry weight. The 5% bentonite was mixed with the top 125 mm of existing aggregate to reduce dust and improve stability of the surface layer. However, the cement and fly ash were mixed with a thinner 75 mm existing surface aggregate (AGG) layer and 125 mm of subgrade (SG) in order to compare with the geosynthetic-stabilized sections. According to a previous laboratory study on effects of stabilizer content on the freeze-thaw performance of a similar local subgrade (which contained 21.4% silt and 33.6% clay), a concentration of 15% fly ash yielded the optimal freeze-thaw performance, and cement concentrations of 5% and 10% showed negligible frost heaves and similar post-thawing CBR values (Zhang et al., 2016). Laboratory mix designs were also conducted in the present study for the fly ash- and cement-stabilized sections. Based on the mix design results, factors that can influence performance including compaction moisture content and compaction delay time were specified during construction.

4.5. Field Testing and Statistical Analysis Methods

Dynamic cone penetrometer (DCP) and falling weight deflectometer (FWD) tests were conducted to measure the pre-freezing and post-thawing shear strength and stiffness of all 22 test sections. DCP and FWD test results were statistically assessed using Dunnett's T3 test, Welch's t test, and multiple regression analysis.

4.5.1. Dynamic cone penetrometer tests

DCP tests were conducted to measure the shear resistance of different material layers of the test sections in accordance with ASTM D6951 (2009). An 8 kg hammer was dropped from a

fixed height of 575 mm to drive a conical tip to a maximum depth of 880 mm below the roadway surface. The penetration per blow was measured in millimeters, and is referred to as the dynamic cone penetration index (DCPI). The measured DCPI values were correlated to in situ California bearing ratio (*CBR*) values using the following empirical relations recommended in ASTM (2009):

for CBR > 10,

$$CBR = 292 / DCPI^{1.12} \qquad (4.1)$$

for CL soils with CBR < 10,

$$CBR = 1 / (0.017019 \times DCPI)^2 \qquad (4.2)$$

The DCP tests were also used to measure the thickness of the different material layers based on sudden changes in the depth profiles of cumulative blows and CBR values, as shown in Figure 4.3. However, the interfaces between the MSB layers and the aggregate layers could not be clearly identified because of their similar shear strengths. All of the test sections in this study were therefore analyzed as two-layered systems consisting of an aggregate layer over a subgrade layer. The weighted average CBR values for the surface aggregate layer and subgrade will be denoted CBR_{AGG} and CBR_{SG}, respectively.
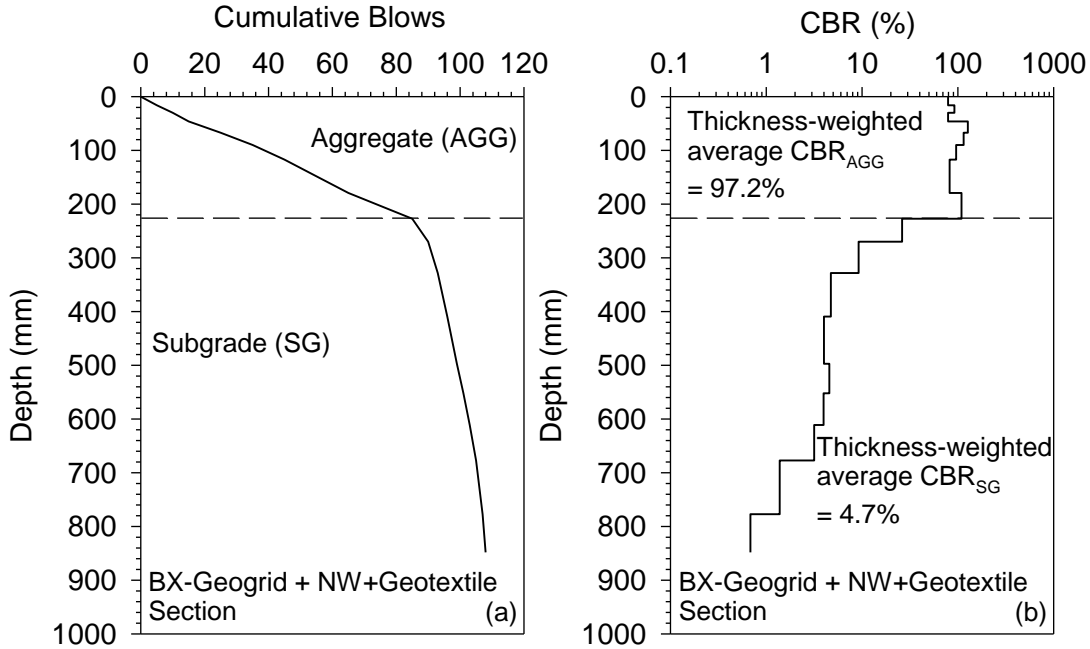
Figure 4.3. Example of DCP test results: (a) cumulative blows and (b) CBR versus depth profiles.

4.5.2. Falling weight deflectometer tests

Falling weight deflectometer tests were conducted to measure the elastic moduli of the test sections using a Kuab Model 150 FWD device with a 300-mm diameter segmented loading plate. For each test location, a seating load was applied followed by four loading drops with increasing dynamic contact forces between 27 and 71 kN. In this paper, the elastic moduli values calculated for a 566 kPa applied pressure (used by AASHTO, 1993) are presented. Eight seismometers were used to measure the roadway surface deflections at distances between 0 and 152 cm from the center of the loading plate. The peak deflection measured at the center of the loading plate was used to calculate a single equivalent composite elastic modulus ( ) based on Boussinesq's solution, by considering the different layers as a single composite system using the following equation:

$$E_{Composite} = \frac{\left(1 - \nu^2\right)\sigma_0 A}{d_0} \times f \tag{4.3}$$

where $E_{Composite}$ is the composite elastic modulus (MPa); d_0 is the measured deflection at the center of the loading plate (mm); ν is the Poisson's ratio (assumed to be 0.4); σ_0 is the normalized applied peak stress (MPa); A is the radius of the plate (mm); and f is the shape factor, assumed to be 2 for a uniform stress distribution (Vennapusa and White, 2009).

Additionally, layered elastic modulus values were calculated for all the test sections, treating them as two-layer systems. The elastic modulus of the aggregate layer (E_{AGG}) and subgrade (E_{SG}) were calculated using an approach developed based on Boussinesq's solution and Odemark's equivalent layer thickness assumption, which is detailed in AASHTO (1993).

4.5.3. Statistical analysis methods

Welch's unequal variances t test, also called the approximate t test, was used to determine statistical significance in the difference between two sample means. In this study, the approximate t test was used to compare the average *CBR* values of the subgrade under the MSB with those of the other sections. The approximate t value (t') was calculated using the following equation (Ott and Longnecker, 2001):

$$t' = \frac{\mu_1 - \mu_2}{\sqrt{\dfrac{S_1^2}{n_1} + \dfrac{S_2^2}{n_2}}} \tag{4.4}$$

where $\overline{\mu_1}$ and $\overline{\mu_2}$ are the average *CBR* values, S_1^2 and S_2^2 are the corresponding variances, and n_1 and n_2 are the number of tests for the two sections.

The degree of freedom calculated using Satterthwaite's approximation (Satterthwaite, 1946) can be used to determine the rejection criteria (critical t value) as

$$df = \frac{(n_1 - 1)(n_2 - 1)}{(1 - c)^2 (n_1 - 1) + c^2 (n_2 - 1)} \tag{4.5}$$

where

$$c = \frac{S_1^2 / n_1}{S_1^2 / n_1 + S_2^2 / n_2} \qquad (4.6)$$

The calculated t' is then compared to the critical $t_{\alpha/2}$ for a two-tailed test with 95%

confidence level ($\alpha = 0.1$). If t' is greater than $t_{\alpha/2}$, it can be concluded that there is a

statistically significant difference at the 95% confidence level between the two sample means.

However, to compare the statistical significance among multiple sample means, the pairwise

approximate t test cannot control the family-wise type I error inflation (Hochberg and Tamhane,

1987). In this study, Dunnett's T3 test, recommended for small sample sizes with unequal

sample sizes and variances, was used to compare the average elastic modulus values among the

various test sections (Dunnett, 1980; Hochberg and Tamhane, 1987). To compare a number k of

test sections, a total of $k \times (k-1)/2$ pairwise comparisons must be made. The average elastic

modulus values of two sections were declared significantly different if their absolute difference

was greater than the test statistic;

$$\left| \mu_i - \mu_j \right| \geq SMM_{\alpha, k^*, \upsilon} \sqrt{\frac{S_i^2}{n_i} + \frac{S_j^2}{n_i}} \qquad (4.7)$$

$$\upsilon = \frac{\left(S_i^2 / n_i + S_j^2 / n_i \right)^2}{S_i^4 / n_i^2 \upsilon_i + S_j^4 / n_j^2 \upsilon_j} \qquad (4.8)$$

where $SMM_{\alpha, k^*, \upsilon}$ is the critical value of the Studentized maximum modulus distribution (Stoline

and Ury, 1979), α is the significance level (i.e., 0.05, 0.1, and 0.2 for 95%, 90%, and 80%

confidence level), k^* is the total number of pairwise comparisons (i.e., $k \times (k-1)/2$),

n_i and $n_j =$ are the number of measurements for the two sections, S_i^2 and S_j^2 are the variances

of the measurements for the two sections, and υ_i and υ_j are degrees of freedom for the two

sections (e.g., $n_i - 1$).

The E_{AGG} and E_{SG} results obtained from layered analysis were also compared with the

$E_{Composite}$ values using the following multiple regression model:

$$E_{Composite} = b_0 + b_1\left(E_{AGG}\right) + b_2\left(E_{SG}\right) \tag{4.9}$$

where b_0 is the intercept and b_1 and b_2 are the unstandardized coefficients for E_{AGG} and E_{SG},

respectively. The purpose of this analysis was to assess the relative significance of the influence

of each layer (i.e., the surface aggregate and underlying subgrade) on the composite deflection

response measured at the surface.

The magnitudes of the E_{AGG} values were much higher than the E_{SG} values. Therefore,

standardized coefficients b'_1 and b'_2 were calculated using Equation (4.10).

$$b_1'\ or\ b_2' = b_1\ or\ b_2 \times \frac{SD_{E_{AGG}}\ or\ SD_{E_{SG}}}{SD_{E_{Composite}}} \tag{4.10}$$

where SD is the standard deviation of the elastic moduli values. Finally, the percentage of

influence of the surface aggregate and subgrade layers were evaluated using the following

equations:

$$\text{Influence of Surface Aggregate} = \frac{b_1'}{b_1' + b_2'} \times 100 \tag{4.11}$$

$$\text{Influence of Subgrade} = \frac{b_2'}{b_1' + b_2'} \times 100 \tag{4.12}$$

4.6. Monitoring of Weather and Subgrade Temperatures

To monitor the weather conditions and ground temperatures at the project site, a weather station was installed, and six thermocouples were embedded at depths of 15, 30, 60, 90, 120, and 150 cm below the roadway surface by attaching the thermocouples to a PVC pipe embedded in a backfilled borehole. The PVC pipe was filled with expanding foam to minimize heat conduction between different depths, and the natural soil was compacted around the pipe after placing the thermocouples in contact with the borehole wall. Based on the temperature data, the maximum frost penetration depths and durations of the freezing and thawing periods over the two seasonal freeze-thaw periods were monitored. From the measured subgrade temperature profiles, the 0℃ isotherm lines determined as a function of depth and time are shown in Figure 4.4. For any date on the x-axis, the isotherms delineate the upper and lower extents of the frozen soil zone.
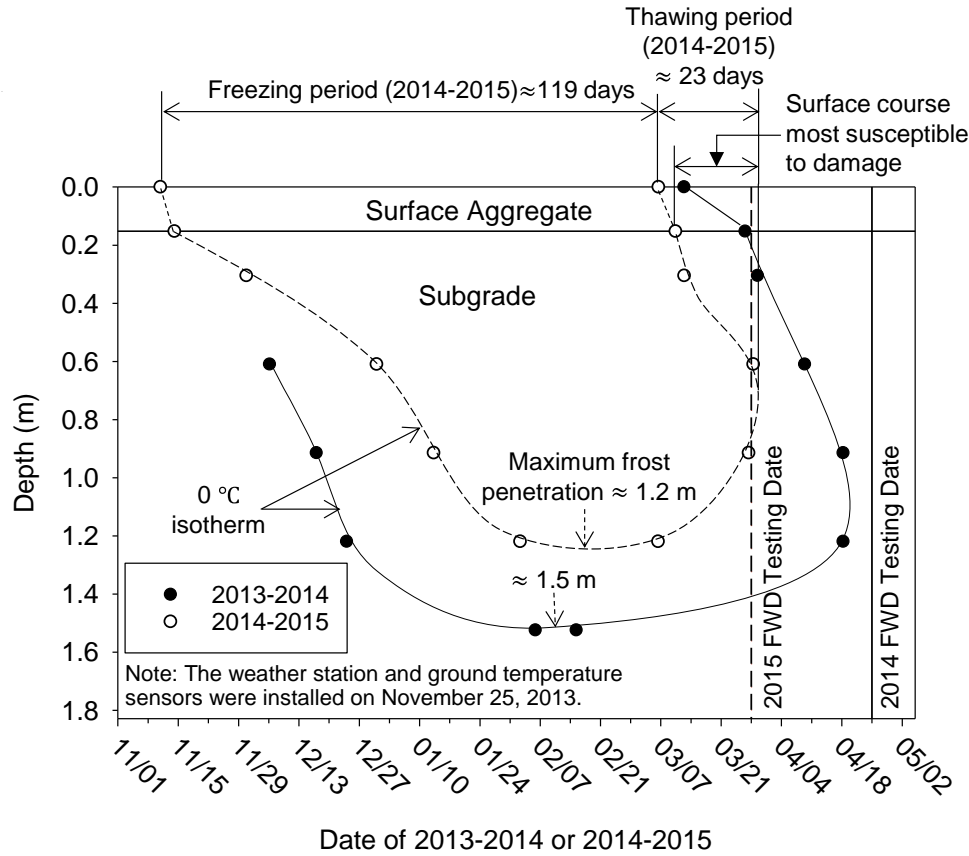
Figure 4.4. Isotherms showing subsurface freeze-thaw periods and maximum frost penetration depths of the project site over two winter-spring periods.

The lengths of the freezing periods were determined based on the first and last days for which the ground temperature remained below 0℃ at the ground surface. The upper 30 cm of the profile was already frozen when the ground temperature sensors were embedded in 2013, so the 0℃ isotherm contour in Figure 4.4 is not complete for 2013–2014. The maximum frost penetration depth during the winter of 2013–2014 progressed beyond 1.5 m, which was 0.3 m deeper than the 2014–2015 winter and the approximate local maximum frost depth of 1.2 m estimated per Bowles (1996). The freezing and thawing periods of the first seasonal freeze-thaw cycle were also longer than those of the following year. The isotherms in Figure 4.4 quantify the durations over which the ground thaws from the bottom up and top down for both periods. The roadway surface is most vulnerable during such thawing periods, because the water trapped in

the thawed surface layer cannot drain through the frozen subgrade zone below, and it generates

high pore-water pressures under traffic loads (Andersland and Ladanyi 2004). In addition,

melting of the ice lenses could result in rearrangements of the soil structure, and volume changes

to adapt new equilibrium void ratios. In this study, the two groups of post-thawing tests were

conducted near the end of the thawing periods, as indicated in Figure 4.4.

4.7.   Comparisons of In Situ Stiffnesses of the Test Sections

Construction of the first 1.6 km of test sections was completed in fall 2013, while the second

1.6 km of test sections were completed in fall 2014. The first pair of pre-freezing and post-

thawing (2013–2014) FWD tests were therefore only conducted on the MSB sections of the first

1.6 km, and the second pair of tests (2014–2015) were conducted on all the test sections.

4.7.1. Test results on macadam stone base sections for 2013-2014

To quantify changes in the elastic moduli of the MSB sections, the pre-freezing and post-

thawing FWD tests were conducted at the same locations within each section, as shown in Figure

4.5. The test points were matched using the distance measuring device on the FWD referenced to

the start and end stations of the test sections. The FWD test results exhibited very similar trends

between the two periods, which indicates that the test point locations were well matched.

The average composite modulus values ($E_{Composite}$) of the MSB sections were more than 2.5

times higher than the control section for both pre-freezing and posting-thawing conditions. The

sections with higher pre-freezing stiffness also yielded higher post-thawing stiffness, as shown in

Figure 4.5(a). Among the MSB sections, the clean macadam section exhibited the highest $E_{Composite}$

values on average, but also yielded higher variability. Kazmee et al. (2016) explained that the large

voids between the uniformly graded large macadam aggregates can allow significant particle

movements and reorientations under heavy traffic loading, which could explain the observed

variability. Results presented in Figure 4.5(a) and (b) also reveal that the dirty macadam sections suffered greater modulus reductions after thawing than the clean and RPCC macadam sections, and that sections with the NW-geotextile layer yielded lower modulus values than the corresponding sections without the NW-geotextile. However, except for the clean macadam section, the sections with NW-geotextile also yielded smaller reductions in the E_{AGG} values. This implies that the NW-geotextile can improve the subsurface drainage for the macadam materials that have relatively higher fines contents, but not for the clean macadam which already has a lower fines content and large voids in the aggregate matrix.

Compared to the $E_{Composite}$ and E_{AGG} values, the subgrade elastic modulus (E_{SG}) values show much less variations in magnitude (Figure 4.5(c)). Additionally, the average E_{SG} values in the MSB sections are approximately twice those of the control section. This better subgrade support in the MSB sections is attributed to the effects of improved subsurface drainage through the large voids of the macadam layers, and increased confining stresses from the surcharge of the large macadam stones. The DCP tests were conducted to directly measure the shear resistance of the subgrade, and the test results agreed with the FWD test results, as will be discussed in the following
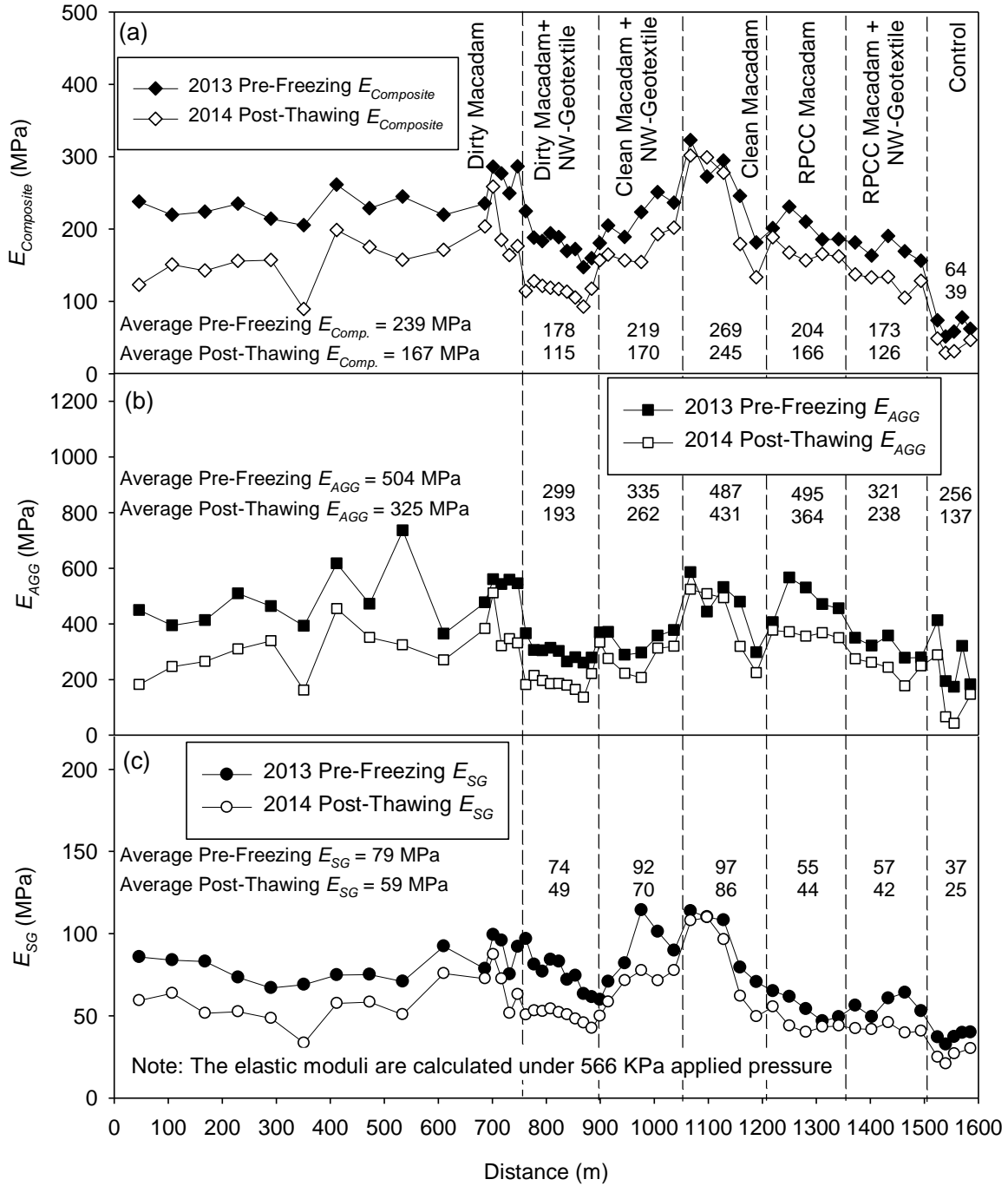
Figure 4.5. 2013 pre-freezing and 2014 post-thawing FWD test results for the MSB sections and one control section.

4.7.2. Test results on all sections for 2014-2015

The second pair of tests were conducted on all test sections in October 2014 (pre-freezing) and March 2015 (post-thawing). The test results are summarized together with the first pair of

FWD test results in the box plots of Figure 4.6, by which the medians, variations, and changes of the elastic moduli of the various test sections can be compared.

Overall, the MSB and fly ash- and cement-treated sections yielded higher $E_{Composite}$ values than other sections as shown in Figure 4.6(a). However, the cement and fly ash stabilized sections experienced significant modulus reductions after their first seasonal freeze-thaw cycle. The geogrid-stabilized sections also showed significant reductions in modulus after thawing, but remained stiffer than the control sections. The sections with the bentonite treatment yielded slightly higher $E_{Composite}$ values and less significant modulus reductions than the corresponding sections without bentonite. The $E_{Composite}$ values of the geocomposite and aggregate column sections, which were designed to improve subsurface drainage rather than strength or stiffness, were approximately the same as those of the control sections for both pre-freezing and post-thawing tests. Based on visual observations, the surfaces of the aggregate column sections performed much better than the control section during thawing (survey photos can be found in Li et al. 2015).

For the elastic modulus of surface aggregate layer, the chemically and geogrid-stabilized sections yielded much higher pre-freezing E_{AGG} values than other sections, but these values reduced greatly after thawing (Figure 4.6(b)). Additionally, significant variability was observed for $E_{Composite}$ and E_{AGG} values in the cement-stabilized section due to nonuniform mixing of the cement with surface aggregate and subgrade materials because of a varying surface course thickness.

The subgrade modulus values of the MSB sections were also higher than the other sections for both pre-freezing and post-thawing conditions (Figure 4.6(c)). The post-thawing E_{SG} values of most test sections were lower than the pre-freezing E_{SG} values, except for the dirty macadam

with bentonite treatment, RPCC macadam, and fly ash- and cement-stabilized sections, which showed improvements in E_{SG} after thawing. This phenomenon is attributed to the relatively low hydraulic conductivity of the chemically stabilized surface materials and hydrophilic nature of the RPCC macadam, which likely impeded the melting snow from penetrating into the subgrade (Nokkaew et al., 2012; Rahardjo et al., 2011; White et al., 2008).

Varying degrees of modulus recovery over the summer 2014 season (between the 2014 post-thawing and pre-freezing tests) are also evident for the MSB sections constructed in 2013 as well as the control sections. The dirty macadam section yielded much less recovery in $E_{Composite}$ and E_{AGG} than the other MSB sections, while the sections with NW-geotextile showed greater recovery than the corresponding sections without the NW-geotextile, which also indicates that the NW-geotextile layer can bring long term benefits to unpaved road systems.
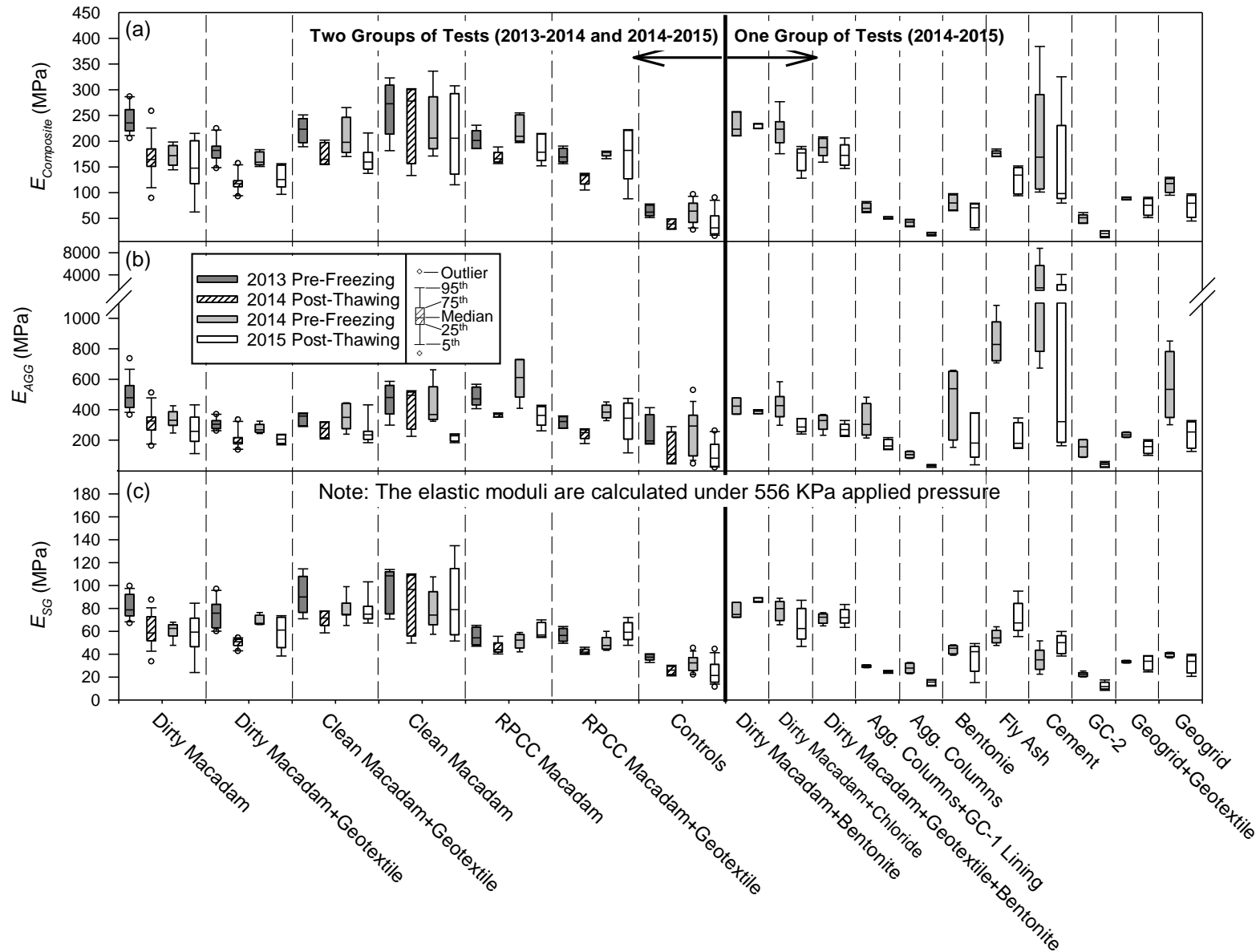
Figure 4.6. Moduli from pre-freezing and post-thawing FWD tests conducted on all sections.

4.8. Performance of Test Section Surfaces during Thawing

To assess and track the performance of the various stabilization methods through the critical seasonal thawing periods, survey photographs were taken of each test section. During the first (2014) thawing period, the MSB sections did not suffer any discernable damage, whereas the control sections suffered significant rutting, as shown in Figure 4.7 (a) through (g).

During the 2015 thawing period, the roadway surfaces of all test sections were generally in better condition than in the 2014 thawing period. This is likely a result of the shorter freezing and thawing periods and shallower frost penetration depth in 2014-2015 compared to those of 2013-2014 (see Figure 4.4). In addition, the weather station data showed that the cumulative precipitation of the 2015 thawing period was only 30.9 cm, compared to 32.7 cm in 2014.

Survey photos taken during the 2015 thawing period revealed that the bentonite-treated surface of the dirty macadam section was much drier and tighter than the corresponding section without the bentonite (see comparison in Figure 4.7(h)). Laboratory hydrometer and Atterberg limits tests conducted on the field-collected samples showed that the better performance is associated with a higher clay content of the bentonite-treated material. This phenomenon can be explained by the fact that the bentonite (sodium montmorillonite) particles have extremely large specific surface areas absorbing significantly more water than the granular material, so the bentonite-treated surface appeared much drier under the same moisture conditions.

Figure 4.7. Surface conditions of (a through g) the MSB and control sections during the first thawing period (photos taken March 11, 2014), and (h) dirty macadam sections with and without the bentonite surface treatment during the second thawing period (photo taken March 28, 2015).

4.9.   Statistical Analyses

4.9.1. Comparisons of post-thawing elastic moduli

To statistically compare the post-thawing elastic moduli of the various stabilization methods, eight test sections without surface treatments for dust control or geosynthetics for improving drainage were selected for the analysis. The pairwise multiple-comparison procedure for unequal sample sizes and variances (Dunnett's T3 test) was performed on the 2015 post-thawing FWD test results (Table 4.1). The table is organized into a decreasing order based on the average $E_{Composite}$ values, and the differences that are statistically different at the 85% to 95% confidence levels are highlighted.

The results show that although the clean macadam section yielded the highest average $E_{Composite}$, the difference with other MSB sections was not statistically significant at the 85 to 95% confidence level due to the small sample size and large variance. Similar results were found for the cement-stabilized section. All MSB sections showed significantly higher average $E_{Composite}$ values than the geogrid-stabilized, bentonite-treated, and control sections at the 80% confidence level. The RPCC macadam section also had a higher average $E_{Composite}$ than the fly ash section at the 80% confidence level. For the surface aggregate layer, only the three analyzed MSB sections showed statistically higher E_{AGG} values than the control section at the 95% confidence level. For the subgrade, the RPCC macadam, dirty macadam, and fly ash- and cement-stabilized sections exhibited significantly higher E_{SG} values than the geogrid and control sections.

Table 4.1. Summary of the Dunnett's t3 test results for comparing the 2015 post-thawing elastic moduli values of the selected test sections..

Pairwise Multiple Comparisons		$E_{Composite}$ (MPa)		E_{AGG} (MPa)		E_{SG} (MPa)	
		$\mu_i - \mu_j$ [a]	Sig.[b]	$\mu_i - \mu_j$ [a]	Sig.[b]	$\mu_i - \mu_j$ [a]	Sig.[b]
Clean macadam	RPCC macadam	213−186	1.000	218−360	0.082	85−60	0.864
	Dirty macadam	213−149	0.898	218−267	0.975	85−58	0.859
	Cement	213−147	0.993	218−1042	0.988	85−49	0.529
	Fly ash	213−125	0.561	218−221	1.000	85−72	1.000
	Geogrid	213−75	0.177	218−241	1.000	85−32	0.209
	Bentonite	213−58	0.119	218−222	1.000	85−37	0.292
	Control	213−39	0.085	218−107	0.002	85−24	0.136
RPCC macadam	Dirty macadam	186−149	0.873	360−267	0.722	60−58	1.000
	Cement	186−147	0.999	360−1042	0.998	60−49	0.477
	Fly ash	186−125	0.112	360−221	0.314	60−72	0.908
	Geogrid	186−75	0.005	360−241	0.605	60−32	0.024
	Bentonite	186−58	0.001	360−222	0.762	60−37	0.172
	Control	186−39	0.001	360−107	0.002	60−24	<0.001
Dirty macadam	Cement	149−147	1.000	267−1042	0.993	58−49	0.991
	Fly ash	149−125	0.997	267−221	1.000	58−72	0.953
	Geogrid	149−75	0.112	267−241	1.000	58−32	0.140
	Bentonite	149−58	0.028	267−222	1.000	58−37	0.515
	Control	149−39	0.007	267−107	0.047	58−24	0.021
Cement	Fly ash	147−125	1.000	1042−221	0.989	49−72	0.266
	Geogrid	147−75	0.897	1042−241	0.991	49−32	0.275
	Bentonite	147−58	0.743	1042−222	0.989	49−37	0.884
	Control	147−39	0.546	1042−107	0.969	49−24	0.014
Fly ash	Geogrid	125−75	0.242	221−241	1.000	72−32	0.029
	Bentonite	125−58	0.053	221−222	1.000	72−37	0.081
	Control	125−39	0.010	221−107	0.425	72−24	0.014
Geogrid	Bentonite	75−58	0.994	241−222	1.000	32−37	1.000
	Control	75−39	0.357	241−107	0.419	32−24	0.836
Bentonite	Control	58−39	0.906	222−107	0.860	37−34	0.669

[a] Difference in average elastic moduli values between two sections.
[b] Opened, dashed line enclosed, and solid line enclosed shaded significance values show that the mean differences are statistically significant at 80%, 90%, and 95% confidence level, respectively.

4.9.2. Relative influence of aggregate and subgrade layers on the composite stiffness

To assess the influence of the surface aggregate layers and subgrade on the composite elastic moduli of the test sections for both pre-freezing and post-thawing conditions, multiple regression analyses with standardized coefficients were performed on the FWD measurements at a 95%

confidence limit. All of the test sections were categorized into six groups as shown in Table 4.2. The analysis results show that before freezing, the surface aggregate layers had a greater influence (58 to 74%) on the composite modulus values in all test sections except for the geosynthetic sections. In the geosynthetic sections, the subgrade layer showed a higher influence (59%) than the surface aggregate layer (41%) in predicting the composite modulus value.

For post-thawing conditions, the influence of the subgrade greatly increased (58% to 79%) in the control, aggregate columns, chemically stabilized, and geosynthetics sections. This indicates that the post-thawing reduction in composite modulus in these test sections was influenced more by the modulus reduction in the subgrade than the surface aggregate layer. In the macadam sections, however, the relative influence of the aggregate layers remained relatively unchanged. This is attributed to the observed smaller reduction in the subgrade modulus values after thawing in these sections. One exception was the clean macadam section after the 2015 post-thawing season, for which the E_{AGG} value was not statistically significant in the multiple regression analysis, and therefore the relative influence could not be calculated.

Table 4.2. Summary of multiple regression (95% confidence limit) analysis results for assessing relative influence of surface aggregate layer modulus (E_{AGG}) and subgrade modulus (E_{SG}) on composite modulus ($E_{Composite}$) of test sections.

Parameters	Dirty Macadam		Clean Macadam		RPCC Macadam		Control and Agg. Columns	Bentonite, Fly Ash, and Cement	Geosynthetics
Testing Period [a]	1 [a]	2 [a]	1	2	1	2	2	2	2
Number of Tests	25	26	10	12	10	10	26	14	13
Pre-Freezing FWD Tests									
R^2 of Regression Model	0.94	0.97	0.98	1.00	0.98	0.99	0.89	0.79	0.97
Standardized Coefficient for E_{AGG}	0.76	0.77	0.71	0.73	0.93	0.96	0.70	0.84	0.44
Standardized Coefficient for E_{SG}	0.46	0.39	0.44	0.33	0.45	0.34	0.36	0.60	0.63
Influence of Aggregate Layer	62%	66%	62%	69%	67%	74%	66%	58%	41%
Influence of Subgrade	38%	34%	38%	31%	33%	26%	34%	42%	59%
Post-Thawing FWD Tests									
R^2 of Regression Model	1.00	0.99	1.00		1.00	1.00	0.97	0.86	0.99
Standardized Coefficient for E_{AGG}	0.73	0.59	0.71		0.82	0.78	0.43	0.45	0.21
Standardized Coefficient for E_{SG}	0.37	0.47	0.33	NA [b]	0.31	0.26	0.59	0.77	0.81
Influence of Aggregate Layer	66%	56%	68%		73%	75%	42%	37%	21%
Influence of Subgrade	34%	44%	32%		27%	25%	58%	63%	79%

[a] 1 represents the first (2013–2014) freezing-thawing period, and 2 represents the second (2014–2015) freezing-thawing period.

[b] The E_{AGG} is not a significant influence variable at 95% confidence limit.

4.9.3. Subgrade shear strength of the MSB sections

DCP tests were conducted to independently verify subgrade support conditions and cross-check the results obtained from FWD data analysis in terms of higher E_{SG} values in the MSB sections compared to the other sections. The DCP test data and Welch t test results are summarized in Figure 4.8. For both pre-freezing and post-thawing conditions, the average CBR values of the subgrade (CBR_{SG}) of the MSB sections are at least two times higher than other sections. Welch t test results also showed that the average CBR_{SG} of the MSB sections during the 2015 thawing period is not significantly different from the pre-freezing average CBR_{SG}. However, it can be seen that the average CBR_{SG} values of other test sections significantly decreased during both 2014 and 2015 thawing periods. These findings suggest that use of MSB sections can not only retain the aggregate layer stiffness during freeze-thaw cycles, but also retain the underlying subgrade layer stiffness due to improved drainage and increased confining stresses, which is the key to the overall support of the system under traffic loading.
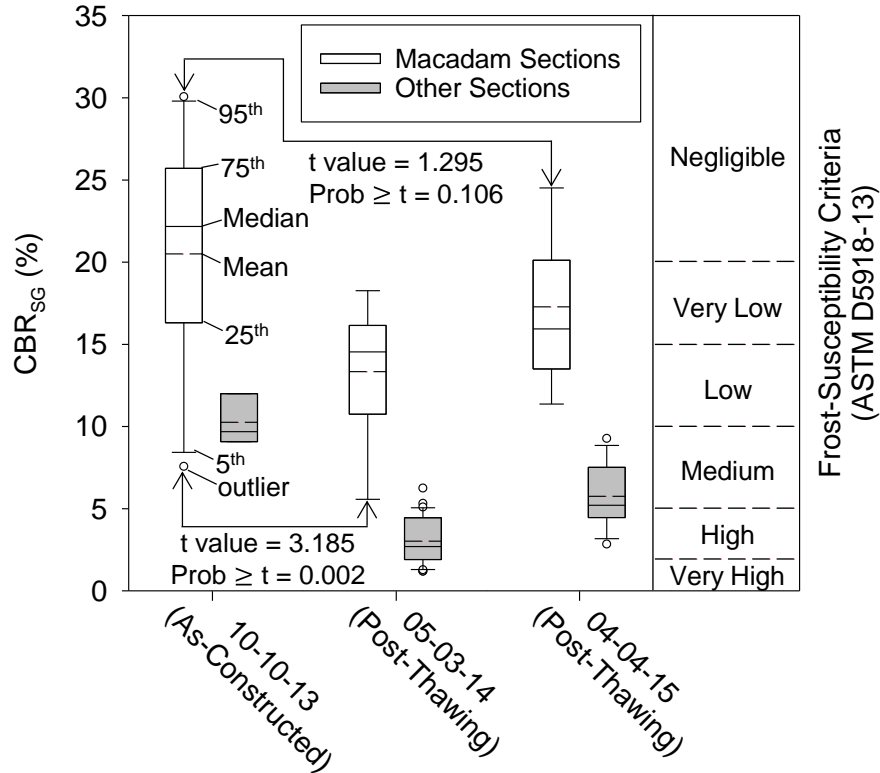
Figure 4.8. Comparisons of pre-freezing and post-thawing *CBR* values of the subgrade under the MSB and other sections.

4.10. Summary and Conclusions

In this study, a range of several promising technologies for mitigating freeze-thaw damage that were identified in a comprehensive literature review were used to construct a total of 17 test sections over a 3.2 km stretch of unpaved roadway in Iowa. This paper presented the visual survey and FWD and DCP test results conducted over two seasonal freeze-thaw cycles to compare the pre-freezing and post-thawing performance and mechanical properties of the various stabilization methods. Several key findings from the study are summarized below:

- The MSB, fly ash- and cement-treated, and geogrid-stabilized sections showed significantly higher composite modulus values than the other sections before freezing, but the chemically and geogrid stabilized sections suffered considerable modulus reductions after thawing.

- The clean macadam section had the highest pre-freezing and post-thawing elastic moduli compared to the other MSB sections, but exhibited greater variations possibly due to the large voids between the poorly graded particles resulting in more particle movements under the heavy FWD impact loads.

- The influence of the aggregate layers on the composite moduli of the MSB sections remained relatively unchanged from pre-freezing to post-thawing conditions, which indicates that the MSB layers play more significant structural roles than the subgrade. In contrast, the subgrade had a greater influence on the composite moduli of the non-MSB sections during thawing periods.

- The subgrade of the MSB sections showed significantly higher CBR values than the other sections for both pre-freezing and post-thawing conditions, which may be due to the increased confining stress and improved drainage offered by the MSB layers.

- The aggregate column sections did not have higher elastic moduli than the control sections, but visual inspections showed that they were very effective in preventing the occurrence of frost boils.

- The roadway surface with a bentonite treatment was much drier and tighter than the other sections during the thawing period, which indicates the importance of the plasticity of unpaved road surface materials.

4.11. Acknowledgements

CHAPTER 5. GYRATORY ABRASION WITH 2D IMAGE ANALYSIS TEST METHOD FOR EVALUATION OF MECHANICAL DEGRADATION AND CHANGES IN MORPHOLOGY AND SHEAR STRENGTH OF COMPACTED GRANULAR MATERIALS

A paper submitted to *Construction and Building Materials*

Cheng Li, Jeramy C. Ashlock, David J. White, Charles T. Jahren, and Bora Cetin

5.1. Abstract

Mechanical degradation of granular materials can significantly influence the performance and durability of pavement systems. The commonly used Los Angeles (LA) abrasion test does not test the entire gradation of the material, nor simulate the compaction and field loading conditions. A new Gyratory Abrasion and Image Analysis (GAIA) test method was developed in this study and compared with the LA abrasion test for five granular material types. Results show that the GAIA test can address shortcomings of the conventional test, provide insight into mechanical behavior of granular materials during compaction, and enable performance-based specifications for field compaction of granular materials.

5.2. Introduction

Mechanical degradation or abrasion of granular materials used for unpaved road surface and pavement base layers can significantly influence their mechanical properties, drainage conditions, and freeze-thaw durability (Cho et al. 2006; Nurmikolu 2005; Vallejo et al. 2006; White and Vennapusa 2014). As detailed in several previous studies, the degradation and abrasion of a granular material is a function of its mineral composition, gradation, morphology, and loading conditions including compaction during construction and traffic loading over the service life of a roadway (Hardin 1985; Lade et al. 1996; Lees and Kennedy 1975; Marsal 1967;

Nurmikolu 2005; White et al. 2004; Zeghal 2009). Previous studies have illustrated the effects of gradation and loading conditions on the degradation of aggregate, railroad ballast, and soils using static or cyclic triaxial tests (Chen and Zhang 2016; Hardin 1985; Indraratna et al. 2005; Nurmikolu 2005). To more practically evaluate degradation characteristics or create specifications for granular materials, most researchers and transportation agencies rely on the Los Angeles (LA) abrasion and Micro-Deval tests, which require specimens to be prepared to standard gradings and tested in a rotating steel drum containing steel spheres (ASTM 2014; ASTM 2014; Gökalp et al. 2016). However, these two testing methods do not simulate the actual loading conditions responsible for the degradation and performance of the materials, and do not test their full gradations.

To address these deficiencies, a new laboratory testing method is proposed and developed herein, which employs the gyratory compaction device and two-dimensional (2D) image analyses to evaluate the mechanical degradation and changes in morphology and shear strength of granular materials under simulated field compaction loads. The new method, termed the Gyratory Abrasion and Image Analysis (GAIA) method, aims to more accurately predict the actual degradation of granular materials after compaction, and rapidly establish the density-strength-compaction energy relationship for a material. The latter can be used to develop performance-based specifications that ensure field performance, minimize material degradation, and save time and energy. This paper details the new testing method and associated analyses, compares the results with those of conventional LA abrasion tests using five types of granular materials, explains the behavior of the granular materials during the gyratory compaction tests, and demonstrates how the test results can be used to develop performance-based specifications for field compaction of granular materials.

5.3. Background

The following sections provide background information on the mechanical degradation of granular materials as well as details on the gyratory compaction and image analysis techniques used for quantifying particle morphology in this study.

5.3.1. Gradation and loading effects on mechanical degradation

Mechanical degradation of granular materials can significantly decrease resilient modulus by up to 50% and increase permanent deformations by 100% to 300%, resulting in significant rutting and cracking on roadway surfaces (Zeghal 2009). It is widely known that uniformly graded or gap-graded aggregates can experience significantly more degradation than well-graded aggregates, because the lower void ratio of well-graded materials results in lower interparticle contact stresses. As a result, well-graded materials tend to break down more slowly than uniformly graded materials under a given set of loading conditions (Airey et al. 2008; Lade et al. 1996; Nurmikolu 2005). For example, the effects of maximum particle size and coefficient of uniformity (C_u) on the permanent deformation and degradation of railroad ballast were examined using large-scale cyclic triaxial tests, and it was reported that particle breakage was significantly reduced when C_u was larger than 1.8 (Indraratna et al. 2016). Particle breakage is also significantly influenced by load duration, with reported values of breakage index under creep loading being more than 1.5 times those of monotonic loading (Chen and Zhang 2016). Based on results of cyclic triaxial tests, degradation can also be minimized by keeping the confining pressure within a certain range (Lackenby et al. 2007).

5.3.2. Gyratory compaction device and pressure distribution analyzer

The gyratory compaction test was originally developed for mix design and field management of hot-mix asphalt (HMA) mixtures (Harman et al. 2002). In this test, two compaction

mechanisms: a constant vertical pressure and gyratory shear stresses induced by eccentric loadings are used to simulate field compaction and traffic loads (Bahia and Faheem 2007; Delrio-Prat et al. 2011). Previous studies have demonstrated that the gyratory compactor is also useful for evaluating the compaction characteristics of soils ranging from coarse aggregates to high-plasticity clays (Cerni and Camilli 2011; Li et al. 2015; Ping et al. 2002). The effects of the four equipment operational parameters, which are the vertically applied pressure and the angle, frequency, and number of gyrations, have been well studied for both HMA and soils (Butcher 1998; Mokwa and Cuelho 2008). Compared to other laboratory compaction methods such as impact and vibratory compaction, it has been reported that the gyratory compaction curves for soils can better replicate field compaction results (Ping et al. 2003).

A pressure distribution analyzer (PDA) was also developed in a prior study to monitor changes in shear resistance of HMA specimens during gyratory compaction (Guler et al. 2000). The PDA uses three load cells to measure the applied vertical load and changes in eccentricity of the load during the test. Based on the PDA data and equipment operational parameters, the theoretical compaction energy applied to the specimen can also be calculated (Delrio-Prat et al. 2011). Using the PDA to measure shear resistance of a granular material (Ottawa sand) was very repeatable (< 7 kPa), and a strong linear correlation ($R^2 = 0.89$) was found between the PDA-measured shear resistance and unconfined compressive strength for a fine-grained granular material possessing some apparent cohesion (Li et al. 2015).

5.3.3. Particle morphology and image analysis techniques

Aggregate morphology has long been recognized as an important factor affecting the engineering properties and degradation of granular materials (Cheung and Dawson 2002; Cho et al. 2006; Pan et al. 2006). Various parameters proposed to quantify the external morphology of

particles can be categorized in a three-tiered hierarchy of observational scales with respect to particle size: form, angularity, and surface texture (Barrett 1980; Özen 2007). The Rittenhouse and Krumbein charts were conventionally used to visually classify the sphericity and roundness of particles, respectively (Krumbein 1941; Rittenhouse 1943). As development of imaging and computing techniques advanced, image-based particle morphological analysis has enabled more rapid, objective, and repeatable means of classification (Al-Rousan et al. 2007). High-definition cameras and scanners have been used to collect 2D image data of aggregates. Automated 3D image analysis systems including the University of Illinois Aggregate Image Analyzer (UI-AIA) and the Aggregate Imaging System (AIMS) were also developed for determining morphological parameters at multiple length scales (Fletcher et al. 2003; Liu et al. 2016; Rao et al. 2001). The accuracy and ability of several image analysis methods have also been assessed by comparing their results to the Rittenhouse and Krumbein charts (Al-Rousan et al. 2007).

5.4. Materials and Testing Procedures

In this study, the new GAIA method was used for tests on five types of granular materials typically used for unpaved roadway surface and pavement foundation layers. To compare the results with conventional laboratory testing methods, sieve analyses and LA abrasion tests were also conducted in accordance with ASTM C136 and C131, respectively (ASTM 2014; ASTM 2014).

5.4.1. Materials

The five different granular material types were collected from a granular-surfaced road as well as from two quarries having different geological diagenesis. The existing surface aggregate (ESA) had the lowest gravel content (>4.75 mm), because this material had already been abraded by traffic for some time. Compared to the concrete stone (CS) material which consisted of a

uniformly graded clean aggregate, the virgin surface aggregate (VSA), road rock (RR), and class

A stone (CAS) were all more well graded. The sieve analysis results and Unified Soil

Classification System (USCS) symbols for the five materials are summarized in Table 5.1.

Table 5.1 Properties of the five granular materials tested in this study.

Parameters	Existing Surface Aggregate	Virgin Surface Aggregate	Road Rock	Class A Stone	Concrete Stone
Abbreviation	ESA	VSA	RR	CAS	CS
Source	Granular road	Quarry 1	Quarry 1	Quarry 2	Quarry 2
Gravel content (%)	24.0	68.7	65.2	42.9	96.3
Sand content (%)	50.0	22.8	19.5	48.9	2.9
Fines content (%)	26.0	8.5	15.3	8.2	0.8
Maximum aggregate size (mm)	25.4	38.1	38.1	25.4	25.4
Coefficient of curvature, C_c	4.23	7.61	18.32	3.99	1.08
Coefficient of uniformity, C_u	213.67	57.45	970.27	31.39	2.25
Plastic limit (%)	15	25			
Liquid limit (%)	17	16	NP[a]	NP[a]	NP[a]
USCS symbol	SM	GP-GC	GM	SP-SM	GP

[a] NP = non-plastic

5.4.2. Sample preparation and testing procedures

The gyratory compactor was used to compact the specimens under a constant vertical

pressure, with the PDA on top of the specimens to measure changes in their shear resistance

throughout the tests, as shown in Figure 5.1. A high-speed optical scanner (Canon 9000F Mark

II, Figure 5.2(a)) with a dust and scratch removal image processing feature was used to capture

2D color images of the gravel-size portions (retained on the 4.75 mm sieve) of the aggregate

specimens before and after the gyratory compaction tests.
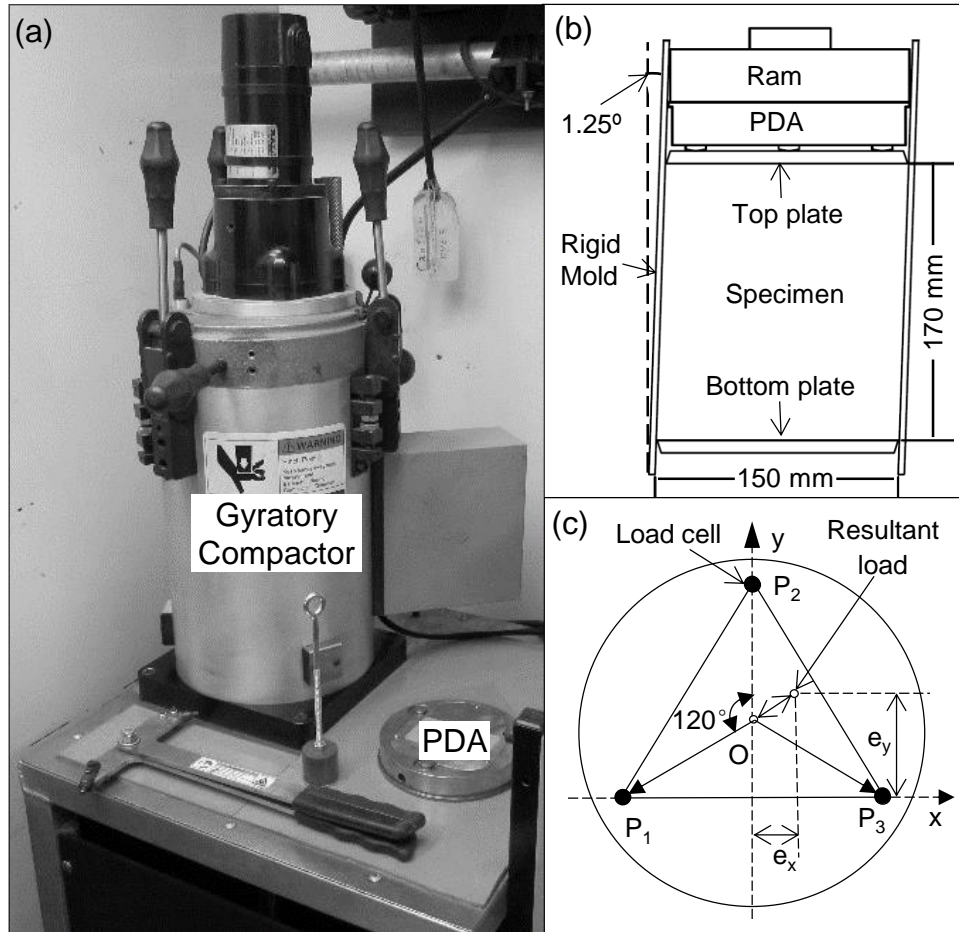
Figure 5.1. (a) Photo of gyratory compactor and Pressure Distribution Analyzer (PDA). (b) Schematic of the gyratory compactor. (c) Schematic of the PDA.

For each material type, a representative specimen of approximately 4500 g was prepared using a riffle splitter, then separated into two portions using a 4.75 mm (#4) sieve. The coarse portion was then washed, oven-dried at 110℃ for 24 hours, and scanned for image analysis. To determine the particle size (i.e., the equivalent sieve opening size) and 2D sphericity of each aggregate using the image analysis, the aggregate particles were manually distributed on top of the scanner platen with their maximum projection areas facing down. Depending on the gravel content, the number of coarse particles varied from 1,000 to 3,200 per specimen, with individual scans containing up to several hundred aggregate particles each. However, the scanning process was easy to perform and took less than two hours per specimen. After scanning, the coarse and

fine portions of the specimen were thoroughly mixed back together and transferred into the gyratory compactor.

In this study, the operational parameters of the gyratory equipment specified for testing asphalt mixtures in ASTM D6925 (ASTM 2014) were followed and summarized in Table 5.2. Effects of the operational parameters have also been evaluated in previous studies (see Section 5.3.2), and detailed discussion of all such parameters is beyond the scope of the present paper.

Table 5.2 Equipment operation parameters of the gyratory compactor.

Parameter	Value
Vertical applied pressure	600 ± 10 kPa
Number of gyrations	500 [a]
Angle of gyration	1.25 ± 0.02 degrees
Frequency of gyration	30 ± 0.5 gyrations/min
Number of dwell gyrations	2

[a] Applied in two consecutive tests having 250 gyrations each.

In this study, a total of 500 gyrations were applied to each specimen. Due to the compactor's limitation of a maximum of 299 gyrations per test, the device was temporarily stopped after 250 gyrations and then manually restarted. However, after the first 250 gyrations, the compactor automatically released the vertical pressure and applied two dwell gyrations to remove the angle of gyration and square the specimen. This procedure may have introduced some slight disturbance of the specimens and possibly resulted in varying degrees of dilation. After the gyratory compaction test, the washing, drying, and scanning procedures were repeated on the coarse fractions to analyze the changes in gradation and morphology caused by the gyratory compaction load during the test.

5.5. Data Analysis

The changes in volume of the specimens during the gyratory compaction tests were calculated from specimen heights measured using the system's integral displacement transducer.

Based on the dry mass and volume of the specimen, the dry unit weight (γ_d) can be easily

determined for each gyration, and the void ratio (*e*) can be calculated by assuming or measuring

the specific gravity (G_s) of the material as

$$e = \frac{G_s \gamma_w}{\gamma_d} - 1 \qquad (4.13)$$

where γ_w is the unit weight of water (9.81 kN/m³).

The shear resistance of the specimens can be determined for each gyration using the PDA

data. The three load cells embedded in the PDA give the resultant vertical load applied to the

specimen, as well as the eccentricity of the load relative to the center (*O*) of the PDA from

moment equilibrium equations along two perpendicular axes as shown in Figure 5.1(c). Based on

energy conservation principles, the energy of the external forces can be equated to the strain

energy of the specimen, assuming that energy due to surface traction is negligible (Guler et al.

2000). The effective moment can then be calculated for a direct measure of shear resistance of

the specimen as

$$\tau_G = \frac{R_i e_i}{A H_i} \qquad (4.14)$$

where *A* is the cross-sectional area of the compaction mold, H_i is the specimen height at a given

gyration number, R_i is the resultant vertical load applied on the specimen for the same gyration

number, and e_i is the eccentricity of the resultant load.

In addition, the PDA data can be used to estimate the compaction energy applied to the

specimen. The gyratory compaction energy ($E_{gyratory}$) is the work done per unit volume by the

vertical applied pressure and the moment induced by the vertical pressure and shear stress, which

can be calculated using the equipment operational parameters (Table 5.2) and the measured shear

resistance of the specimen as (see (Delrio-Prat et al. 2011; Li et al. 2015))

$$E_{gyratory} = \frac{PA\left(H_0 - H_N\right) + 4\theta\sum_0^N \tau_{G(i)}V_i}{V_i} \tag{4.15}$$

where $E_{gyratory}$ is the gyratory compaction energy (kJ/m^3), P is the vertical applied pressure

(kPa), A is the cross-sectional area of the mold (m^2), H_0 is the initial specimen height (m), H_N is

the height after the final gyration (m), θ is the angle of gyration (radians), V_i is the specimen

volume after gyration number i (m^3), and $\tau_{G(i)}$ is corresponding shear resistance of the specimen

(kPa).

As detailed above, the 2D image analyses were conducted on the gravel-size portions of each

specimen before and after each test, to quantify the abrasion and morphology changes caused by

the gyratory compaction. The images (0.085mm per pixel) were then processed using a public-

domain image-processing program named ImageJ developed by the National Institutes of Health,

to quantify the size and shape of the individual aggregates (Schneider et al. 2012). A series of

image processing techniques including noise reduction, contrast enhancement, thresholding,

background removal, local maxima detection, and hole filling were performed to convert the

original scanned color images to binary images, examples of which are shown in Figure 5.2(b)

and (c).
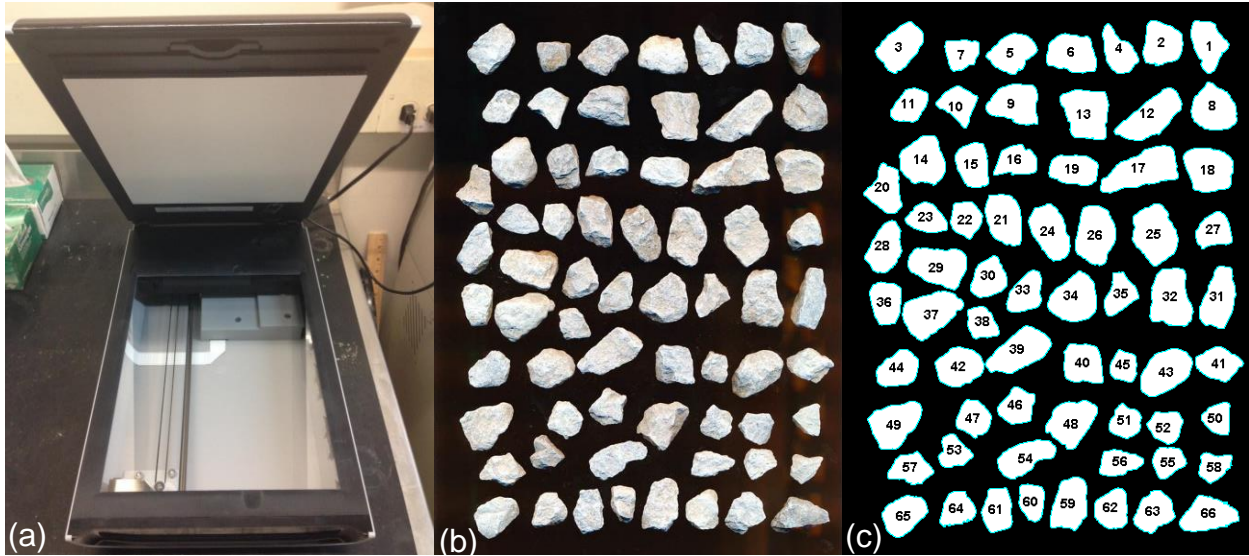
Figure 5.2. (a) Optical scanner used in this study. (b) Example original scanned color image of gravel-size aggregates. (c) Converted binary image with aggregate edges detected.

Using the 2D image analyses results, nearly continuous particle size distribution (PSD) curves of the gravel-size aggregates were generated. Several different methods could be used to estimate the particle sizes on the x-axis (i.e., the sieve size through which a particle would pass), including the minimum bounding rectangle, best-fit ellipse, or minimum Feret diameter, which is the minimum distance between two parallel lines tangential to the projections of an aggregate particle (Igathinathane et al. 2008; Yue et al. 1995). For the present study, the percentages finer than a given size on the y-axis were calculated using the ratio of each individual particle's area to the total area of all particles. This approach assumes that all particles have the same specific gravity, and that the ratios of their 2D projections are equal to the ratios of their volumes. The resulting PSD curves determined by the three methods mentioned above are compared in Figure 5.3. For all specimens tested in this study, similar comparisons revealed that the PSD curves determined by the minimum Feret diameter consistently showed the best agreement with actual sieve analysis results, with typically less than 6% difference at any given particle size. However, as particle size decreases, the difference between Feret diameter and sieve analysis can increase

to as much as 14%. The differences between PSDs from sieving versus 2D image analyses are mainly caused by the image analyses being based on area fractions rather than mass fractions (Ohm and Hryciw 2013; Tutumluer et al. 2000). Previous studies also demonstrated that the difference can be minimized by estimating the size of the short axis that is perpendicular to the maximum projection area (i.e., thickness) of each particle. However, the PSD curves before and after gyratory compaction tests in this study were both generated based on the image analysis and can therefore be compared directly, so the short-axis correction was not performed (Kumara et al. 2012; Ohm and Hryciw 2013).
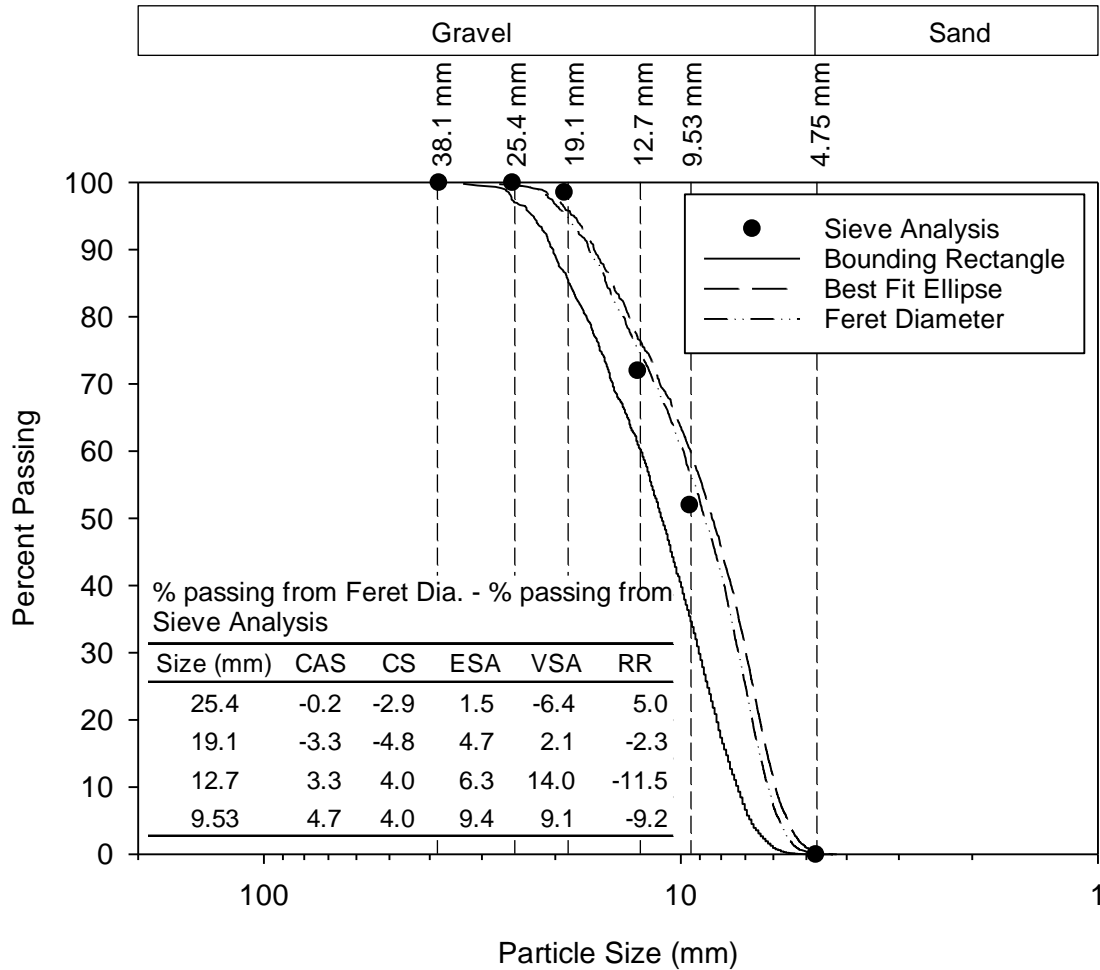
Figure 5.3. Comparison of PSD curves for ESA material determined by sieve analysis and 2D image analysis using three different methods for estimating particle sizes, with tabulated data for other materials.

To quantify the particle shapes for the various specimens, the 2D sphericity of a particle defined in (Wadell 1932) was calculated using the binary image data as

$$\text{Sphericity} = \frac{r_i}{r_c} \tag{4.16}$$

where r_i is the diameter of the largest inscribed circle of the aggregate projection area, and r_c is the diameter of the smallest circle circumscribing the projection area.

5.6. Shortcomings of LA abrasion test

According to the ASTM C131 for the LA abrasion test (ASTM 2014), depending on the original gradation of the material, the specimen must be washed and prepared to a standard grading before being tested in a rotating steel drum containing steel spheres. After the test, the specimen is washed and sieved through a 1.7 mm sieve, and the percent passing is reported as the LA abrasion loss or percent loss of the material. Because the specimen is first prepared to a standard grading, the influence of the material's original gradation on the actual abrasion performance in the field is eliminated. In this study, additional sieve analyses beyond those required by the ASTM standard were performed on each specimen to determine the gradation change of the specimens during the LA abrasion test. Interestingly, it was found that specimens of the different material types (see Table 5.1) with the same initial grading yielded very similar gradations after the test despite the different geological sources and mineral components, as shown in Figure 5.4. This phenomenon may indicate that the LA abrasion test results could be largely governed by the testing mechanism instead of the material's intrinsic properties such as mineral components, initial gradation, and morphology.
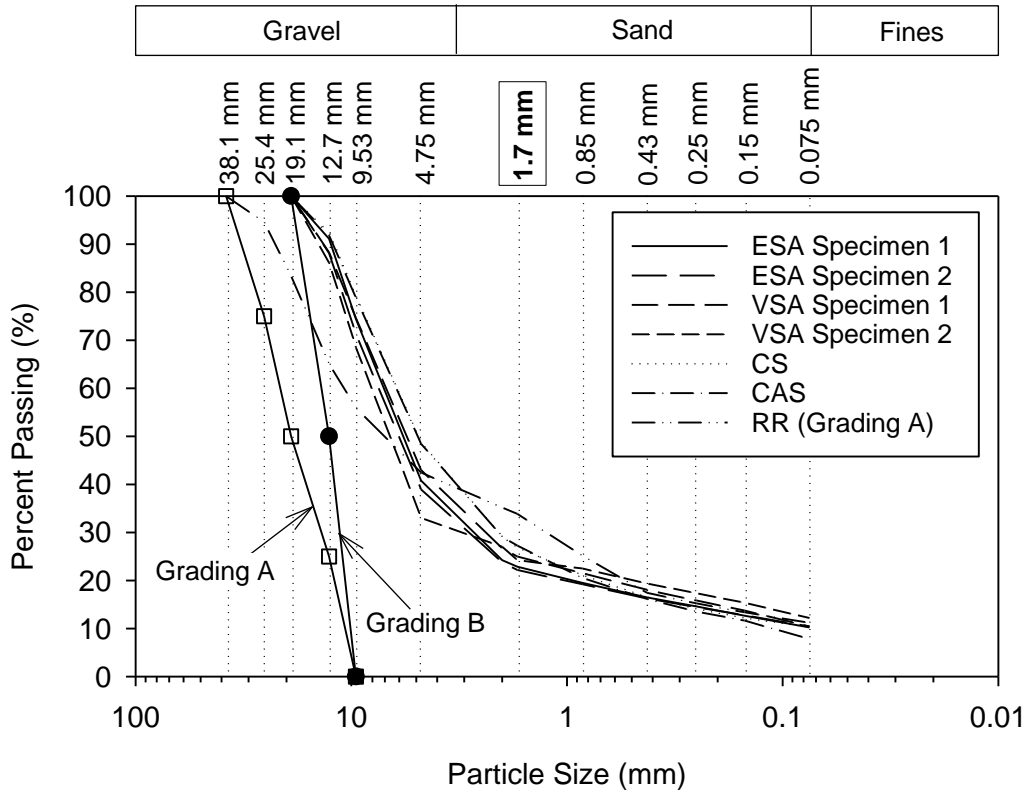
Figure 5.4. Standard initial Gradings A and B of the LA abrasion test and gradations of specimens after testing.

To compare with the LA abrasion loss values, a similar parameter can be calculated for each specimen based on the initial and final PSD curves generated using the image analysis data. To examine this idea, the parameter was taken as the difference between the initial and final PSD curves at the 4.75 mm sieve size (the smallest size available from the image analyses). Using this parameter, the gyratory compaction test results are compared with LA abrasion loss calculated using the 1.7 and 4.75 mm sieve in Figure 5.5, showing that the percent losses determined by the two testing methods are significantly different, which is expected because of the different testing mechanisms and initial gradations of the specimens.
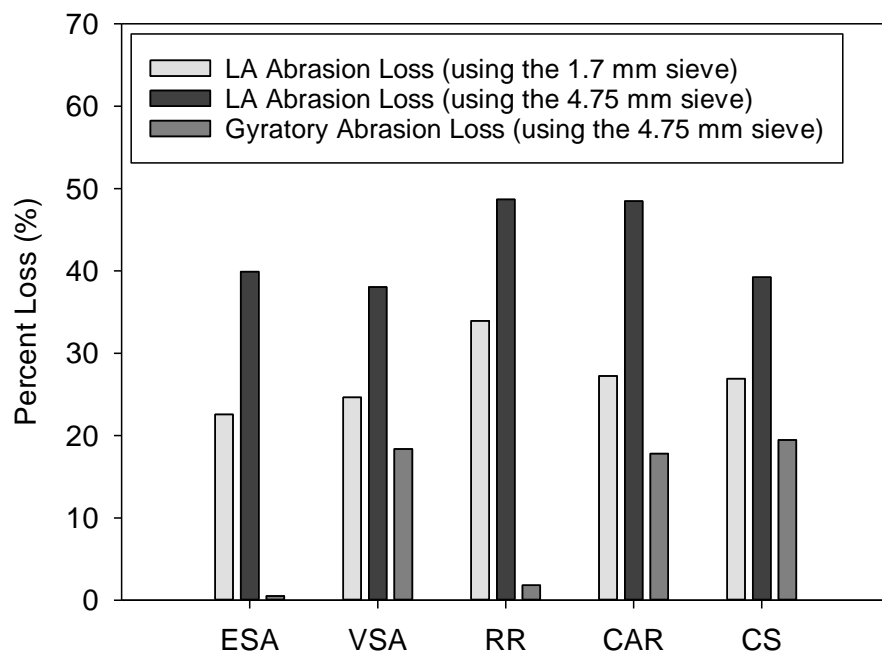
Figure 5.5. Comparison of percent abrasion loss in LA abrasion tests and gyratory compaction tests for the five specimens.

However, comparison of the PSD curves before and after the gyratory compaction test demonstrates that using a single arbitrary sieve size to quantify the degradation of a material can be misleading. This is demonstrated in Figure 5.6, in which the road rock (RR) specimen (which had the highest LA abrasion loss of 34% in Figure 5.5) exhibited a significant difference between the initial and final PSD curves, but yielded an increase of only 1.8% in the percent passing the 4.75 mm sieve after the gyratory compaction test. Therefore, the total breakage (B_t) originally proposed by Hardin (Hardin 1985) and defined as the area enclosed by the initial and final PSD curves of a material and the line of the 0.075 mm sieve size was adapted in this study to more completely quantify degradation of the gravel-size portions (>4.75 mm) of the specimens, as shown in Figure 5.6.
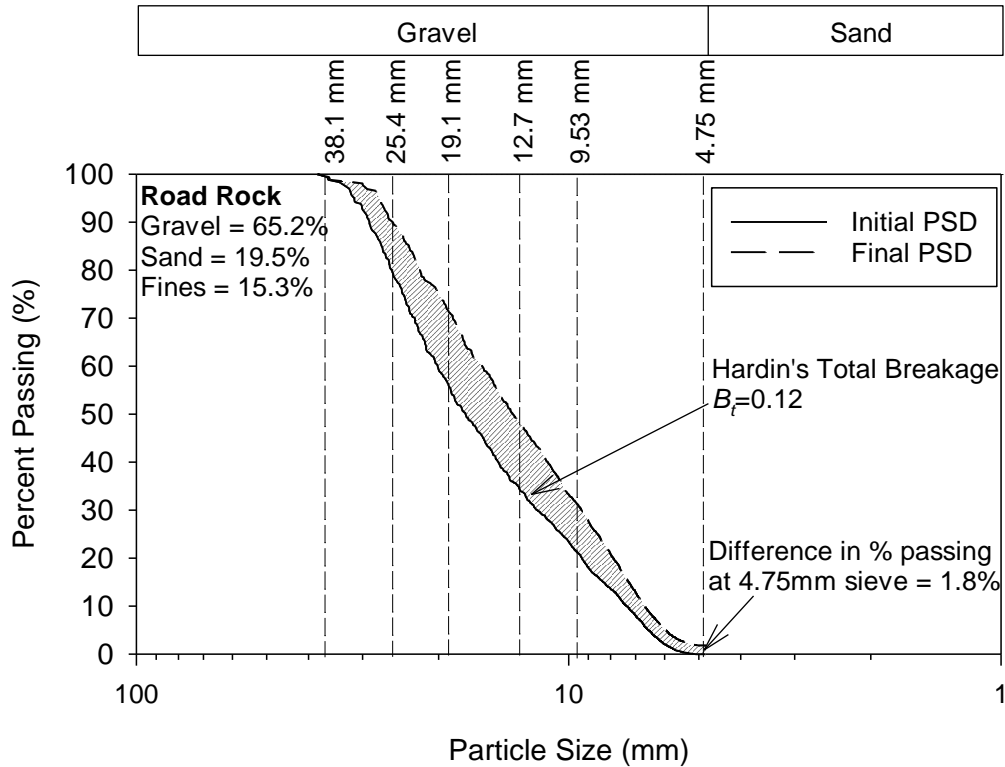
Figure 5.6. PSD curves of gravel fraction of road rock specimen before and after gyratory compaction test, as determined by 2D image analyses.

For the different material types tested in this study, a strong linear relationship was observed between the total breakage (B_t) and initial gravel content of the specimens (Figure 5.7). This strong correlation indicates that particle size distribution or particle packing significantly influences the degradation of a material. Note that this relationship does not mean that gravel content is the only parameter that governs the mechanical degradation. To predict mechanical degradation of a granular material, its gradation, morphology, void ratio, and loading condition need to be carefully considered.
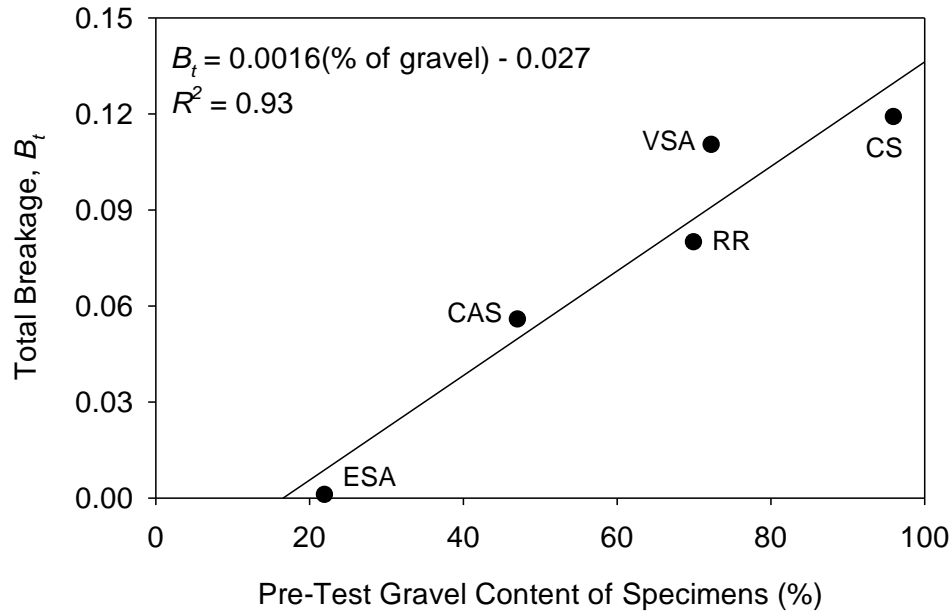
Figure 5.7. Correlation between initial gravel content of specimens and their total breakage caused by gyratory compaction tests, as measured by image analysis.

5.7. Demonstration of results from the proposed Gyratory Abrasion and Image Analysis (GAIA) test

The proposed GAIA testing method enables the mechanical gradation and morphology changes after compaction to be quantified relatively quickly, and a void ratio (or density)-strength-compaction energy relationship to be established for each specimen. This section demonstrates how such GAIA test results can be used to (1) better understand how the large-size aggregate fraction of a material abrades during compaction, and (2) set performance-based specifications for field compaction of granular materials.

In this study, the concrete stone (CS) material had the highest gravel content (96%) among the five material types tested (Table 5.1). During the gyratory compaction test on the CS specimen, approximately 20% of the initial gravel-size aggregates degraded to sandy-size particles or fines, as shown by the final PSD curve in Figure 5.8(a). To further identify which size ranges of the gravel fraction degraded the most during the test, the percent retained on

several commonly used sieves are also presented as a histogram in Figure 5.8(a). The histogram shows that the percent retained on all the sieves decreased after the test, except for the 4.75 to 9.53 mm range. This indicates that a wide range of aggregate sizes comprised the skeleton of the initial specimen and played an important structural role under compaction loading, because almost all size ranges experienced similar abrasion.

From the image analysis data, changes in particle shape (sphericity) of the aggregate were also calculated as described in Section 5.5, giving the results shown in Figure 5.8(b). The sphericity spanned a wide range from 0.4 to 0.8, so use of only a single value (e.g., median or mean) to describe the morphology of the material may not be sufficient. Therefore, box plots of sphericity in Figure 5.8(b) are used to show the distribution of sphericity for each specimen before and after gyratory compaction. As shown in these results, the median sphericity increased very slightly in all of the CS gravel size ranges examined, as small asperities and corners fractured off the aggregates from abrasion during the gyratory compaction.
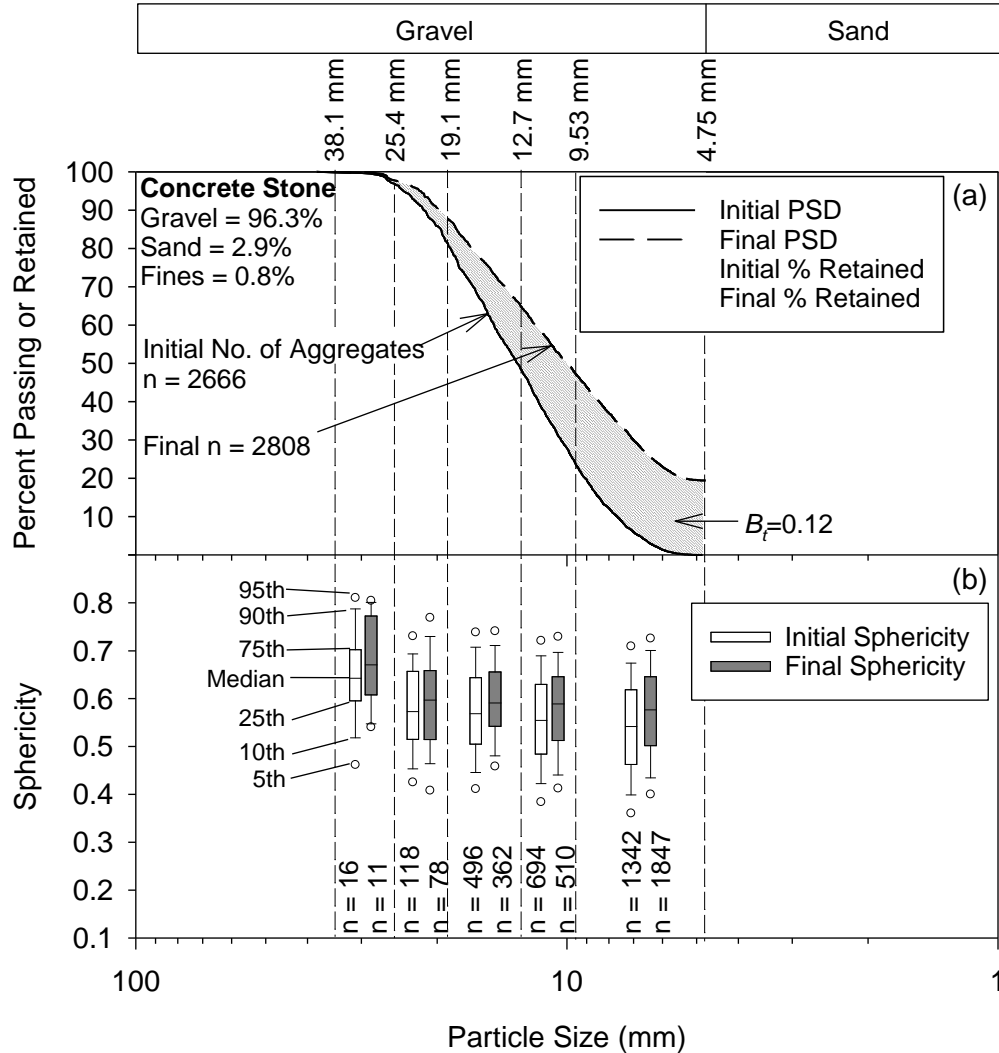
Figure 5.8. (a) Pre- and post-test gradations and (b) sphericities of the gravel-size aggregates of the concrete stone (CS) specimen determined by 2D image analysis.

Compared to the concrete stone, the existing surface aggregate (ESA) material had a much lower gravel content (24%), as this material had already been abraded by traffic for some time. The image analyses of the gravel-size fractions before and after the gyratory compaction test showed almost no change in the PSD curves and percent retained (Figure 5.9(a)), with slight changes in sphericity for the 19.1 to 25.4 mm range (Figure 5.9(b)). It can therefore be concluded that the mechanical behavior under loading was mostly governed by the sand-size particles and fines, which can not only bridge between the larger particles thus creating more contact points

thereby reducing contact stresses, but also more easily be reoriented relative to the gravel-size

particles, both of which would reduce abrasion.
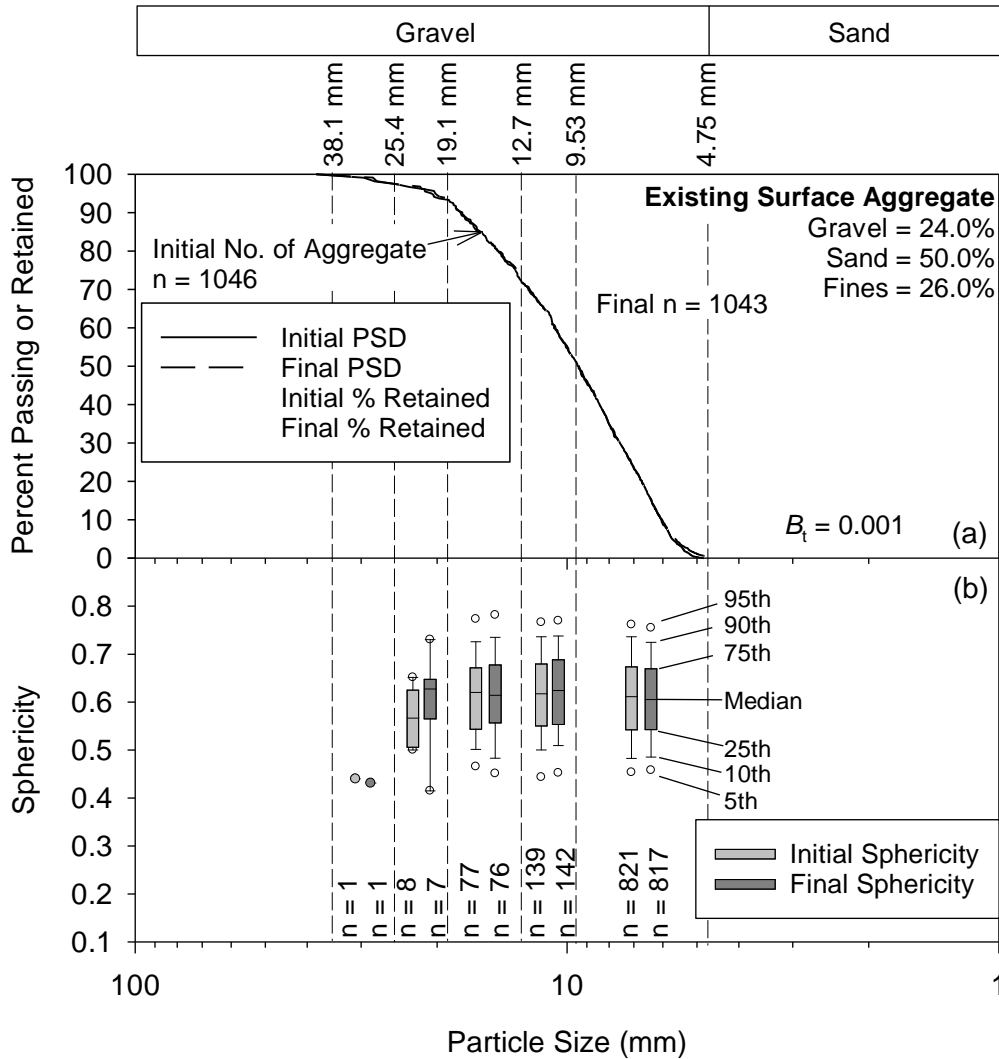
Figure 5.9. (a) Pre- and post-test gradations and (b) sphericities of the gravel-size aggregates of the existing surface aggregate (ESA) specimen determined by 2D image analysis.

The shear resistances and void ratios throughout the gyratory compaction tests were

calculated as detailed in Section 5.5. To calculate the void ratio, a specific gravity of 2.75 was

assumed for all five materials in this study. Both the shear resistance and void ratio show similar

trends for the different specimens, with rapid increases in the first 20 to 60 gyration cycles,

followed by much slower rates of change in the remaining cycles as shown in Figure 5.10. One explanation for this behavior is that the loose specimens with relatively large initial void ratios before compaction had a small number of point-to-point contacts between aggregates, but the kneading-shearing mechanism induced by the gyratory compactor effectively reoriented the aggregates while causing corner abrasions, resulting in a rapid reduction in void ratio. As the void ratio decreased, further movement of the aggregates was limited by the rigid mold, causing contact stresses between the aggregates to rapidly increase. Once contact stresses increased beyond the aggregate strengths, particle breakage and additional corner abrasions occurred, further decreasing the void ratio at a much slower rate.

The shear resistances of all the specimens in Figure 5.10 show noticeable fluctuations beyond the points of maximum curvature, whereas the void ratio curves are relatively smooth. The fluctuations in shear resistance may be due to fracture or frictional stick-slip behavior between aggregates, as well as slight dilation induced by the kneading-shearing movement of the compactor. The fluctuations also indicate that a small change in void ratio can result in a significant change in shear resistance. As mentioned previously, the gyratory compactor was stopped after 250 gyrations and two dwell gyrations were applied to the specimen before restarting, which could have caused a slight degree of dilation as shown by the jumps in void ratio at 250 gyrations for two specimens (Figure 5.10(a) and (b)). For the concrete stone specimen, a small increase in void ratio of 14% was accompanied by a significant reduction of 33% in shear resistance, but both values quickly returned towards the previous trends with additional gyrations.
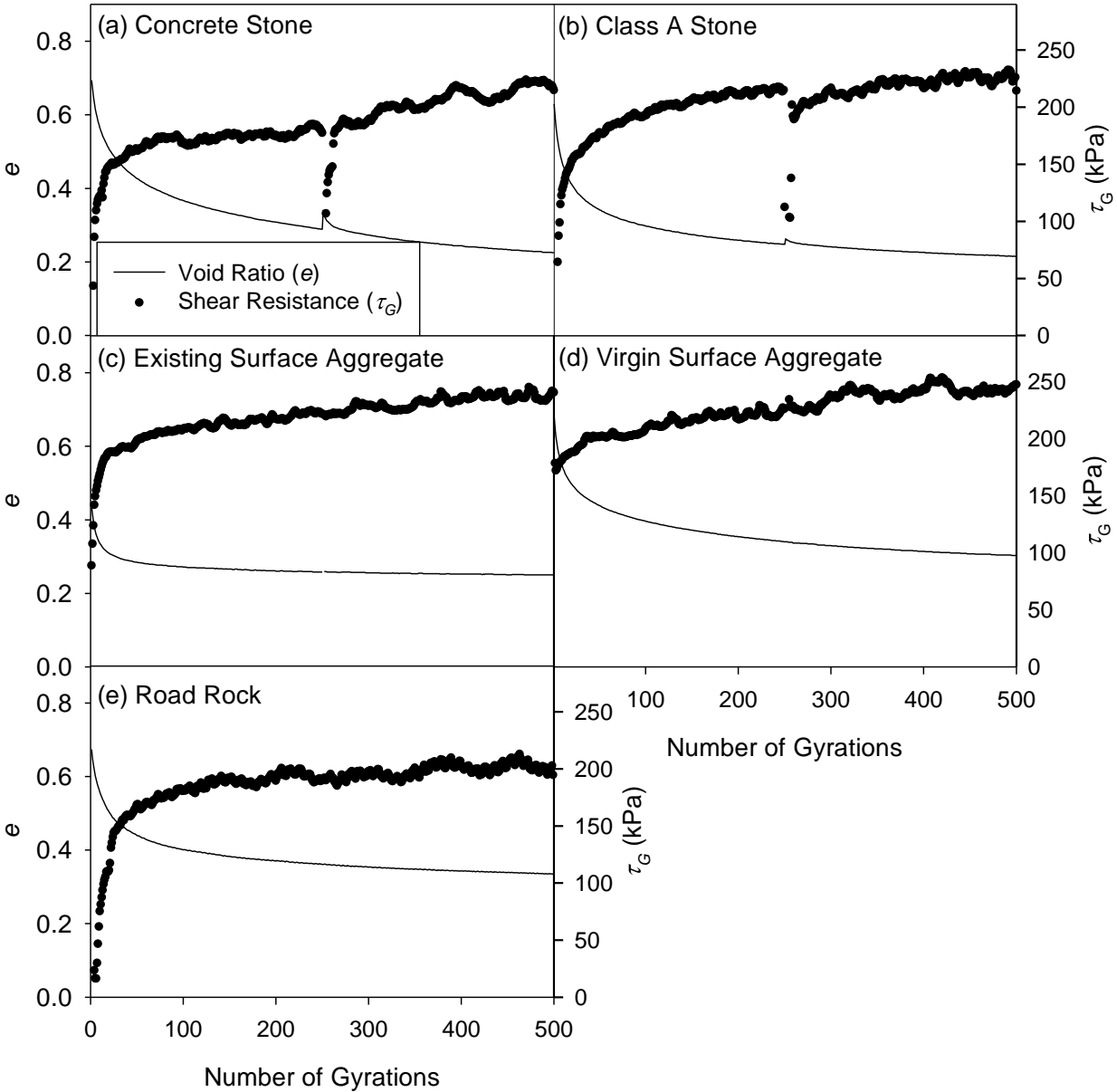
Figure 5.10. Changes in void ratio and shear resistance of the five material types during gyratory compaction tests.

Based on the test results from the range of materials types presented herein, the behavior of the specimens during the gyratory compaction test can potentially be divided into two stages. Stage I shows a rapid decrease in void ratio primarily due to particle reorientations which results in a significant increase in shear resistance, while Stage II yields much slower changes in both void ratio and shear resistance which may be caused primarily by particle breakage and abrasion.

This indicates that the point of maximum curvature of the gyratory compaction curves has an important physical meaning, and can be used to help prevent over-compaction of granular materials, which can cause significant degradation without greatly improving the mechanical properties.

The gyratory compaction test data can also be used to estabilish relationships between density, shear resistance, and compaction energy for a given granular material. An example is shown for the Road Rock in Figure 5.11, for which both shear resistance and dry unit weight increase at a much slower rate beyond the boundary between Stage I and II, corresponding to a threshold compaction energy level. Additionally, as discussed above, significantly more aggregate breakage may occur during Stage II. In this study, the maximum curvature point of the dry unit weight curve was used to define Stage I and II. The turning point was defined as the longest distance from the curve perpendicular to the line connecting the two ends of the curve (i.e., the minimum and maximum dry unit weights of the specimen), as shown in Figure 5.11.

As an improvement over current field specifications which typically simply require granular material to be compacted to a certain minimum relative density (D_r), the density-shear resistance-compaction energy relationships estabilished by the GAIA test can be used to set performance-based specifications that can give an optimum balance between compaction effort, material preservation, and performance of the compacted material, thus potentially saving significant amounts of time and energy. Further studies involving measurement of such relationships evaluated against observations of field performance for demonstration sections of different material types and gradations is recommended.

Number of Gyrations
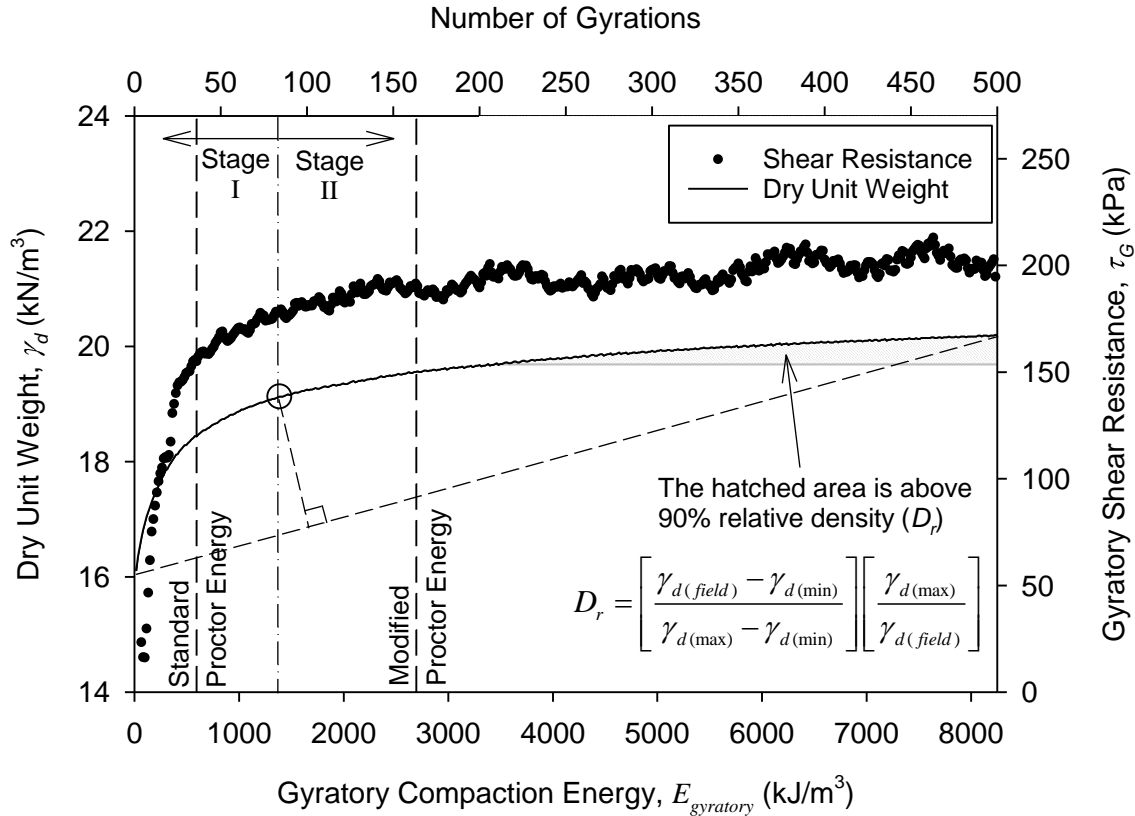
Figure 5.11. Density-shear resistance-compaction energy relationship for the Road Rock specimen.

5.8. Conclusions

In this study, the newly proposed Gyratory Abrasion and Image Analysis (GAIA) laboratory testing method was developed and applied to five different granular materials to quickly evaluate their mechanical degradation, morphology, and shear strength under gyratory compaction.

Comparisons between GAIA and the commonly used LA abrasion test revealed four main shortcomings of the latter: (1) the standard specimen gradings of the LA abrasion test may only cover a very small range of the actual material gradation used in the field; (2) the testing mechanism that involves using steel spheres to impact or crush the aggregate in a rotating steel drum does not simulate the true field compaction or loading conditions; (3) test results determined based on an arbitrary sieve size instead of accounting for the entire gradation's

change could be misleading, and (4) the test results could be largely governed by the testing mechanism instead of the material's intrinsic properties.

Based on the results presented herein, the newly proposed GAIA test can address all of the above issues. In addition, various parameters determined by the proposed test can be used to better understand the behavior of granular materials during compaction. The density-shear resistance-compaction energy relationship established based on the test results enables performance-based field specifications to be readily developed for compaction of granular materials, which can ensure final performance and save time and energy.

5.9. Acknowledgements

CHAPTER 6. IN-SITU MULTI-LAYERED NONLINEAR MODULUS REDUCTION CHARACTERISTICS OF STABILIZED UNPAVED ROADS BY SURFACE WAVE AND FALLING WEIGHT DEFLECTOMETER METHODS

A paper to be submitted to *Road Materials and Pavement Design*

Cheng Li, Jeramy C. Ashlock, Shibin Lin, and Pavana K.R. Vennapusa

6.1. ABSTRACT

Unpaved roads are prone to significant degradation and damage due to the effects of traffic, moisture, and temperature, and are often stabilized or paved to improve ride quality and reduce maintenance costs. Many agencies upgrade unpaved roads with little or no preparation of the foundation layers, and the new asphalt surfaces can rapidly deteriorate due to considerable variation in quality of the foundation materials. Therefore, quantitative nondestructive testing methods that could rapidly determine the in-situ modulus of each layer of an unpaved roadway system would provide valuable inputs for both mechanistic-based design and quality control/quality assurance in construction. Toward these goals, a newly improved multichannel analysis of surface wave (MASW) test is adapted and combined with the falling weight deflectometer (FWD) test to determine nonlinear in situ modulus reduction curves. To first assess the feasibility of using the MASW test to determine the moduli of both the unbound aggregate surface layer and subgrade, FWD and MASW tests were conducted on a total of 22 unpaved road test sections constructed using a wide range of geomaterials and various mechanical and chemical stabilization methods. Field test results showed that the elastic moduli of surface aggregate layers from the MASW tests were much higher than those from FWD tests as expected, with strong correlations except for road sections containing a geosynthetic layer. By combining the MASW and FWD moduli from different strain levels, a new method is developed

to determine in-situ nonlinear modulus reduction characteristics, which may offer improvements in mechanistic-based design methods for both paved and unpaved roads.

6.2. Introduction

Unpaved roads comprise a significant portion (approximately 2.3 million km) of the 6.6 million total kilometers of public roads and streets (FHWA 2014). However, annual maintenance costs for unpaved roads can be quite significant as they are frequently damaged by heavy agricultural traffic loads and seasonal moisture and temperature variations. Unpaved roads are therefore often stabilized or paved to improve ride quality and reduce maintenance costs. However, many agencies upgrade unpaved roads with little or no preparation of the foundation layers, and thus the new asphalt surface courses can rapidly deteriorate and also require recurring maintenance (Fay et al. 2016). To evaluate structural capacity, predict damage susceptibility, or conduct mechanistic-based upgrade designs for unpaved roads, it would be beneficial to rapidly and economically measure the in-situ elastic modulus of the existing aggregate and subgrade layers. The falling weight deflectometer (FWD) is a commonly used nondestructive testing (NDT) device for measuring physical properties of pavement systems. In an FWD test, a large dynamic impact load is applied to simulate traffic loading, while the resulting deflection basin is measured on the roadway surface. A single composite modulus or a multi-layered modulus profile of the pavement system can then be back-calculated using the measured deflection data (Crovetti et al. 1989; Hoffman and Thompson 1982). To date, however, FWD testing has not been widely used for unpaved granular-surfaced roads due to several limitations including high equipment and maintenance costs, greater required measurement ranges for the deflection sensors, and lack of consistency between different back-calculation methods.

Geophysical surface wave methods (SWM), including the widely used multichannel analysis of surface waves (MASW) method in particular, are efficient NDT tools commonly employed for profiling of elastic moduli of soil and pavement systems (Lin and Ashlock 2015; Park et al. 2001; Ryden 2004). However, MASW has not been widely applied to testing of unpaved roads with a focus on characterizing the elastic properties of both the unbound aggregate layer and top subgrade layer. In this study, a wide range of geomaterials including unconventional large aggregates (macadam stone), geosynthetics, chemical stabilizers, and recycled pavement materials were used to construct various stabilized test sections and unmodified control sections along a 3.2-km (2 mile) stretch of unpaved roadway in Iowa in 2013 and 2014. Both FWD and MASW tests were subsequently conducted at the same testing locations within the test sections. The FWD and MASW methods employ two different theories (i.e., the theory of elastic layer systems and wave propagation theory) to calculate the elastic moduli of the multi-layered unpaved road systems. In this paper, the MASW method with recent improved data analysis methods for pavement systems is briefly described, then results of MASW and FWD tests are presented and analyzed to obtain multi-layered elastic moduli for the various test sections, and correlations and discrepancies between the two methods are discussed.

6.3. MASW Tests

Surface wave methods employ the phenomenon of dispersion of surface waves in layered elastic media, to infer the layer properties (e.g., thickness and modulus) by matching experimental dispersion curves to their theoretical counterparts (Park et al. 1998; Park et al. 1999; Xia et al. 1999). In contrast to the conventional seismic reflection and refraction methods, SWM are capable of measuring modulus profiles of stiff over soft layers (Lin and Ashlock 2011), which applies to both paved and unpaved roads which typically possess stiffer surface

courses over softer subgrade layers. In MASW tests, an impact is applied on the ground surface to generate surface waves (e.g., Rayleigh waves for regular profiles with depth-wise increasing stiffness, or quasi-Lamb waves when the stiffest layer is on the surface), and the surface wave motion is measured using an array of geophones or accelerometers (Park et al. 1999).

Based on dispersion characteristics contained in the measured surface motion, the shear wave velocity as a function of depth can be back-calculated through an inversion procedure. However, when applying traditional surface wave analysis methods to pavement systems, several challenges are encountered such as numerical instability when using the transfer matrix method to calculate theoretical dispersion curves at high frequencies, and convergence to a local minimum when using the Levenberg-Marquardt method for inversion (Lin and Ashlock 2011). To address these issues, several improvements were made to the dispersion analysis and inversion procedures for MASW data analysis by Lin (Lin 2014). These include a new phase-velocity and intercept-time scanning (PIS) method to improve the resolution and sharpness of experimental dispersion images by minimizing side lobes and aliasing that can be generated by conventional wavefield transformation methods. The side lobes and aliasing can lead to misidentification of apparent higher and lower modes, resulting in errors in the inverted profiles. In addition, the new PIS dispersion analysis method does not require a complex high-accuracy trigger system, because it eliminates the assumption of the conventional methods that the impact point coincides with the generation point of the Rayleigh waves. The PIS method first converts the field data from the space-time domain to the space-frequency domain by applying a Fourier transform, then uses the slant-stack method to provide a new series of harmonic curves in the phase slowness-time intercept plane, and finally applies another Fourier transform followed by auto-power spectrum analysis to the new harmonic curves to generate the experimental

dispersion image. The key differences between the improved PIS and conventional methods are "*(1) the additional dimension of scanning the intercept time, whereas the conventional analysis assumes an intercept time of zero, and (2) the use of auto-power spectrum analysis, which presents the dispersion image amplitude in terms of power to greatly reduce effects of side lobes and aliasing" (Lin 2014).* A new hybrid genetic-simulated annealing (GSA) optimization algorithm was also developed to improve the inversion procedure by enhancing global searching efficiency, thus reducing the risk of the search becoming trapped in a local minimum. The GSA method uses a new combination of the genetic algorithm (GA) and simulated annealing (SA) algorithm, which excel at global and local searches, respectively. A flowchart and step by step optimization procedure for the GSA algorithm are detailed in Lin (2014).

6.4.   Site Descriptions and Materials

In this study, a wide range of stabilization methods were selected to construct various test sections over a 3.2 km stretch of unpaved road in Hamilton County, Iowa. Nominal cross-section profiles and materials for the various sections are shown in Figure 6.1. The design, construction, performance data, and economic analyses for each of the test sections are detailed in (Li et al. 2015). Three types of macadam stone base layers (dirty, clean, and RPCC macadam) were used with and without a non-woven (NW) geotextile layer to mechanically stabilize the first 1.6-km (1 mile) of the road. For dust control, bentonite and calcium chloride surface treatments were applied over part of the surface of two of the dirty macadam sections. The macadam materials used in this study were not bound with tar or bitumen. The clean macadam stone was sieved over a 19 mm sieve and had a maximum aggregate size of 75 mm. The dirty and RPCC macadam were well-graded with a maximum aggregate size of 127 mm. To improve subsurface drainage and minimize frost boils, aggregate column drains (200 mm in diameter and 1.83 m in depth)

118

were installed with approximately 1 column per 21 m^2 of surface area in two test sections of the second 1.6-km (second-mile) of road. Geocomposite liners were used to prevent contamination of the clean aggregate fill for one of the two sections with aggregate columns. Bentonite, Class C fly ash, and Portland cement were used to chemically stabilize the surface courses of three test sections. For the fly ash and cement sections, the existing surface aggregate (AGG) layer (~75 mm thick) was mixed with 130 mm of subgrade (SG) to obtain an SG+AGG mixture for the surface course. Geocomposite, NW-geotextile underlying biaxial (BX) geogrid, and BX-geogrid alone were placed at the interface of the subgrade and surface course for three test sections to improve subsurface drainage or mechanically stabilize the surface aggregate.

6.5. Test Setup and Calculations

The MASW and FWD tests were conducted at the same locations on the test sections in one day (Figure 6.2). On the day of testing, the fly ash- and cement-treated sections had cured for 18 and 20 days, respectively.
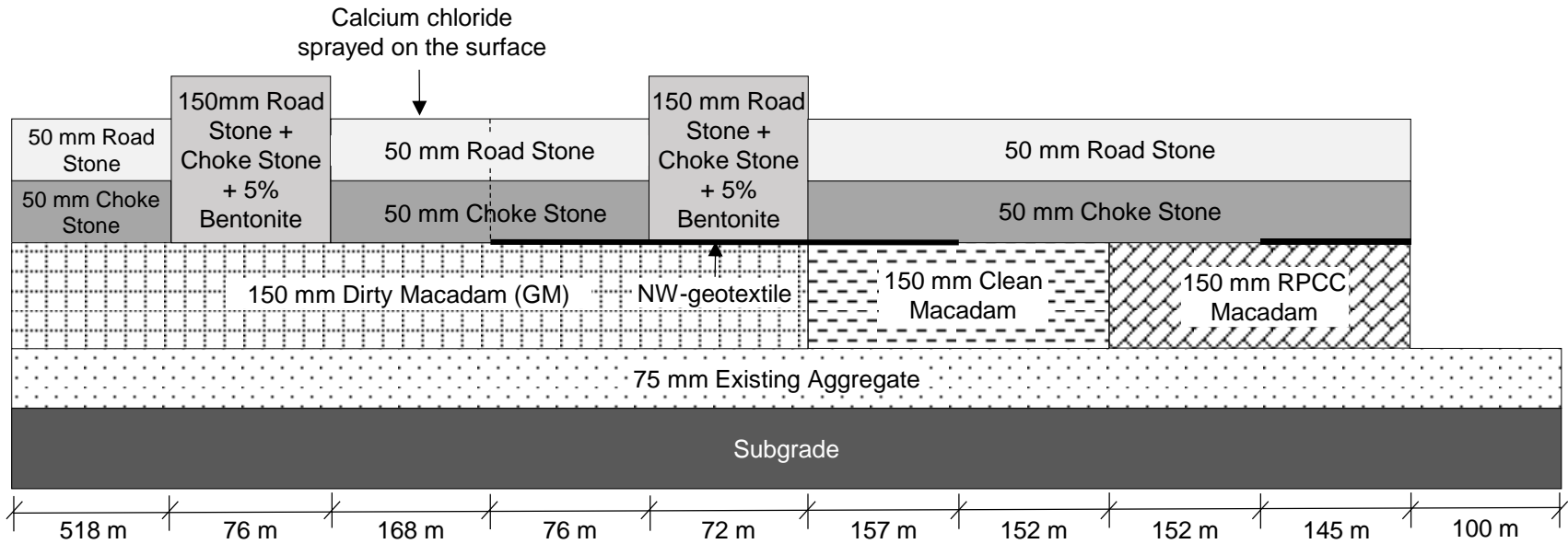
(a) The First 1.6-km Test Sections
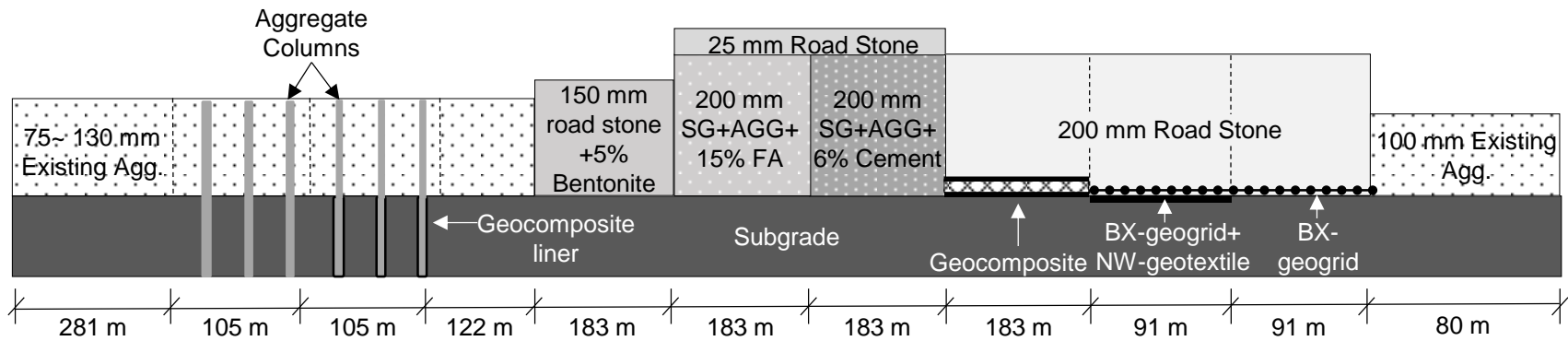
(b) The Second 1.6-km Test Sections

Figure 6.1 Nominal cross-section profiles, materials, and lengths of the first 1.6-km (top) and second 1.6-km (bottom) of test sections (not to scale).
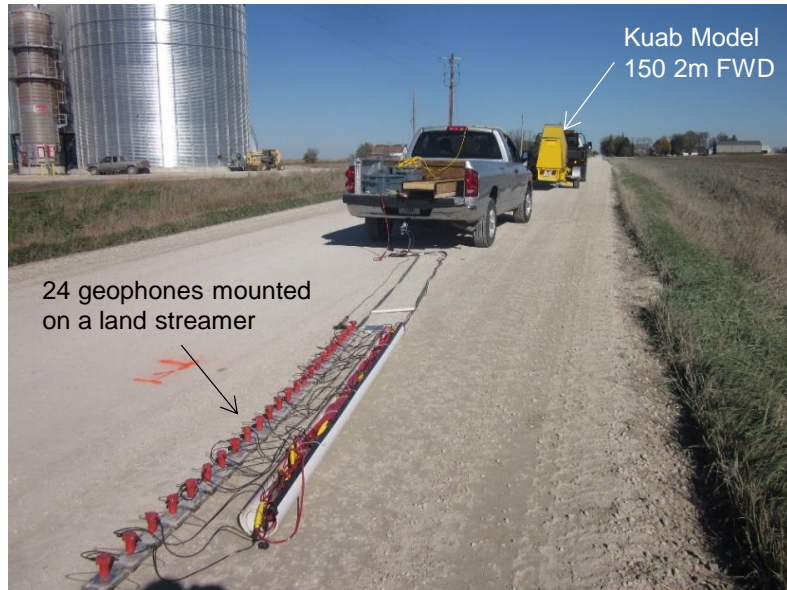
Figure 6.2. FWD and MASW testing setup.

6.5.1. Test Configurations

A Kuab Model 150 2m FWD was used, with a 300 mm diameter segmented loading plate to apply a more uniform stress distribution on the roadway surface. The Kuab contains eight seismometers with up to 1.27 cm measurement capacity that measure surface deflections over a range of offsets from the center of the loading plate. To measure elastic moduli over a range of strain levels, a static seating load was first applied, followed by four weight drops with applied dynamic pressures normalized to 378, 566, 655, and 881 kPa.

Compared to the FWD test, the MASW test typically uses a lower energy source, and a smaller 152 mm (6 in.) receiver spacing was also selected to focus the measurement resolution on the surface aggregate layer and top layer of subgrade. A 900 g triggered ball-peen hammer was used to impact a 152 mm square by 25 mm thick aluminum plate resting on the road surface to generate surface waves containing high frequencies. An array of twenty-four 4.5-Hz geophone receivers with 152 mm spacing were used to measure the vertical velocity of the roadway surface. The geophones were installed on a custom-built towed land-streamer, which

significantly reduces testing time compared to the conventional approach of installing geophones with spikes. Tests using the landstreamer on a granular road were compared to those using spikes to verify good geophone-to-ground coupling and data quality (Carnevale and Hager 2006; Van Der Veen et al. 2001). With the land streamer setup, each test takes less than two minutes. The geophone data was recorded using a 24-channel Geometrics Geode seismograph. The MASW and FWD test configurations are compared in Table 6.1.

Table 6.1. MASW and FWD test configurations.

Parameters	FWD Tests	MASW Tests
Impact source to first receiver offset (m)	0.20	0.31
Total number of receivers	8	24
Receiver spacing (m)	0.11 to 0.31 [a]	0.15
Total length of receiver spread (m)	1.52	3.51

[a] FWD seismometers were located at 0, 0.20, 0.31, 0.46, 0.61, 0.91, 1.22, and 1.52 m from center of the loading plate

To back-calculate the multi-layered elastic moduli, the thicknesses of the surface aggregate layers were estimated from dynamic cone penetrometer (DCP) test data, identified by breaks in the slope of cumulative blows versus depth, or sudden decreases in the DCP-correlated California Bearing Ratio (CBR) versus depth, as shown in Figure 6.3. All of the test sections were considered as two-layer systems (surface course + subgrade), because the road stone, choke stone, and underlying existing aggregate layers taken together are relatively thin (50 – 75 mm), and the boundaries between the material layers cannot be clearly identified by the DCP test due to the similar shear strength properties of these aggregate materials. An average thickness of the surface course layer was determined for each test section and used for both the FWD and MASW back-calculations.
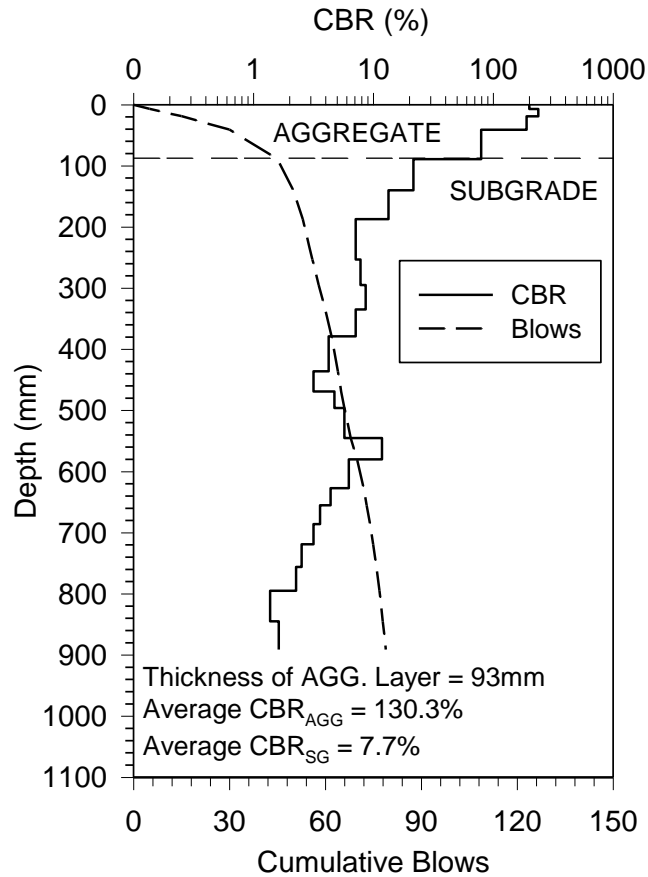
Figure 6.3 Example of using DCP data to determine thickness of surface aggregate layer.

6.5.2. Data Analysis Methods

For the FWD tests, the elastic modulus of the surface aggregate layer ($E_{FWD\text{-}AGG}$) and subgrade (($E_{FWD\text{-}SG}$) were back-calculated using an approach developed based on Boussinesq's solution and Odemark's equivalent layer thickness assumption (AASHTO 1993). Boussinesq's solution is typically used for calculating stresses, strains, and deformations at a given radius and depth in a homogeneous linear elastic half-space caused by a point load applied on the surface (Boussinesq 1885). Odemark's assumption is used to convert the thickness of the top layer to an equivalent thickness of additional subgrade material, and then match the measured surface

deflections with the theoretically calculated deflections of the equivalent single layer (Odemark 1949).

For the MASW test, the experimental dispersion trends can be extracted from the field space-time domain data using the PIS method discussed previously, to give experimental dispersion images such as the one shown in Figure 6.4a. The peaks of each dispersion image are picked algorithmically to obtain a corresponding experimental dispersion curve as shown in Figure 6.4b. To back-calculate properties of a layered profile, the GSA inversion procedure is then employed to match a theoretical dispersion curve (circles in Figure 6.4b) with the experimental counterpart (white dots in Figure 6.4a and black dots in Figure 6.4b). Using assumed densities along with the measured thickness of the surface aggregate layer and treating the subgrade as a homogenous half-space, the elastic modulus of the surface aggregate layer ($E_{MASW\text{-}AGG}$) and subgrade ($E_{MASW\text{-}SG}$) can be calculated from the back-calculated Rayleigh-wave velocities using Equation (6.1) through Equation (6.2).

$$G = V_S^2 \rho \tag{6.1}$$

$$E_{MASW-AGG} \ or \ E_{MASW-SG} = 2(1+\nu)G \tag{6.2}$$

where V_S is the shear wave velocity (m/s), V_R is the phase velocity of Rayleigh waves (m/s), ν is Poisson's ratio (assumed 0.3 for surface aggregate layer and 0.4 for subgrade), G is shear modulus (kPa), and ρ is dry density (kg/m³).
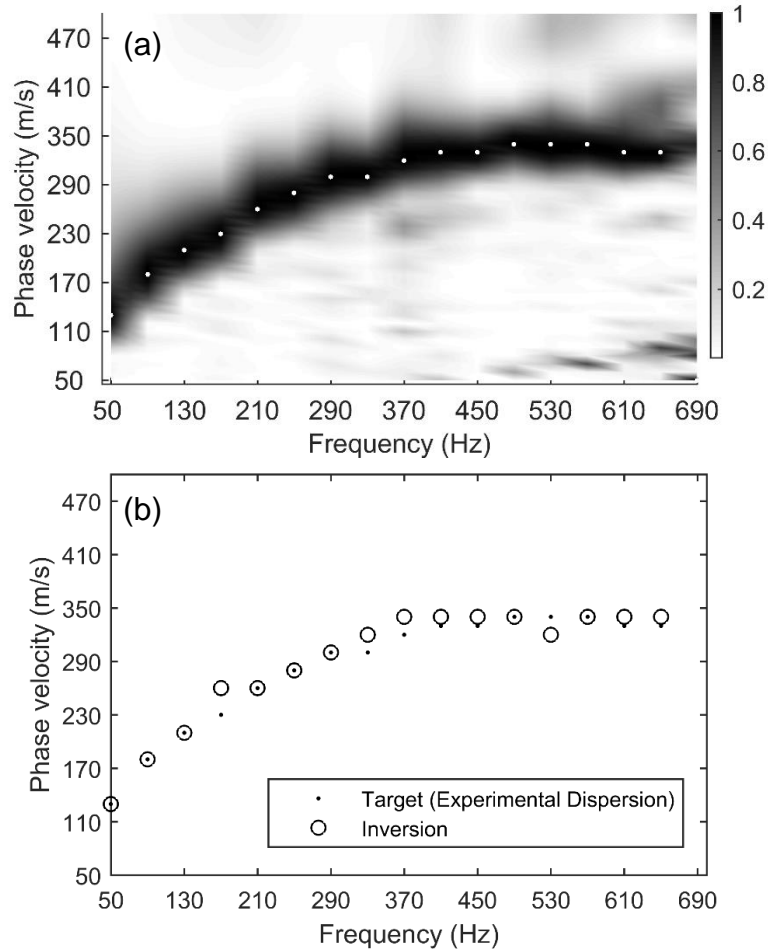
Figure 6.4 Example of (a) experimental dispersion image and (b) comparison of the dispersion curve (target) and theoretical dispersion curve from GSA inversion procedure.

6.6. Results and Discussion

The back-calculated MASW moduli for all 104 test locations are compared to those from FWD tests under the 378 kPa applied dynamic pressure in Figure 6.5 and Figure 6.6. For surface aggregate layers without an underlying geosynthetic layer the two test methods show very similar trends, with the $E_{MASW-AGG}$ values being greater than the $E_{FWD-AGG}$ ones, as shown in Figure 6.5a and Figure 6.6a. This behavior is expected, because the strains induced by the large FWD impact loads are much greater than those of the MASW tests, and it is well known that the elastic modulus of granular materials decreases nonlinearly with increasing strain levels (Hardin

and Drnevich 1972; Rollins et al. 1998; Seed et al. 1986). One exception is that the $E_{MASW\text{-}AGG}$ and $E_{FWD\text{-}AGG}$ values of the BX-geogrid stabilized section (Figure 6.6) have roughly the same mean and show similar trends. This may be due to the stabilization benefit from aggregates interlocking with the BX-geogrid being activated more under the larger strains of the FWD impact load than under the smaller MASW hammer impacts. Additionally, the trends of the two NDT tests exhibited a poorer agreement for the sections containing a geosynthetic layer. The relative lack of agreement is not surprising, as the lateral reinforcement provided by the geosynthetics violates the assumptions of Boussinesq's solution. Additionally, the influence of the geosynthetic layers on wave propagation in the multi-layered systems requires further study.

The magnitude of the MASW and FWD subgrade elastic moduli were in closer agreement than the surface course elastic moduli, but the MASW values showed significantly greater variation than the FWD ones (Figure 6.5b and Figure 6.6b). This may be a result of the small ball-peen hammer impact source used for MASW tests delivering much lower seismic energy to the subgrade than the FWD impact, resulting in lower signal to noise ratios for the MASW tests. However, the small hammer was chosen in this study to generate surface waves with greater higher frequency content, to focus the MASW measurement resolution on the relatively thin surface courses. If reduced variability in the MASW subgrade moduli is desired, a heavier impact source such as the traditionally used sledgehammer could easily be employed to generate greater seismic energy in the subgrade, along with a larger impact offset to avoid clipping of the geophone signals.
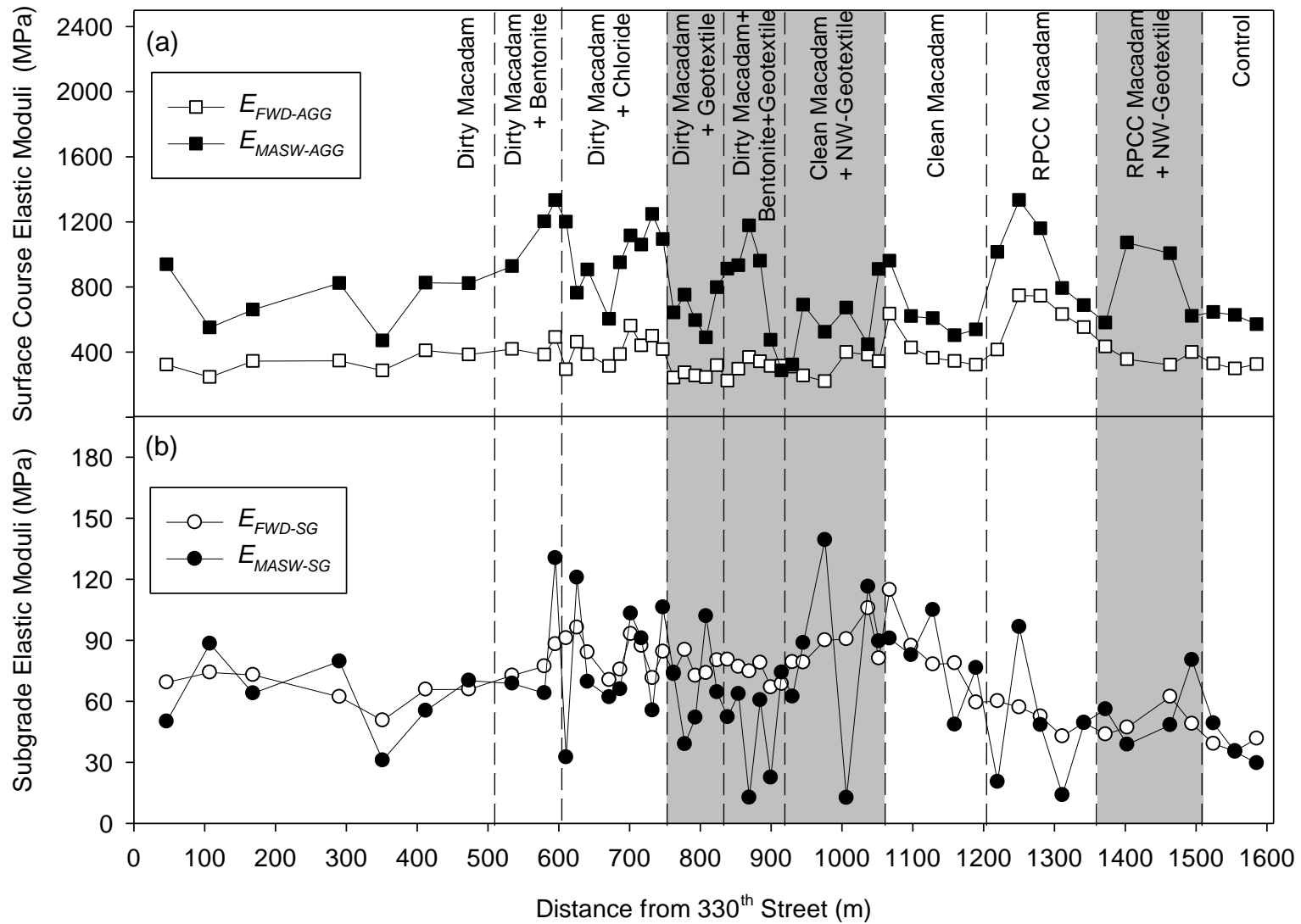
Figure 6.5 Elastic moduli from FWD and MASW tests for the first 1.6-km (first-mile) test sections: (a) surface course and (b) subgrade.

126
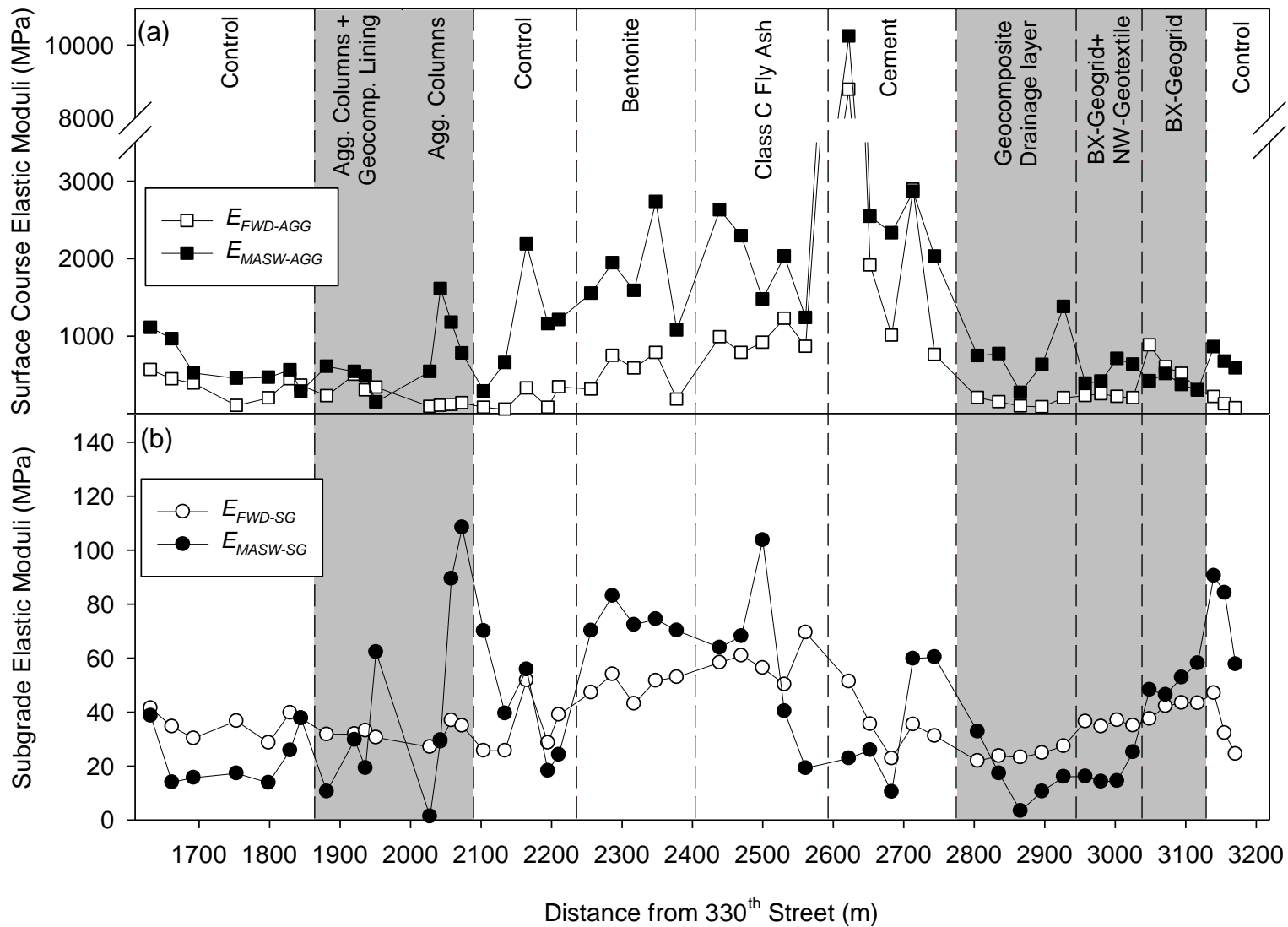
Figure 6.6 Elastic moduli from FWD and MASW tests for the second 1.6-km (second-mile) test sections: (a) surface course and (b) subgrade.

Statistical linear correlations between the moduli from MASW tests and FWD tests with the 378 kPa pressure are shown for all sections except those having a geosynthetic layer in Figure 6.7. The coefficient of determination (R^2) for the surface courses is 0.53, which is considered to be a strong correlation for in situ test data. Based on the linear correlation, the surface course moduli estimated by the MASW tests are about twice those measured under the 378 kPa pressure in the FWD tests. However, the R^2 for the subgrade is only 0.35 due to the lower energy reaching the subgrade in MASW tests because of the selected small hammer size, as discussed above.

$E_{FWD-AGG}$ (MPa) = 0.50 ($E_{MASW-AGG}$) - 38.45
R^2 = 0.53, n=61, RMSE=301.12

E_{FWD-SG} (MPa) = 0.43 ($E_{MASW-SG}$) + 31.57
R^2 = 0.35, n=62, RMSE=17.36
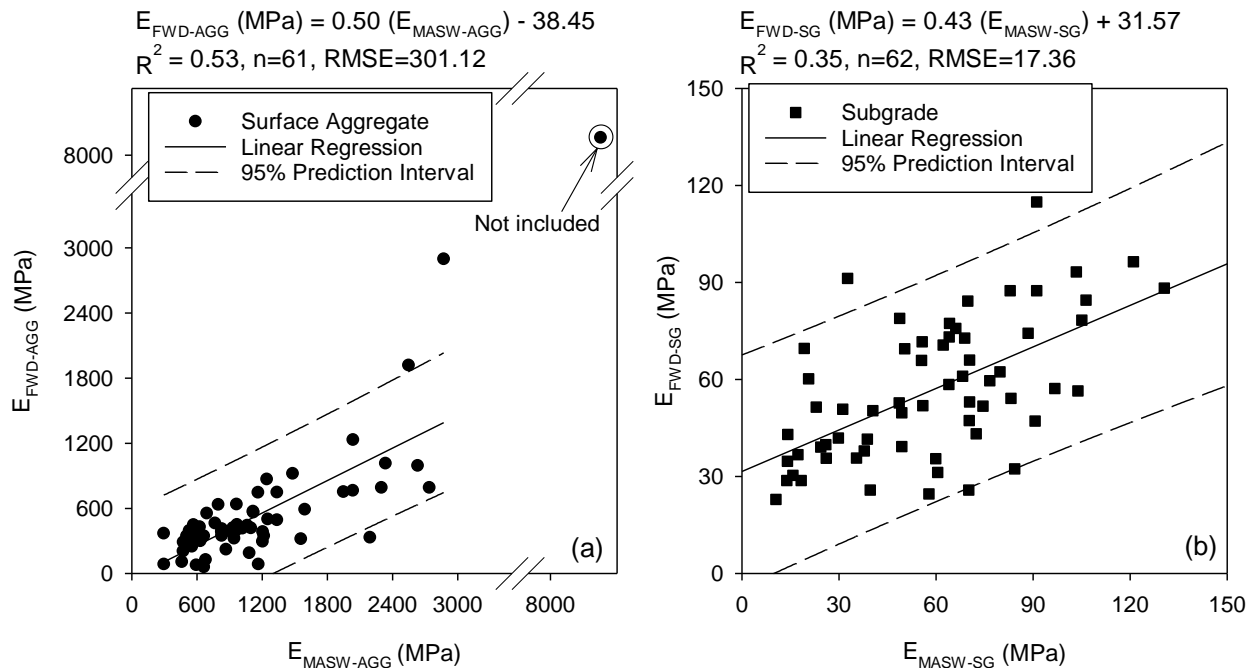
Figure 6.7 Linear correlations between MASW and FWD moduli of sections without a geosynthetic layer: (a) surface course and (b) subgrade.

For the FWD tests, four increasing impact pressures were applied at each test location, with the dynamic strains increasing with applied pressure. Linear correlations between the MASW moduli, which are assumed to all correspond to a consistent small strain level, and the FWD moduli for which strains increase with applied dynamic pressure, are summarized in Table 6.2. Linear correlations between MASW and FWD elastic moduli under different FWD pressures for

sections without geosynthetic layer. The R^2 values for the surface courses decreased significantly from 0.53 to 0.30 with increasing FWD impact pressure, but remained relatively constant between 0.33 and 0.35 for the subgrade. In addition, the slope coefficients of the linear correlations for the aggregate surface layer decreased from 0.50 to 0.26 with increasing dynamic pressure, indicating that the elastic moduli of the granular materials significantly decreased with increasing strains as expected. Therefore, the different imposed strain levels should be considered to develop a strain-modulus relationship by interpreting data from the two testing methods. This also suggests that the impact pressure level and resulting testing strain level should be carefully considered when using the field-determined elastic moduli for mechanistic-based design for both paved and unpaved road systems.

Table 6.2. Linear correlations between MASW and FWD elastic moduli under different FWD pressures for sections without geosynthetic layer

FWD Pressure (kPa)	Surface Courses		Subgrade	
	Correlations [a]	R^2	Correlations [b]	R^2
378	$E_{FWD\text{-}AGG} = 0.50\, E_{MASW\text{-}AGG} - 38.45$	0.53	$E_{FWD\text{-}SG} = 0.43\, E_{MASW\text{-}SG} + 31.57$	0.35
566	$E_{FWD\text{-}AGG} = 0.42\, E_{MASW\text{-}AGG} + 18.31$	0.49	$E_{FWD\text{-}SG} = 0.40\, E_{MASW\text{-}SG} + 29.27$	0.34
755	$E_{FWD\text{-}AGG} = 0.36\, E_{MASW\text{-}AGG} + 63.35$	0.44	$E_{FWD\text{-}SG} = 0.39\, E_{MASW\text{-}SG} + 27.92$	0.33
881	$E_{FWD\text{-}AGG} = 0.26\, E_{MASW\text{-}AGG} + 129.42$	0.30	$E_{FWD\text{-}SG} = 0.39\, E_{MASW\text{-}SG} + 25.38$	0.33

In this study, the program KENLAYER (Huang 2004) was used to develop a physics-based method for determining the inherent material nonlinear modulus-strain relationships from FWD and MASW data. Stresses, strains, and deformations at different depths within the unpaved road systems were calculated in KENLAYER for each of the FWD test locations and dynamic impact pressures. All test sections were modelled as two-layer systems, with the elastic moduli determined for the surface courses and subgrade from FWD testing used as inputs to the program. Typical comparisons between the field-measured and KENLAYER-calculated FWD roadway surface deflections are shown in Figure 6.8. Overall, the experimental and theoretical

deflections exhibit good agreement, indicating that the calculated values from the equivalent-linear KENLAYER models are reliable at the different strain levels. However, for the sections with a geosynthetic layer, the measured deflections are typically larger than the computed ones, especially for the two sensors closest to the loading plate. This phenomenon is possibly due to the tension forces generated within the NW-geotextile layer, which tend to distribute the FWD impact load over a larger area than the sections without a NW-geotextile, yielding greater deflections for the sensors close to the loading plate. Another possibility is the compliance of the geotextile layer resulting in the overlying surface course slightly decoupling from the underlying layer, causing the surface wave behaviour to approach that of a plate structure, with less energy propagating to the subgrade. For the dirty and clean macadam sections, greater discrepancies are also observed between the measured and calculated deflections as the FWD impact pressure increases. These discrepancies are possibly due to frictional sliding between macadam stones under the larger FWD impact loads.
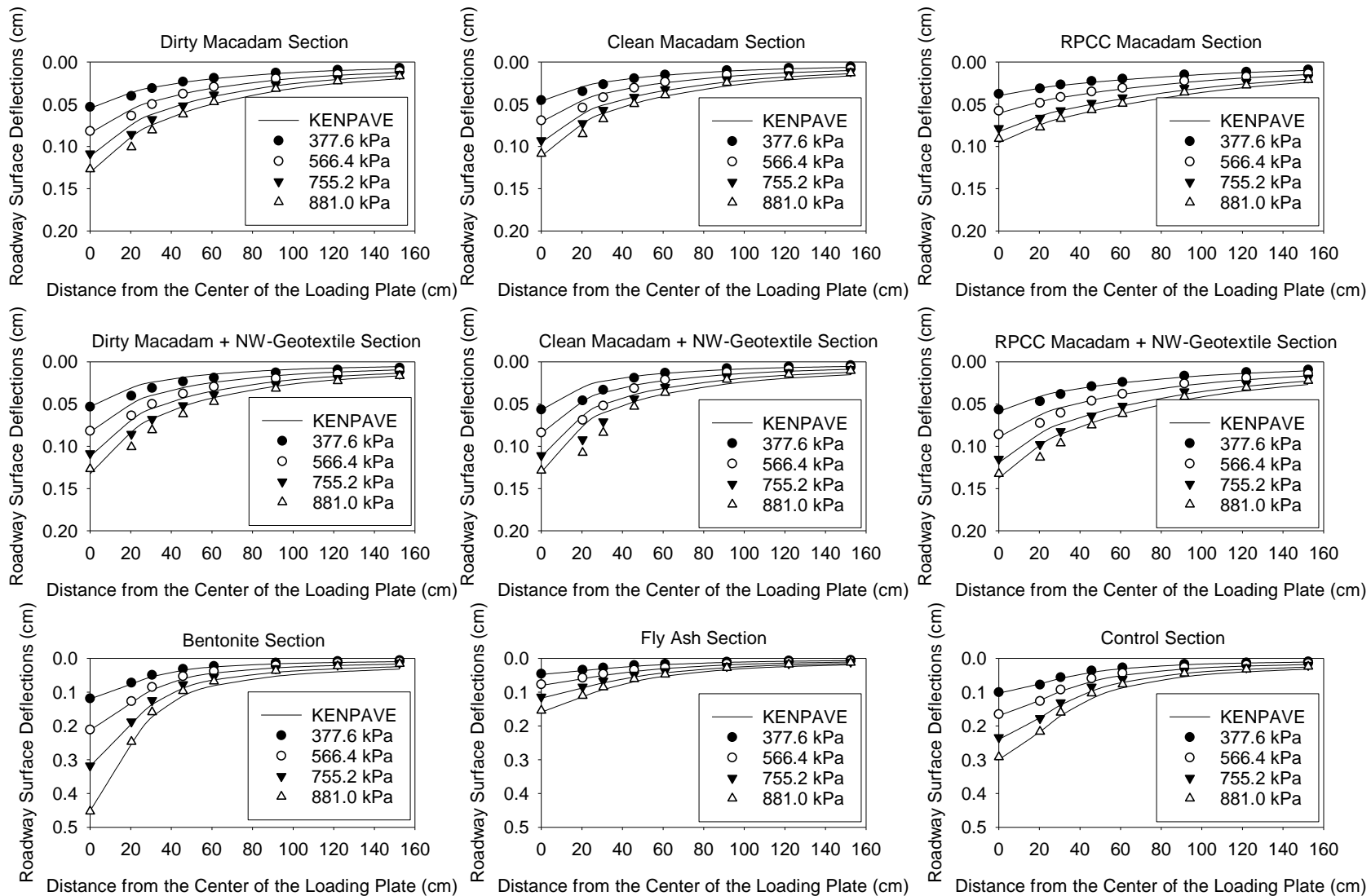
Figure 6.8 Comparisons between typical field-measured deflection data and KENPAVE-calculated deflections for the various test sections.

131

For all the sections without a geosynthetic layer, the MASW moduli were combined with those from the different calculated strain levels in the FWD tests to obtain nonlinear modulus reduction curves for both the surface courses and subgrades (Figure 6.9). The FWD strain levels were calculated at the mid-depth of the surface courses and at 15 cm below the subgrade surface. The MASW strain levels were assumed to be 10-5 % for the surface courses and 10-4 % for subgrade, based on several references (Das and Das 2011; Lytton 1989; Ryden and Mooney 2009). The strain level in the subgrade was assumed to be greater than that in the surface course, because the subgrade moduli are only approximately 5% of the surface course moduli. Figure 6.9a shows that the surface courses of the three macadam sections and the control section yield similar trends, and all contain aggregate materials with less than 20% non-plastic fines. The surface courses of the bentonite, fly ash, and cement sections exhibited significantly greater modulus reductions with increasing strain, which can possibly be attributed to breaking of the weak cementation bonds, and the relatively higher clay contents in the surface courses of these sections. Specifically, 5% bentonite by dry mass was mixed with the surface aggregate in the bentonite section, and the surface material of the fly ash and cement section consisted of 33% existing aggregate and 67% subgrade by volume. Figure 6.9b shows that the modulus reduction characteristics of the subgrade materials vary within comparatively smaller ranges, except for the dirty and clean macadam sections, which yielded higher subgrade elastic moduli at a given strain level. However, because the subgrade material can be considered to be the same under all sections, the higher moduli of the dirty and clean macadam sections may be due to the increased confining stress caused by the heavy macadam stone base layers
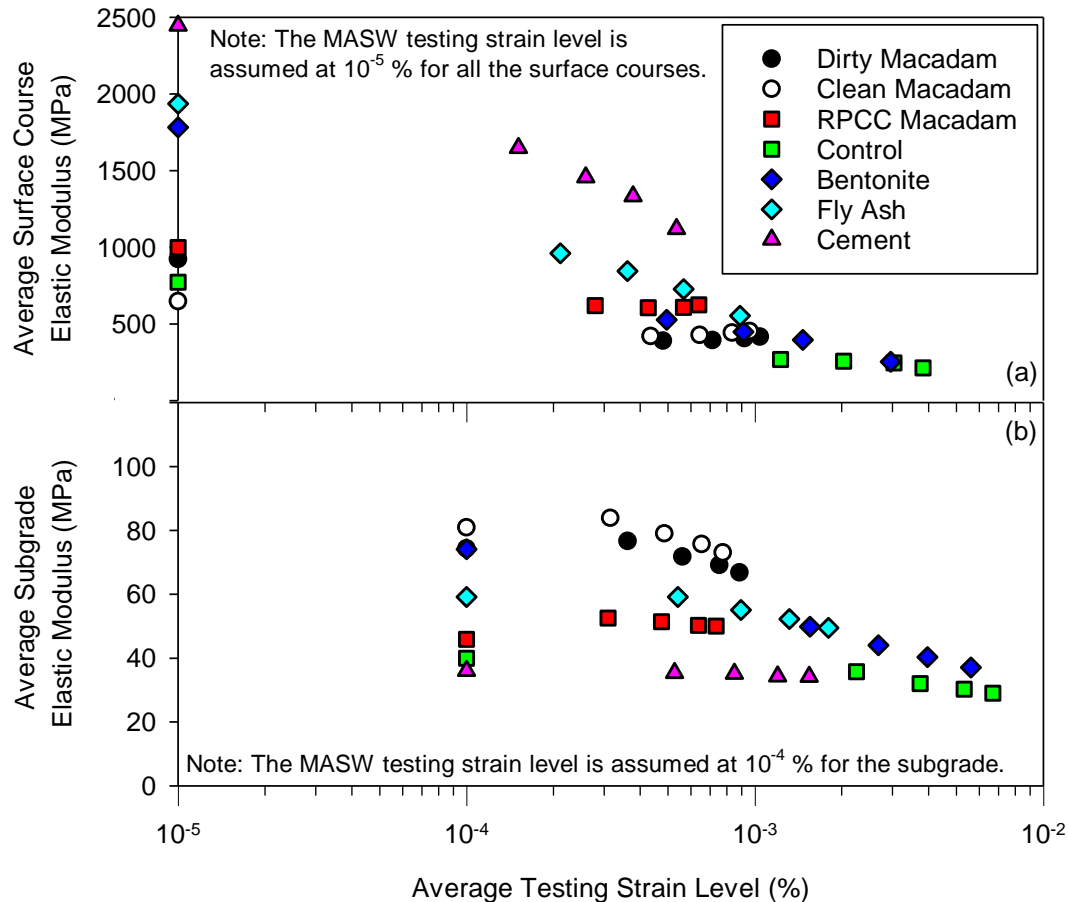
Figure 6.9 Average elastic modulus versus average strain level in MASW and FWD tests for surface course and subgrade, for test sections without a geosynthetic layer.

6.7.   Summary and Conclusions

In this paper, results from nondestructive MASW and FWD tests on various mechanically

and chemically stabilized unpaved road test sections were analyzed. The results showed that the

MASW test with recently developed improved data analysis methods and a custom-built land-

streamer was capable of measuring multi-layered elastic moduli of several types of stabilized and

unstabilized unpaved road systems. The testing results and linear correlations presented herein

covered a wide range of geomaterials and commonly used stabilization methods. The MASW

and conventional FWD methods exhibited a relatively strong linear correlation ($R^2 = 0.53$) for

surface courses of sections without a geosynthetic layer, but the R^2 values decreased significantly

as the FWD testing strain level increased. The linear correlations between the two NDT methods were not statistically significant for the subgrade, and the MASW-measured subgrade moduli showed significantly greater variation than the FWD moduli due to the small hammer size chosen and consequent smaller strains. A heavier impact source with a longer impact offset could be employed to generate greater seismic energy in the subgrade to improve the signal to noise ratio and reduce variability of the back-calculated subgrade moduli.

It was demonstrated that in situ nonlinear modulus reduction curves could be determined for both the surface course and subgrade layers, by optimizing deflections calculated using KENLAYER against the FWD data to determine the corresponding strain levels, and combining with the MASW data at very small strain levels.

The large amount of field testing data provide a better understanding about capabilities and discrepancies of the two testing methods, and are useful for estimating FWD moduli from more economical MASW tests. The data and analyses presented herein also showed that the elastic moduli of the granular layers could reduce by more than two times as the testing strain level increases. This demonstrates that the testing strain level should be carefully considered when using either FWD or MASW tests on unpaved roads, or in general when using field-determined elastic moduli as inputs for mechanistic-based designs of both paved and unpaved roads.

CHAPTER 7. CONCLUSIONS AND RECOMMENDATIONS

Unpaved roads are a critical component of public transportation systems, especially in rural and suburban areas. Compared to paved roads, unpaved roads in seasonally frozen climate regions are more prone to freeze-thaw and moisture related damage. The goal of this study was to improve performance and sustainability of unpaved roads. Specific conclusions and key findings of each research article are provided in the previous chapters. This chapter provides general conclusions from this study and recommendations for future research and practice.

7.1. Stabilization Methods for Improving Freeze-Thaw Performance of Unpaved Roads

- Among the various stabilization methods assessed in this study, the macadam stone base (MSB) sections showed the best overall performance and the highest stiffness for both pre-freezing and post-thawing periods.

- The as-constructed stiffness of the Iowa DOT-specified clean macadam material was not statistically higher than the dirty macadam or the RPCC macadam materials, despite both of the latter being classified as marginal by the DOT specifications due to their gradations.

- The average stiffness of the dirty macadam base layer suffered the greatest reduction (~26%) one year after construction, but the RPCC macadam layer showed an increase in modulus of approximately 25% one year after construction, due to the beneficial effects of further hydration of the Portland cement.

- Compared to the control sections, the aggregate column and geocomposite sections did not have significantly higher stiffnesses, but these stabilization methods were quite effective at reducing water drainage-related damage during thawing periods.

7.2. The MASW Test for Evaluating in-situ Multilayered Stiffness Profiles of Unpaved Roads

- The MASW test with recently improved data analysis methods and a custom-built land-streamer can be used to quickly evaluate multi-layered elastic moduli of unpaved road systems.

- The MASW and conventional FWD methods show a relatively strong linear correlation ($R^2 = 0.53$) for surface aggregate layers without a geosynthetic layer, but the MASW-measured subgrade moduli showed significantly greater variation than the FWD moduli due to the small seismic energy delivered to the subgrade because of the small hammer size used, resulting in lower signal to noise ratios for the MASW tests. More energy can be delivered to the subgrade by selecting a larger hammer and greater offset distance.

- The roadway surface deflections calculated using Burmister's layered theory agreed very well with the field FWD-measured deflection data, therefore the KENLAYER program which was developed based on the same theory can be used to estimate the FWD testing strain levels in the surface course and subgrade.

- The MASW and FWD test results can be combined to develop in-situ nonlinear modulus reduction characteristics of both the surface course and subgrade layer, which can be used to optimize mechanistic-based design methods for both paved and unpaved roads.

7.3. The GAIA Test for Evaluating Degradation and Compaction Behaviors of Granular Materials

- The newly developed Gyratory Abrasion and Image Analysis (GAIA) laboratory testing method can address several limitations of the conventionally used Los Angles (LA)

abrasion and Micro-deval tests for evaluating the mechanical degradation of granular materials.

- The GAIA test can quickly quantify the changes in gradation, morphology, and shear resistance of granular materials that occur under simulated field compaction loads, and provide insight into the mechanical behavior of granular materials during compaction.

- The density-shear resistance-compaction energy relationships that can be established using GAIA test results enable performance-based field specifications to be readily developed for compaction of granular materials, to better ensure final field performance, reduce material loss, and save time and energy.

7.4. Recommendations

Several directions for further research related to the demonstration project and the MASW and GAIA test methods are recommended below:

- Field tests and continued documentation of maintenance activities are recommended to further quantify the durability and long-term performance of the MSB sections, as well as to better estimate their life cycle costs.

- The diameter, depth, and spacing of the aggregate columns which function as drainage basins for unpaved road systems during thawing periods need to be optimized for different subgrade types using numerical analysis and lab tests.

- The newly proposed method that employs MASW and FWD tests to determine the in-situ non-linear multi-layered modulus reduction curves needs to be validated using laboratory resilient modulus or resonant column tests.

- Correlations between the equipment operation parameters of the gyratory compactor and the operation weights, frequencies, and amplitudes of field vibratory rollers need to be determined for a range of granular material types.

- The effects of the operation parameters of vibratory rollers on degradation of granular materials need to be evaluated, and used to develop specifications for controlling the operational parameters of vibratory compactors to minimize compaction-related degradation and maximize the long-term performance of the granular materials.

BIBLIOGRAPHY

AASHTO (1993). *AASHTO Guide for Design of Pavement Structures*, American Association of State Highway and Transportation Officials, Washington, D.C.

AASHTO (2004). "Guide for Mechanistic-Empirical Design of New and Rehabilitated Pavement Structures." NCHRP 1-37A Draft Final Report.

Abu-Farsakh, M. Y., Akond, I., and Chen, Q. (2016). "Evaluating the Performance of Geosynthetic-Reinforced Unpaved Roads Using Plate Load Tests." *International Journal of Pavement Engineering*, 17(10), 901—912.

Airey, G. D., Hunter, A. E., and Collop, A. C. (2008). "The Effect of Asphalt Mixture Gradation and Compaction Energy on Aggregate Degradation." *Construction and Building Materials*, 22(5), 972—980.

Al-Rousan, T., Masad, E., Tutumluer, E., and Pan, T. (2007). "Evaluation of Image Analysis Techniques for Quantifying Aggregate Shape Characteristics." *Construction and Building Materials*, 21(5), 978—990.

Andersland, O. B., and Ladanyi, B. (2004). *Frozen Ground Engineering*, John Wiley & Sons, Hoboken, New Jersey.

ASTM (2013). "Standard Test Method for Use of the Dynamic Cone Penetrometer in Shallow Pavement Applications." *Annual book of ASTM standards, ASTM 6951-09*, ASTM, West Conshohocken, PA.

ASTM (2014). "Standard Test Method for Preparation and Determination of the Relative Density of Asphalt Mix Specimens by Means of the Superpave Gyratory Compactor." ASTM International, West Conshohocken, PA.

ASTM (2014). "Standard Test Method for Resistance of Coarse Aggregate to Degradation by Abrasion in the Micro-Deval Apparatus." *Annual book of ASTM standards, ASTM D6928-10*, ASTM, West Conshohocken, PA.

ASTM (2014). "Standard Test Method for Resistance to Degradation of Small-Size Coarse Aggregate by Abrasion and Impact in the Los Angeles Machine." *Annual book of ASTM standards, ASTM C131/C131M-14*, ASTM, West Conshohocken, PA.

ASTM (2014). "Standard Test Method for Sieve Analysis of Fine and Coarse Aggregates." *Annual book of ASTM standards, ASTM C136/C136M‑14*, ASTM, West Conshohocken, PA.

Azadegan, O., Yaghoubi, E., and Li, J. (2013). "Evaluation of The Performance of Lime and Cement Treated Base Layers in Unpaved Roads." *Electronic Journal of Geotechnical Engineering*, 18(D), 647—660.

Bahador, M., Evans, T. M., and Gabr, M. A. (2013). "Modeling Effect of Geocomposite Drainage Layers on Moisture Distribution and Plastic Deformation of Road Sections." *Journal of Geotechnical and Geoenvironmental Engineering*, 139(9), 1407—1418.

Bahar, R., Benazzoug, M., and Kenai, S. (2004). "Performance of Compacted Cement-Stabilised Soil." *Cement and Concrete Composites*, 26(7), 811—820.

Bahia, H. U., and Faheem, A. F. (2007). "Using the Superpave Gyratory Compactor to Estimate Rutting Resistance of Hot-Mix Asphalt." *Transportation Research E-Circular,* E-C124, 45—61.

Barber, V. C., Odom, E. C., and Patrick, R. W. (1978). "The Deterioration and Reliability of Pavements." *Technical Report S-78-8*, U.S. Army Engineers Waterways Experiment Station, Vicksburg, MS.

Barrett, P. J. (1980). "The Shape of Rock Particles, A Critical Review." *Sedimentology*, 27(3), 291—303.

Berg, K. C. (1998). "Durability and Strength of Activated Reclaimed Iowa Class C fly Ash Aggregate in Road Bases."M.S. Thesis, Department of Civil Engineering, Iowa State University, Ames, Iowa.

Bergeson, K. L., and Barnes, A. G. (1998). "Iowa Thickness Design Guide for Low Volume Roads Using Reclaimed Class C Fly Ash Bases." Iowa State University, Ames, Iowa.

Bergeson, K. L., Waddingham, J. W., Brocka, S. G., and Lapke, R. K. (1995). "Bentonite Treatment for Economical Dust Reduction on Limestone Surface Secondary Roads." Project HR-351, Iowa Department of Transportation, Ames, Iowa, 99.

Bergeson, K. L., and Wahbeh, A. M. (1990). "Development of an Economic Dust Palliative for Limestone Surfaced Secondary Roads." Project HR-297, Iowa Department of Transportation, Ames, Iowa, 64.

Berthelot, C., and Carpentier, A. (2003). "Gravel Loss Characterization and Innovative Preservation Treatments of Gravel Roads: Saskatchewan, Canada." *Eight International Conference on Low-Volume Roads 2003, June 22, 2003 - June 25, 2003*, National Research Council, Reno, NV, United states, 180—184.

Bin-Shafique, S., Rahman, K., Yaykiran, M., and Azfar, I. (2010). "The Long-Term Performance of Two Fly Ash Stabilized Fine-Grained Soil Subbases." *Resources, Conservation and Recycling*, 54, 666—672.

Bolander, P., Marocco, D., and Kennedy, R. (1995). "Earth and Aggregate Surfacing Design Guide for Low Volume Roads." U.S. Forest Service, Federal Highway Administration, Washington, DC, 312.

Boussinesq, J. (1885). *Application des Potentiels à l'Étude de l'Équilibre et du Mouvement des Solides Elastiques*, Gauthier-Villars, Paris.

Bowles, J. E. (1996). *Foundation Analysis and Design*, The McGraw-Hill Companies, Inc., New York.

Butcher, M. (1998). "Determining Gyratory Compaction Characteristics Using Servopac Gyratory Compactor." *Transportation Research Record: Journal of the Transportation Research Board,* 1630, 89—97.

Carnevale, M., and Hager, J. (2006). "Effect of Sources and Geophone Coupling on MASW Surveys." *Proc., 19th EEGS Symposium on the Application of Geophysics to Engineering and Environmental Problems*, Environmental and Engineering Geophysical Society (EEGS), 10.

Cerni, G., and Camilli, S. (2011). "Comparative Analysis of Gyratory and Proctor Compaction Processes of Unbound Granular Materials." *Road Materials and Pavement Design*, 12(2), 397—421.

Cetin, B., Aydilek, A. H., and Guney, Y. (2010). "Stabilization of Recycled Base Materials with High Carbon Fly Ash." *Resources, Conservation and Recycling*, 54(11), 878—892.

Chen, D.-H., Hong, F., and Zhou, F. (2011). "Premature Cracking from Cement-Treated Base and Treatment to Mitigate Its Effect." *Journal of Performance of Constructed Facilities*, 25(2), 113—120.

Chen, X., and Zhang, J. (2016). "Effect of Load Duration on Particle Breakage and Dilative Behavior of Residual Soil." *Journal of Geotechnical and Geoenvironmental Engineering*, 142(9).

Cheung, L. W., and Dawson, A. (2002). "Effects of Particle and Mix Characteristics on Performance of Some Granular Materials." *Transportation Research Record: Journal of the Transportation Research Board*, 1787, 90—98.

Cho, G.-C., Dodds, J., and Santamarina, J. C. (2006). "Particle Shape Effects on Packing Density, Stiffness, and Strength: Natural and Crushed Sands." *Journal of Geotechnical and Geoenvironmental Engineering*, 132(5), 591—602.

Christopher, B. R., Hayden, S. A., and Zhao, A. (2000). "Roadway Base and Subgrade Geocomposite Drainage Layers." *The Symposium of 'Testing and Performance of Geosynthetics in Subsurface Drainage*, ASTM, Seattle, WA, USA, 35—51.

Chu, T. Y., Davidson, D. T., Goecker, W. L., and Moh, Z. C. (1955). "Soil Stabilization with Lime-Fly Ash Mixtures: Preliminary Studies with Silty and Clayey Soils." *Highway Research Board Bulletin,* 108, 102—112.

Crovetti, J. A., Shahin, M. Y., and Touma, B. E. (1989). "Comparison of Two Falling Weight Deflectometer Devices, Dynatest 8000 and KUAB 2M-FWD." *First International Symposium on Nondestructive Testing of Pavements and Backcalculation of Moduli*, A. J. Bush, and G. Y. Baladi, eds., ASTM, Baltimore, Maryland, 59—69.

Das, B. M., and Das, B. (2011). *Fundamentals of Soil Dynamics*, Elsevier New York.

De Vries, S. W. (2012). "Financial Needs of Iowa's County Roads." Iowa Department of Transportation, Ames, Iowa, 83.

Delrio-Prat, M., Vega-Zamanillo, A., Castro-Fresno, D., and Calzada-Perez, M. A. (2011). "Energy Consumption during Compaction with A Gyratory Intensive Compactor Tester. Estimation Models." *Construction and Building Materials*, 25(2), 979—986.

Douglas, R. A., and Valsangkar, A. J. (1992). "Unpaved Geosynthetic-Built Resource Access Roads: Stiffness Rather than Rut Depth as the Key Design Criterion." *Geotextiles and Geomembranes*, 11(1), 45—59.

Dunnett, C. W. (1980). "Pairwise Multiple Comparisons in the Unequal Variance Case." *Journal of the American Statistical Association*, 75(372), 796—800.

Fannin, R. J., and Sigurdsson, O. (1996). "Field Observations on Stabilization of Unpaved Roads with Geosynthetics." *Journal of Geotechnical Engineering*, 122(7), 544—553.

Fay, L., Kroon, A., Skorseth, K., Reid, R., and Jones, D. (2016). "Converting Paved Roads to Unpaved." *NCHRP Synthesis 485*Washington, D.C., 98.

FHWA (2014). "Highway Statistics 2014." Federal Highway Administration, Washington, DC, https://www.fhwa.dot.gov/policyinformation/statistics/2014/, Accessed [07/09/2016].

Fletcher, T., Chandan, C., Masad, E., and Sivakumar, K. (2003). "Aggregate Imaging System for Characterizing the Shape of Fine and Coarse Aggregates." *Transportation Research Record: Journal of the Transportation Research Board*, 1832, 67—77.

Freeman, E. A. (2006). "Geotextile Separators for Dust Suppression on Gravel Roads." Master of Science, University of Missouri--Columbia, Columbia, MO.

Ghafoori, N., Nyknahad, D., and Wang, L. (2013). "Use of Pulverised and Fluidised Combustion Coal Ash in Secondary Road Construction." *International Journal of Pavement Engineering*, 14(2), 176—189.

Giroud, J. P. (2009). "An Assessment of the Use of Geogrids in Unpaved Roads and Unpaved Areas." *Jubilee Symposium on Polymer Geogrid Reinforcement. Identifying the Direction of Future Research,* London.

Giroud, J. P., and Han, J. (2004a). "Design Method for Geogrid-Reinforced Unpaved Roads. I. Development of Design Method." *Journal of Geotechnical and Geoenvironmental Engineering*, 130(8), 775—786.

Giroud, J. P., and Han, J. (2004b). "Design Method for Geogrid-Reinforced Unpaved Roads. II. Calibration and Applications." *Journal of Geotechnical and Geoenvironmental Engineering*, 130(8), 787—797.

Guler, M., Bahia, H. U., Bosscher, P. J., and Plesha, M. E. (2000). "Device for Measuring Shear Resistance of Hot-Mix Asphalt in Gyratory Compactor." *Transportation Research Record:Journal of the Transportation Research Board,* 1723, 116—124.

Gökalp, İ., Uz, V. E., and Saltan, M. (2016). "Testing the Abrasion Resistance of Aggregates Including By-Products by Using Micro Deval Apparatus with Different Standard Test Methods." *Construction and Building Materials*, 123, 1—7.

Hammitt, G. M., and Aspinall, W. (1970). "Thickness Requirements for Unsurfaced Roads and Airfields; Bare Base Support." *Technical report S-70-5*, U.S. Army Engineer Waterways Experiment Station, Vicksburg, Miss, 139.

Hardin, B. (1985). "Crushing of Soil Particles." *Journal of Geotechnical Engineering*, 111(10), 1177—1192.

Hardin, B. O., and Drnevich, V. P. (1972). "Shear Modulus and Damping in Soils: Design Equations and Curves." *Journal of the Soil Mechanics and Foundations Division*, 98(7), 667—692.

Harman, T., Bukowski, J. R., Moutier, F., Huber, G., and McGennis, R. (2002). "History and Future Challenges of Gyratory Compaction 1939 to 2001." *Transportation Research Record: Journal of the Transportation Research Board,* 1789, 200—207.

Henry, K. S. (1990). "Laboratory Investigation of the Use of Geotextiles to Mitigate Frost Heave." U.S. Army Cold Regions Research and Engineering Laboratory, Washington, D.C., 36.

Henry, K. S. (1996). "Geotextiles to Mitigate Frost Effects in Soils: a Critical Review." *Transportation Research Record,* 1534, 8—11.

Henry, K. S., and Holtz, R. D. (2001). "Geocomposite Capillary Barriers to Reduce Frost Heave in Soils." *Canadian Geotechnical Journal*, 38(4), 678—694.

Henry, K. S., Olson, J. P., Farrington, S. P., and Lens, J. (2005). "Improved Performance of Unpaved Roads During Spring Thaw." Engineer Research and Development Center Cold Regions Research and Engineering Laboratory, Hanover, New Hampshire, 179.

Hochberg, Y., and Tamhane, A. C. (1987). "Single-Step Procedures for Pairwise and More General Comparisons among All Treatments." *Multiple Comparison Procedures*, John Wiley & Sons, Inc., 72—109.

Hoffman, M. S., and Thompson, M. R. (1982). "Comparative Study of Selected Nondestructive Testing Devices." *Transportation Research Record: Journal of the Transportation Research Board,* 852, 32—41.

Holtz, R. D., Christopher, B. R., and Berg, R. R. (2008). "Geosynthetic Design and Construction Guidelines." FHWA-NHI-07-092, National Highway Institute, Federal Highway Administration, U.S. Department of Transportation, Washington, D.C.

Hoover, J. M., Pitt, J. M., Handfelt, L. D., and Stanley, R. L. (1981). "Performance of Soil-Aggregate-Fabric Systems in Frost-Susceptible Roads, Linn County, Iowa." *Journal of the Transportation Research Board*, 827, 6—14.

Huang, Y. H. (2004). *Pavement analysis and design*, Pearson Education, Inc., Upper Saddle River, New Jersey.

Hudson, S. W., McCullough, B. F., and Carmichael, R. F. (1986). "Aggregate and Paved Surface Design and Rehabilitation Manual for Low-Volume Roads."Washington, DC, 247.

Hufenus, R., Rueegger, R., Banjac, R., Mayor, P., Springman, S. M., and Bronnimann, R. (2006). "Full-Scale Field Tests on Geosynthetic Reinforced Unpaved Roads on Soft Subgrade." *Geotextiles and Geomembranes*, 24, 21—37.

Igathinathane, C., Pordesimo, L. O., Columbus, E. P., Batchelor, W. D., and Methuku, S. R. (2008). "Shape Identification and Particles Size Distribution from Basic Shape Parameters using ImageJ." *Computers and Electronics in Agriculture*, 63(2), 168—182.

Indraratna, B., Lackenby, J., and Christie, D. (2005). "Effect of Confining Pressure on the Degradation of Ballast under Cyclic Loading." *Géotechnique*, 55(4), 325-328.

Indraratna, B., Sun, Y., and Nimbalkar, S. (2016). "Laboratory Assessment of the Role of Particle Size Distribution on the Deformation and Degradation of Ballast under Cyclic Loading." *Journal of Geotechnical and Geoenvironmental Engineering*, 142(7).

Iowa DOT. (2011). "Iowa County Traffic Map." Iowa Department of Transportation, Ames, Iowa.

Jahren, C. T., Smith, D., Thorius, J., Rukashaza-Mukome, M., White, D., and Johnson, G. (2005). "Economics of upgrading an aggregate road." Minnesota Department of Transportation, St. Paul, Minnesota, 72.

Jiménez, J. R., Ayuso, J., Agrela, F., López, M., and Galvín, A. P. (2012). "Utilisation of Unbound Recycled Aggregates from Selected CDW in Unpaved Rural Roads." *Resources, Conservation and Recycling*, 58, 88—97.

Jobgen, M. C., Tymkowicz, S., Harris, G., and Callahan, M. (1994). "Low Cost Techniques of Base Stabilization." Project HR-312, Iowa Department of Transportation, Ames, Iowa., 40.

Johnson, A. (2012). "Freeze-Thaw Performance of Pavement Foundation Materials."M.S. Thesis, Dept. of Civil Construction and Environmental Engineering, Iowa State University, Ames, Iowa.

Jones, D., Kociolek, A., Surdahl, R., Bolander, P., Drewes, B., Duran, M., Fay, L., Huntington, G., James, D., Milne, C., Nahra, M., Scott, A., Vitale, B., and Williams, B. (2013). "Unpaved Road Dust Management, A Successful Practitioner's Handbook." *FHWA-CFL/TD-13-001*Lakewood, CO, 94.

Jones, D., and Paige-Green, P. (2015). "Limitations of Using Conventional Unpaved Road Specifications for Understanding Unpaved Road Performance." *Transportation Research Record: Journal of the Transportation Research Board*, 2474, 30—38.

Kazmee, H., Tutumluer, E., and Beshears, S. (2016). "Pavement Working Platforms Constructed with Large-Size Unconventional Aggregates." *Transportation Research Record: Journal of the Transportation Research Board*, 2578, 1—11.

Kestler, M. A. (2003). "Techniques for Extending the Life of Low-Volume Roads in Seasonal Frost Areas." *Eight International Conference on Low-Volume Roads*, National Research Council, Reno, NV, United states, 275—284.

Khoury, N. N., and Zaman, M. M. (2007). "Durability of Stabilized Base Courses Subjected to Wet–Dry Cycles." *International Journal of Pavement Engineering*, 8(4), 265—276.

Knapton, J. (1989). *The Structural Design of Heavy Duty Pavements for Ports and Other Industries*, British Ports Association, London, United Kingdom.

Krumbein, W. C. (1941). "Measurement and Geological Significance of Shape and Roundness of Sedimentary Particles." *Journal of Sedimentary Research*, 11(2), 64—72.

Kumara, G. H. A., Hayano, K., and Ogiwara, K. (2012). "Image Analysis Techniques on Evaluation of Particle Size Distribution of Gravel." *Intern. J. of Geomate*, 3(1), 290—297.

Lackenby, J., Indraratna, B., McDowell, G., and Christie, D. (2007). "Effect of Confining Pressure on Ballast Degradation and Deformation under Cyclic Triaxial Loading." *Géotechnique*, 57(6), 527—536.

Lade, P., Yamamuro, J., and Bopp, P. (1996). "Significance of Particle Crushing in Granular Materials." *Journal of Geotechnical Engineering*, 122(4), 309—316.

Lai, Y., Zhang, S., and Yu, W. (2012). "A New Structure to Control Frost Boiling and Frost Heave of Embankments in Cold Regions." *Cold Regions Science and Technology*, 79—80, 53-66.

Latha, G. M., Nair, A. M., and Hemalatha, M. S. (2010). "Performance of Geosynthetics in Unpaved Roads." *International Journal of Geotechncical Engineering*, 2010(4), 337—349.

Lees, G., and Kennedy, C. K. (1975). "Quality, Shape and Degradation of Aggregates." *Quarterly Journal of Engineering Geology*, 8(3), 193—209.

Less, R. A., and Paulson, C. K. (1977). "Experimental Macadam Stone Base-Des Moines County." Project HR-175, Iowa Department of Transportation, Ames, Iowa.

Li, C., Ashlock, J. C., White, D. J., and Vennapusa, P. (2015). "Low-Cost Rural Surface Alternatives: Demonstration Project." IHRB Project TR-664, InTrans Project 13-479, Ames, Iowa, 242.

Li, C., White, D., and Vennapusa, P. (2015). "Moisture-Density-Strength-Energy Relationships for Gyratory Compacted Geomaterials." *Geotechnical Testing Journal*, 38(4), 461—473.

Li, L., Benson, C.H., Edil, T.B. and Hatipoglu, B. (2008). "Sustainable Construction Case History: Fly Ash Stabilization of Recycled Asphalt Pavement Material." *Geotechnical and Geological Engineering*, 26(2): 177-187.

Lin, S. (2014). "Advancements in active surface wave methods: modeling, testing, and inversion." Doctor of Philosophy, Iowa State University, Ames, Iowa.

Lin, S., and Ashlock, J. C. (2011). "A Study on Issues Relating to Testing of Soils and Pavements by Surface Wave Methods." *38th Annual Review of Progress in Quantitative Nondestructive Evaluation*Burlington, VT, 1532-1539.

Lin, S., and Ashlock, J. C. (2015). "Comparison of MASW and MSOR for Surface Wave Testing of Pavements." *Journal of Environmental and Engineering Geophysics*, 20(4), 277—285.

Liu, Y., Sun, W., Nair, H., Lane, D. S., and Wang, L. (2016). "Quantification of Aggregate Morphologic Characteristics with the Correlation to Uncompacted Void Content of Coarse Aggregates in Virginia." *Construction and Building Materials*, 124, 645—655.

Lynam, D., and Jones, K. (1979). "Pavement Surfaced on Macadam Base-Adair County." Project HR-209, Iowa Department of Transportation, Ames, Iowa.

Lytton, R. L. (1989). "Backcalculation of Pavement Layers Properties." *First International Symposium on Nondestructive Testing of Pavements and Backcalculation of Moduli*, A. J. Bush, and G. Y. Baladi, eds., ASTM, Baltimore, Maryland, 7—38.

Légère, G., and Mercier, S. (2003). "Improving Road Performance by Using Appropriate Aggregate Specifications for Wearing Course." *Proc., Forest Engineering Research Institute of Canada (FERIC)*, 6.

Marsal, R. J. (1967). "Large-Scale Testing of Rockfill Materials." *Journal of the Soil Mechanics and Foundations Division*, 93(2), 27—43.

Mokwa, R., and Cuelho, E. (2008). "Laboratory Testing of Soil Using the Superpave Gyratory Compactor." *Proc., Transportation Research Board 87th Annual Meeting*, Transportation Research Board, 14.

Nokkaew, K., Tinjum, J., and Benson, C. (2012). "Hydraulic Properties of Recycled Asphalt Pavement and Recycled Concrete Aggregate." *GeoCongress 2012*, American Society of Civil Engineers, 1476—1485.

NRCS (2016). "Natural Resources Conservation Service Web Soil Survey." United States Department of Agriculture, Available online at http://websoilsurvey.nrcs.usda.gov/, Accessed [03/09/2016].

Nurmikolu, A. (2005). "Degradation and Frost Susceptibility of Crushed Rock Aggregates Used in Structural Layers of Railway Track." Doctor of Technology, Tampere University of Technology, Tampere, Finland.

Odemark, N. (1949). "Investigations as to the Elastic Properties of Soils and Design of Pavements According to the Theory of Elasticity."Statens Vaginstitut, Stockholm, Sweden.

Ohm, H., and Hryciw, R. (2013). "Translucent Segregation Table Test for Sand and Gravel Particle Size Distribution." *Geotechnical Testing Journal*, 36(4).

Ott, R. L., and Longnecker, M. (2001). *An Introduction to Statistical Methods and Data Analysis*, Cengage Learning, Belmont, CA.

Özen, M. (2007). "Investigation of Relationship Between Aggregate Shape Parameters and Concrete Strength Using Imaging Techniques." Master of Science, Middle East Technical University, Ankara, Turkey.

Paige-Green, P. (1989). "The influence of geotechnical properties on the performance of gravel wearing course materials." Ph.D. University of Pretoria (South Africa), South Africa.

Paige-Green, P. (1998). *Material Selection and Quality Assurance for Labour-Based Unsealed Road Projects*, International Labour Organisation, Advisory Support, Information Services, and Training.

Pan, T., Tutumluer, E., and Anochie-Boateng, J. (2006). "Aggregate Morphology Affecting Resilient Behavior of Unbound Granular Materials." *Transportation Research Record: Journal of the Transportation Research Board*, 1952, 12—20.

Park, C. B., Ivanov, J., Miller, R. D., Xia, J., and Ryden, N. (2001). "Multichannel Analysis of Surface Waves (MASW) for Pavement: Feasibility Test." *Proc., The 5th SEGJ International Symposium*, The Society of Exploration Geophysicists of Japan, 25—30.

Park, C. B., Miller, R. D., and Xia, J. (1998). "Imaging Dispersion Curves of Surface Waves on Multi-Channel Record." *Technical Program with biographies, SEG, 68th Annual Meeting*New Orleans, Louisiana, 1377—1380.

Park, C. B., Miller, R. D., and Xia, J. (1999). "Multichannel Analysis of Surface Waves." *Geophysics*, 64(3), 800—808.

Parsons, R. L., and Milburn, J. P. (2003). "Engineering Behavior of Stabilized Soils." *Transportation Research Record: Journal of the Transportation Research Board*, 1837, 20—29.

PCA (1995). "Soil-Cement Construction Handbook." Portland Cement Association, Skokie, Illinois.

Ping, V. W., Yang, Z., Leonard, M., and Putcha, S. (2002). "Laboratory Simulation of Field Compaction Characteristics on Sandy Soils." *Transportation Research Record: Journal of the Transportation Research Board,* 1808, 84—95.

Ping, W. V., Xing, G., Leonard, M., and Yang, Z. (2003). "Evaluation of Laboratory Compaction Techniques for Simulating Field Soil Compaction (Phase II)." Florida Department of Transportation, Tallahassee, FL, 199.

Puppala, A. J. (2008). "Estimating Stiffness of Subgrade and Unbound Materials for Pavement Design." *NCHRP Synthesis 382*Washington, D.C., 137.

Rahardjo, H., Vilayvong, K., and Leong, E. (2011). "Water Characteristic Curves of Recycled Materials." *Geotechnical Testing Journal*, 34(1), 1—8.

Rao, C., Tutumluer, E., and Stefanski, J. (2001). "Coarse Aggregate Shape and Size Properties Using a New Image Analyzer." *Journal of Testing and Evaluation*, 29(5), 461—471.

Rittenhouse, G. (1943). "A Visual Method of Estimating Two-Dimensional Sphericity." *Journal of Sedimentary Research*, 13(2).

Rollins, K. M., Evans, M. D., Diehl, N. B., and Daily, W. D., III (1998). "Shear modulus and damping relationships for gravels." *Journal of Geotechnical and Geoenvironmental Engineering*, 124(5), 396—405.

Ryden, N. (2004). "Surface Wave Testing of Pavements." Doctoral of Philosophy, Lund Institute of Technology, Lund University, Lund, Sweden.

Ryden, N., and Mooney, M. A. (2009). "Analysis of Surface Waves From the Light Weight Deflectometer." *Soil Dynamics and Earthquake Engineering*, 29(7), 1134—1142.

Saarenketo, T., and Aho, S. (2005). "Managing Spring Thaw Weakening on Low Volume Roads: Problem Description, Load Restriction, Policies, Monitoring and Rehabilitation." ROADEX II, Northern Periphery, Inverness, Scotland.

Satterthwaite, F.E. (1946). "An Approximate Distribution of Estimates of Variance Components." Biometrics Bulletin, 2(6): 110-114.

Schneider, C. A., Rasband, W. S., and Eliceiri, K. W. (2012). "NIH Image to ImageJ: 25 Years of Image Analysis." *Nature Methods*, 9(7), 671—675.

Scott III, S., Konrath, L., Ferragut, T., Anderson, S., Damnjanovic, I., Huber, G., Katsafanas, J., McGhee, K., Sprinkel, M., Ozyildirim, C., Diefenderfer, B., Merritt, D., Dawood, D., Molenaar, K., Loulakis, M. C., White, D., and Schaeffer, V. R. (2014). "Performance Specifications for Rapid Highway Renewal." *S2-R07-RR-1*, Transportation Research Board, 245.

Seed, H., Wong, R., Idriss, I., and Tokimatsu, K. (1986). "Moduli and Damping Factors for Dynamic Analyses of Cohesionless Soils." *Journal of Geotechnical Engineering*, 112(11), 1016—1032.

Shoop, S., Kestler, M., Stark, J., Ryerson, C., and Affleck, R. (2003). "Rapid Stabilization of Thawing Soils: Field Experience and Application." *Journal of Terramechanics*, 39(4), 181—194.

Skorseth, K., and Selim, A. A. (2000). "Gravel roads: maintenance and design manual." U.S. Department of Transportation, 106.

Solanki, P., Zaman, M., and Khalife, R. (2013). "Effect of Freeze-Thaw Cycles on Performance of Stabilized Subgrade." *Sound Geotechnical Research to Practice: Honoring Robert D. Holtz II, Geotechnical Special Publication (GSP) No. 230*, R. D. Holtz, A. W. Stuedlein, and B. R. Christoper, eds., ASCE, Reston, VA, 567—581.

Stoline, M. R., and Ury, H. K. (1979). "Tables of the Studentized Maximum Modulus Distribution and an Application to Multiple Comparisons Among Means." *Technometrics*, 21(1), 87—93.

Stormont, J. C., Ramos, R., and Henry, K. S. (2001). "Geocomposite Capillary Barrier Drain Systems with Fiberglass Transport Layer." *Transportation Research Record: Journal of the Transportation Research Board*, 1772, 131—136.

Tannant, D., and Regensburg, B. (2001). "Guidelines for Mine Haul Road Design." University of British Columbia-Okanagan, Kelowna, B.C., Canada.

Terrel, R. L., Epps, J. A., Barenberg, E. J., Mitchell, J. K., and Thompson, M. R. (1979). "Soil Stabilization in Pavement Structures - A User's Manual." COT-FH-11-9406, Federal Highway Administration, Department of Transportation, Washington D.C.

Tingle, J. S., and Webster, S. L. (2003). "Corps of Engineers Design of Geosynthetic-Reinforced Unpaved Roads." *Transportation Research Record: Journal of the Transportation Research Board*, 1849, 193—201.

Tutumluer, E., Rao, C., and Stefanski, J. A. (2000). "Video Image Analysis of Aggregates." *Transportation Engineering Series No. 111, Illinois Cooperative Highway and Transportation Series No. 278,* Springfield, IL.

USACE (1984). "*Engineering and Design Pavement Design for Seasonal Frost Conditions Mobilization Construction.*" U.S. Army Corps of Engineers, Washington D.C.

Vallejo, L., Lobo-Guerrero, S., and Hammer, K. (2006). "Degradation of a Granular Base under a Flexible Pavement: DEM Simulation." *International Journal of Geomechanics*, 6(6), 435—439.

Van Der Veen, M., Spitzer, R., Green, A. G., and Wild, P. (2001). "Design and Application of Towed Land-Streamer System for Cost-Effective 2-D and Pseudo-3-D Shallow Seismic Data Acquisition." *Geophysics*, 66(2), 482—500.

Van Zyl, G., Henderson, M., and Uys, R. (2007). "Applicability of existing gravel-road deterioration models questioned." *Transportation Research Record: Journal of the Transportation Research Board*, 1(1989), 217—225.

Vennapusa, P. K. R., and White, D. J. (2009). "Comparison of Light Weight Deflectometer Measurements for Pavement Foundation Materials." *Geotechnical Testing Journal*, 32(3), 239—251.

Vennapusa, P. K. R., and White, D. J. (2015). "Performance Assessment of Secondary-Roadway Infrastructure in Iowa After 2011 Missouri River Flooding." *Journal of Infrastructure Systems*, 21(4).

Wadell, H. (1932). "Volume, Shape, and Roundness of Rock Particles." *The Journal of Geology*, 40(5), 443—451.

White, D., and Vennapusa, P. (2013). "Low-Cost Rural Surface Alternatives: Literature Review and Recommendations." Iowa Department of Transportation, Ames, Iowa.

White, D., and Vennapusa, P. (2014). "Rapid In Situ Measurement of Hydraulic Conductivity for Granular Pavement Foundations." *Geo-Congress 2014*, American Society of Civil Engineers, Atlanta, Georgia, 3005—3014.

White, D. J., Becker, P., Vennapusa, P. K., Dunn, M. J., and White, C. I. (2013). "Assessing Soil Stiffness of Stabilized Pavement Foundations." *Transportation Research Record: Journal of the Transportation Research Board*, 2335, 99—109.

White, D. J., Ceylan, H., Jahren, C. T., Phan, T. H., Kim, S. H., Gopalakrishnan, K., and Suleiman, M. T. (2008). "Performance evaluation of concrete pavement granular subbase–pavement surface condition evaluation.", IHRB Project TR-554, Ames, Iowa.

White, D. J., Harrington, D., Ceylan, H., and Rupnow, T. (2005a). "Fly Ash Soil Stabilization for Non-Uniform Subgrade Soils, Volume II: Influence of Subgrade Non-Uniformity on PCC Pavement Performance." IHRB Project TR-461; FHWA Project 4, Ames, Iowa.

White, D. J., Harrington, D., and Thomas, Z. (2005b). "Fly Ash Soil Stabilization for Non-Uniform Subgrade Soils, Volume I: Engineering Properties and Construction Guidelines." IHRB Project TR-461, FHWA Project 4, Ames, Iowa.

White, D. J., Vennapusa, P., and Jahren, C. T. (2004). "Determination of the Optimum Base Characteristics for Pavements." Iowa Department of Transportation, Ames, Iowa, 270.

Wightman, W. E., Jalinoos, F., Sirles, P., and Hanna, K. (2004). "Application of Geophysical Methods to Highway Related Problems." FHWA-IF-04-021, Washington D.C., 742.

Winterkorn, H., and Pamukcu, S. (1991). "Soil Stabilization and Grouting." *Foundation Engineering Handbook*, H.-Y. Fang, ed., Springer US, 317—378.

Xia, J., Miller, R., and Park, C. (1999). "Estimation of Near-Surface Shear-Wave Velocity by Inversion of Rayleigh Waves." *Geophysics*, 64(3), 691—700.

Yue, Z. Q., Bekking, W., and Morin, I. (1995). "Application of Digital Image Processing To Quantitative Study of Asphalt Concrete Microstructure." *Transportation Research Record: Journal of the Transportation Research Board,* 1492, 53—60.

Zeghal, M. (2009). "The Impact of Grain Crushing on Road Performance." *Geotechnical and Geological Engineering*, 27(4), 549—558.

Zhang, Y., Johnson, A. E., and White, D. J. (2016). "Laboratory Freeze–Thaw Assessment of Cement, Fly Ash, and Fiber Stabilized Pavement Foundation Materials." *Cold Regions Science and Technology*, 122, 50—57.